Characterising the Electromagnetic Environment of MeerKAT

by

Temwani Joshua Phiri

Dissertation presented for the degree of Doctor of Philosophy in Electronic Engineering in the Faculty of Engineering at Stellenbosch University

Supervisor: Prof David B. Davidson

Co-supervisor: Dr P. Gideon Wiid

March 2017

Declaration

By submitting this dissertation electronically, I declare that the entirety of the work contained therein is my own, original work, that I am the sole author thereof (save to the extent explicitly otherwise stated), that reproduction and publication thereof by Stellenbosch University will not infringe any third party rights and that I have not previously in its entirety or in part submitted it for obtaining any qualification.

Date: 20-02-2017 .....

Abstract

Characterising the Electromagnetic Environment of MeerKAT

T.J. Phiri

Department of Electrical and Electronic Engineering,
Stellenbosch University,
Private Bag X1, 7602 Matieland, South Africa.

Dissertation: PhD (Elec)

March 2017

MeerKAT is South Africa's 64-dish precursor radio telescope to the Square Kilometre Array (SKA), currently under construction in the semi-desert Karoo region. As these are new generation instruments, their specifications far exceed those of existing telescopes and thereby increases their susceptibility to radio frequency interference (RFI). So far, much has been accomplished in terms of electromagnetic compatibility (EMC) interventions. However, surveys in the recent past have indicated the need to examine signal propagation in the Karoo in greater detail. In particular, reliable predictive tools are essential in order to fully characterize the environment which is changing gradually as infrastructure development progresses.

As a matter of first importance, selected empirical propagation models were statistically assessed by comparison to measurements in the Karoo. Based on the root mean square error (RMSE) values, the transmission loss predictions were deemed reliable. In spite of this, the limitations of empirical modelling were apparent: failure to accurately model real ground, inability to incorporate scattering phenomena and inadequacy in representing underlying physical processes.

To meet the accuracy demands of the South African SKA Project (SKA-SA) pertaining to characterising the complex environment of MeerKAT, a deterministic model exploiting full-wave and asymptotic techniques was developed. Referred to simply as a ray model, this solution utilised the method of moments (MoM) to determine antenna characteristics and solve for real ground, while physical optics was utilised to address scattering from the dishes. With the software FEKO as the interface and simulation engine, the MeerKAT core was reproduced computationally. Analysis of the numeric data revealed the full extent of electromagnetic complexity in relation to multipath. Most notably, high spatial resolution attenuation maps were generated, revealing high and low risk regions. This has benefits for identification of potential RFI problems.

The ray model showed very good performance when examined against measurements (RMSE < 4 dB). This is highly advantageous since numerical modelling allows a lot more flexibility than physical testing permits. In particular, the novelty and significance of this research is the ability to reproduce an actual deployment scenario with precision and high accuracy.

Uittreksel

Karakterisering van die Elektromagnetiese Omgewing van MeerKAT

("Characterising the Electromagnetic Environment of MeerKAT")

T.J. Phiri

Departement Elektriese en Elektroniese Ingenieurswese,
Universiteit van Stellenbosch,
Privaatsak X1, 7602 Matieland, Suid Afrika.

Proefskrif: PhD (Elek)

Maart 2017

Meerkat is Suid-Afrika se 64-skottel voorloper tot die Square Kilometre Array (SKA) radioteleskoop, wat tans in die semi-woestyn Karoo gebied gebou word. Omdat hierdie nuwe generasie instrumente is, oorskry hul spesifikasies dié van bestaande teleskope by verre, dus is hul vatbaarheid vir beide radiofrekwensie steurings (RFS) verhoog. Tot dusver is daar baie vermag in terme van elektromagnetiese versoenbaarheid (EMV) stappe. Onlangse opnames het egter gelei tot die behoefte aan verdere ondersoek van seinvoortplanting in die Karoo. In besonder is daar 'n behoefte aan betroubare voorspellingsgereedskap om ten volle die omgewing, wat geleidelik verander soos die ontwikkeling van infrastruktuur vorder, te karakteriseer.

As 'n saak van eerste belang, is verkose empiriese voortplantingsmodelle statisties geëvalueer deur dit met metings in die Karoo te vergelyk. Op grond van die wortel-gemiddeld-kwadraatfout (WGKF) waardes, was die oordragverliesvoorspellings betroubaar. Ten spyte hiervan, was die beperkings van empiriese modellering duidelik: ware grond word nie akkuraat gemodelleer nie, verstrooiinsverskynsels word nie inkorporeer nie en onderliggende fisiese prosesse word nie voldoende voorgestel nie..

Om aan die akkuraatheid te voldoen wat van die Suid-Afrikaanse SKA Projek (SKA-SA) vereis word met betrekking tot die karakterisering van die komplekse omgewing van MeerKAT, is 'n deterministiese model ontwikkel wat van volgolf en asimptotiese tegnieke gebruik maak.

Hierdie oplossing, wat eenvoudig na verwys word as die straalmodel, het die metode van momente (MoM) gebruik om antenna eienskappe te bepaal en vir ware grond op te los, terwyl fisiese optika gebruik is om verstrooiing van die skottels aan te spreek. Met die sagteware FEKO as die koppelvlak en simulasie enjin, is die MeerKAT kern met dié berekeningsmetode gereproduseer. Ontleding van die numeriese data het die volle omvang van elektromagnetiese kompleksiteit met betrekking tot multipadopstellings aan die lig gebring. Mees merkbaar was die ontwikkeling van hoë ruimtelike resolusie verswakkingskaarte wat beide hoë en lae risiko streke uitgewys het. Hierdie het voordele vir die identifisering van potensiële RFI probleme.

Die straalmodel het egter uitgeblink wanneer dit teen metings ondersoek was (WGKF < 4 dB). Dit is hoogs voordelig aangesien numeriese modellering baie meer buigsaam as fisiese toetse

is. In besonder is die nuutheid en noemenswaardigheid van hierdie navorsing die vermoë om ’n werklike ontplooiing scenario met presisie en hoë akkuraatheid te reproduseer.

Acknowledgements

I am grateful to my supervisor, Prof David B. Davidson, for being an excellent mentor and an inspiration. His guidance has been impeccable. I have also benefited much from Dr P. Gideon Wiid who has been my co-supervisor. I am especially thankful for the way he guided my thought process on and seeing to it that we conducted the necessary measurements. I also wish to thank Prof Howard C. Reader for recruiting me and subsequently playing a pivotal advisory role in my research.

I extend thanks to Danie Ludick for helping with FEKO simulations and running jobs on the Rhasatsha HPC; Nogy Mutonkole for sharing Matlab scripts, moral support and helpful discussions; Joely Andriambeloson and Stanley Kuja for assisting with measurements, making suggestions and aiding my thinking process; Anneke Bester and Wessel Crouwkamp for technical support and their creative solutions; Stephan Combrink, Hardie Pienaar, Mariet Venter, Anathi Hokwana, Mourits de Beers and Sam Dodson for the value they added as friends and colleagues. My sincere gratitude to John-Paul Harper for assisting with the translation of my abstract into Afrikaans at short notice.

I am indebted to the South African SKA office for funding this research and the opportunity to conduct measurements at the SKA site. Thanks to Carel van der Merwe for being supportive of this research, Adrian Tiplady for broadening my thinking around propagation issues and Tshegofatso Monama for assisting with GIS issues.

I am grateful to EMC Consultants MESA Solutions for sharing data and assisting with measurements at the MeerKAT. Special thanks to the FEKO Support Team (South Africa) – especially Mel van Rooyen and Danie le Roux – for providing meaningful feedback that tremendously contributed to the final modelling.

The Canon Collins Trust supported me with supplementary funding for which I am thankful. Interactions with the Trust have broadened my thinking around social justice and the meaning of development.

I also wish to acknowledge the administrative assistance received from the Department of Electrical and Electronic Engineering. In particular, I salute Johan Booysen and Larry Morkel for the excellent work they do.

My deepest and heartfelt gratitude to my wife Chimwemwe for her constant support. I cannot fully express how thankful I am for her love, care and reassurance. I will always be indebted to my parents for their love, support and vote of confidence. A big thank you to my brothers, Wezi and Kachinga, for their contribution to who I am and making it possible for me to pursue my academic ambitions. Thanks to my parents-in-love (Mathias and Esther Tembo) for their encouragement.

The financial assistance of the South African SKA Project (SKA-SA) towards this research is hereby acknowledged. Opinions expressed and conclusions arrived at are those of the author and are not necessarily to be attributed to the SKA-SA. www.ska.ac.za

Full scale computations of the KAT-7 array and the MeerKAT core were performed using the Stellenbosch University HPC1 (Rhasatsha): http://www.sun.ac.za/hpc

In honour of the late Fred Kunda Phiri, my father and the greatest mentor I have ever known: a tribute to his legacy of hard work, the love for literature and critical thinking

In memory of my maternal grandmother, Tamali Nakamba, who loved education

To Chimwemwe, the wife my youth and queen of my heart: thank you for taking a plunge with this dreamer and caring for me the way you have

Contents

List of Figures

List of Tables

Nomenclature

Abbreviations

CAD	Computer Aided Design
CEM	Computational Electromagnetics
COST	European Cooperation in the field of Scientific and Technical Research
DE	Differential Equation
EHF	Extremely High Frequency
EIRP	Effective Isotropic Radiated Power
EM	Electromagnetic
EMC	Electromagnetic Compatibility
EMI	Electromagnetic Interference
ERP	Effective Radiated Power
FD	Frequency Domain
FDTD	Finite-Difference Time-Domain
FEM	Finite Element Method
FSL	Free Space Loss
FWPM	Full-wave Propagation Model
GLPDA	Gideon Wiid Log-Periodic Dipole Antenna
GO	Geometrical Optics
GTD	Geometrical Theory of Diffraction
GUI	Graphical User Interface
HF	High Frequency
HOBF	Higher Order Basis Functions
IE	Integral Equation
ITM	Irregular Terrain Model
ITU	International Telecommunication Union
ITU-R	International Telecommunication Union Radiocommunication Sector
KAPB	Karoo Array Processor Building
KAT	Karoo Array Telescope
KLPDA	Keith Palmer Log-Periodic Dipole Antenna
LE-PO	Large Element Physical Optics
LF	Low Frequency
LNA	Low Noise Amplifier
LOS	Line-of-Sight
LPDA	Log-Periodic Dipole Antenna
MF	Medium Frequency

MLFMM	Multilevel Fast Multipole Method
MoM	Method of Moments
NTIA	National Telecommunications and Information Administration
PCB	Printed Circuit Board
PDE	Partial Differential Equation
PE	Parabolic Equation
PEC	Perfect Electric Conductor
PO	Physical Optics
RCA	Reflection Coefficient Approximation
RE	Relative Error
RF	Radio Frequency
RFI	Radio Frequency Interference
RL-GO	Ray Launching Geometrical Optics
RMS	Root Mean Square
RMSE	Root Mean Square Error
RQZ	Radio Quiet Zone
RT	Ray-tracing
RTA	Real-time Analyser
RWG	Rao-Wilton-Glisson
SA	Spectrum Analyser
SD	Standard Deviation
SE	Standard Error
SHF	Super High Frequency
SKA	Square Kilometre Array
SKA-SA	Square Kilometre Array South Africa
TDS	Thin Dielectric Sheet
TEM	Transverse Electromagnetic
UHF	Ultra High Frequency
UTD	Uniform Theory of Diffraction
VHF	Very High Frequency

Chapter 1

Introduction

The South African Square Kilometre Array (SKA-SA) precursor instrument (MeerKAT) is being realised in the semi-desert Karoo region of the Northern Cape Province. Thus far, much has been achieved in terms of electromagnetic compatibility (EMC) interventions. However, surveys in the recent past indicated that signal propagation ought to be examined in greater detail, ultimately leading to an electromagnetic characterisation of the site. The focus of this research is therefore assessing and developing propagation modelling tools.

1.1 MeerKAT and Its Environment

A new, international radio observatory with specifications that far exceed those of existing telescopes is on the horizon in the form of the Square Kilometre Array (SKA). As the name indicates, a primary attribute of the fully completed SKA telescope will be its large collecting area of at least a square kilometre* realised by means of numerous, inter-linked antennas spread over two geographic locations: SKA1-mid in South Africa and SKA1-low in Australia [1]. Construction of the SKA in South Africa is preceded by the Karoo Array Telescope, MeerKAT (literally "more of KAT"), which will comprise 64, 13.5 m diameter dishes employing offset Gregorian configuration [2]. MeerKAT serves to demonstrate and develop cutting-edge technology in the mid-frequency band (350 to 3050 MHz) of the SKA and will be a world-class radio telescope in its own right once completed. At the time of writing (November 2016), assembly of MeerKAT dishes is progressing at a steady pace with 16 antennas – referred to as Array Release 1 (AR1) – already commissioned [3].

On the grounds of its radio quiet characteristics, the Karoo region was selected as the SKA and MeerKAT site. Situated a good distance away from radio frequency interference (RFI) sources, the site is additionally naturally shielded by the hilly terrain [4]. Furthermore, a vast portion of the Karoo is protected by legislation as a radio astronomy reserve and radio quiet zone (RQZ) to promote unencumbered longevity of radio astronomy activities [5, 6]. Presently, man-made noise is already limited by the fact that the area is sparsely populated. The exact location of the MeerKAT site lies 90 km in a west-northwest (WNW) direction from the town of Carnarvon in the Northern Cape Province. As can be seen in Figure 1.1, the landscape of the site is plain but surrounded by flat-topped hills, particularly to the south.

1.2 Problem Statement

Since inception of the seven dish KAT-7 array – an engineering testbed and MeerKAT forerunner – every effort has been made to preserve the electromagnetic (EM) quietness of the site

*The collecting area of SKA Phase 1 is less than 1 km^2

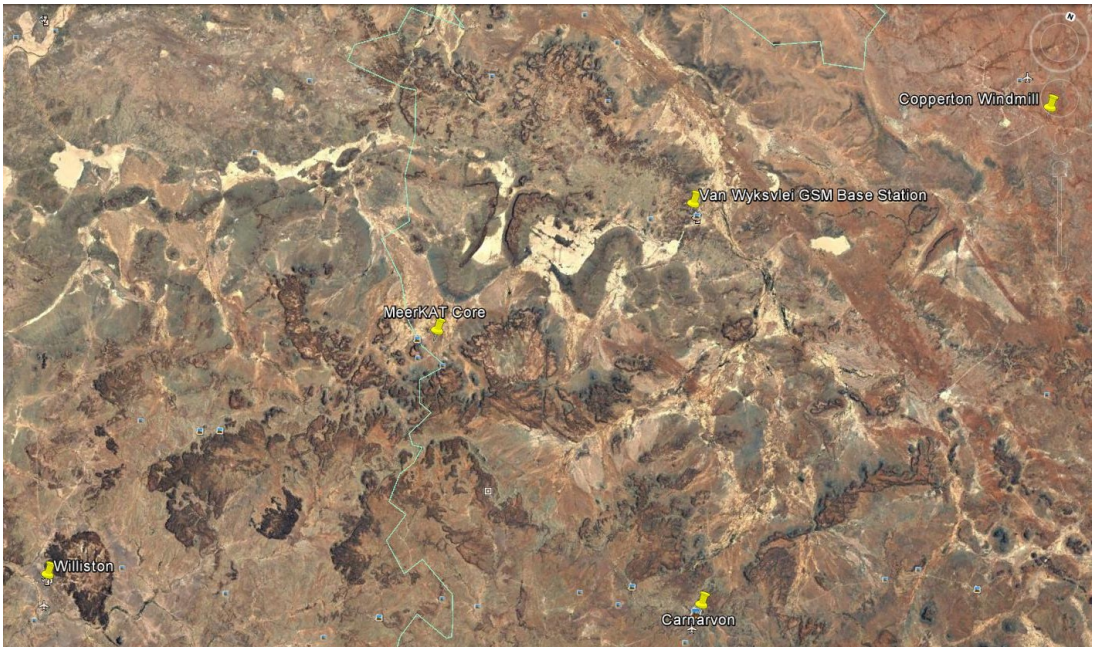

(a) MeerKAT site in relation to surrounding towns (Image credit: Google Earth)

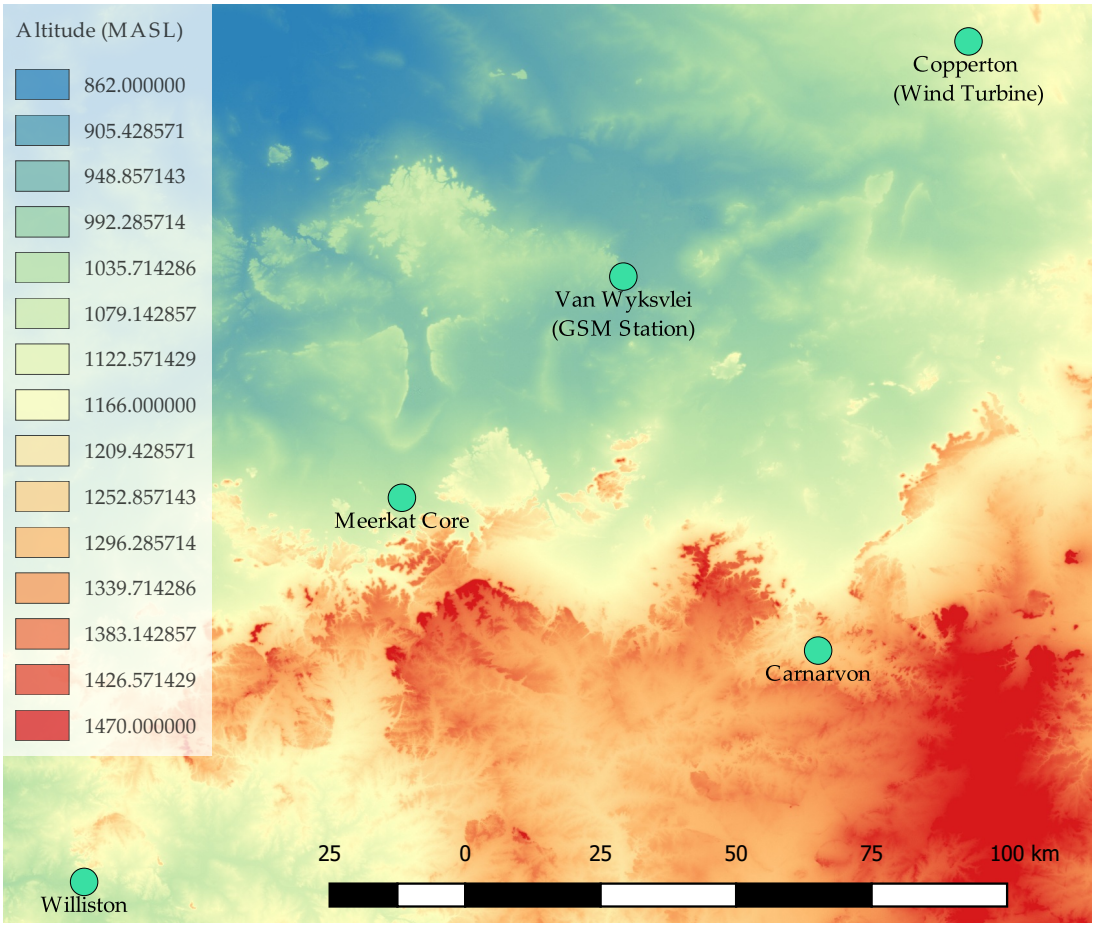

(b) Digital elevation model of the MeerKAT site and surrounding towns (Data source: Shuttle Radar Topography Mission (SRTM), USGS Explorer website)

Figure 1.1: Overview of the landscape at and around the MeerKAT site. The GSM base station closest to the site is at Van Wyksvlei (54.12 km from the core) while Copperton (129.18 km from the core) houses the nearest windmill.

through a meticulous RFI mitigation approach. Various electromagnetic compatibility (EMC) schemes have been implemented as a result of findings from powerline sparking investigations [7], cable layout and cable transfer impedance assessments [8], lightning protection studies [9] and pedestal shielding characterisation [10]. Continued research in EMC and spectrum management is essential to fully characterise the environment which is changing gradually as infrastructure development progresses. Within this framework, probing signal propagation lies at the heart of understanding the EM characteristics of the MeerKAT environment. Measurement campaigns in the recent past have thus focused on assessing: (1) the potential impact (on MeerKAT receivers) of noise emanating from within the Karoo Array Processor Building (KAPB) [11, 12]; and (2) signal attenuation over Karoo terrain [13, 14]. It has become overwhelmingly clear that accurate prediction tools are an indispensable requirement in drawing together a systematic picture of EM coupling and signal propagation. This is especially true in relation to the MeerKAT core which will have a dense arrangement of $\sim$40 dishes in a 1 km diameter. And herein lies the challenge: which models should be used? What level of accuracy can be obtained from empirical modelling?

There is a lot in literature addressing propagation predictions for terrestrial broadcasts (television and FM radio) and mobile cellular communications, but not much has been done in relation to propagation modelling for managing RFI in a radio astronomy environment. A significant difference between conventional modelling and radio observatory site protection is that for the latter, high loss is considered a good thing. Consequently, free space loss typically provides the reference benchmark for computing attenuation. On one hand, power protection thresholds may thus be more stringent than is necessary and on the other, a free space-derived protection level could be detrimental in a multipath environment.

1.3 Methodology

The object of propagation modelling is to account for signal degradation due to interactions with the radio environment. Path loss* is the main output parameter from a prediction and is defined as the difference in decibels (dB) between the power transmitted and the power received by an isotropic receiver. Theoretical and empirical predictions† can be made about an environments response to EM fields, particularly if terrain data are available. However, unless verification has been done for the specific or similar environment, such outputs must be regarded only as estimates.
This research thus relies on measured data to arrive at an understanding of the effects that are most critical to account for in the Karoo. Measurements also provide the basis for an evaluation of selected propagation models via statistical analysis. Prediction accuracy of a model is determined primarily by its root mean square error (RMSE), whereby values below 15 dB are considered accurate for a rural area [15].

*Basic transmission loss is the technically correct and preferred term in this work. See Appendix A for details.

†Theoretical predictions are based on a mathematical model derived from first principles of propagation theory while empirical predictions are based on a fit to previously observed phenomena

Computational modelling using the commercial electromagnetics code, FEKO, is utilised to address the challenge of scattering in the complex MeerKAT core. First, a full-wave propagation model (FWPM) employing the method of moments (MoM) is developed and shown to perform very well over relatively flat terrain at ranges between 20 and 3600 m. A hybrid of the MoM with physical optics (PO) yields a ray model that is subsequently applied to model multipath effects within a 1 km radius of the MeerKAT core. Both models assume a flat ground modelled as an infinite dielectric ground plane (whose electrical properties can be changed in accordance with the type of environment). Due to the sensitivity of the MeerKAT receivers, validation of these numerical predictions was performed by comparison to measurements in the relatively simpler KAT-7 environment.

1.4 Contributions

Attenuation mapping of the environment of MeerKAT is the natural next step in EMC studies in the Karoo. This work integrates signal propagation and facility deployment to realise an accurate prediction tool. The following outputs form the core contributions of this research:

- *Evaluation of empirical propagation models*
  The (Longley-Rice) Irregular Terrain Model (ITM), Recommendation P.1546* of the International Telecommunication Union (ITU) and the Egli model are for the first time statistically evaluated for predictions in the Karoo. Even though some comparisons to measurements have been made previously, the validity of predictions has been called into question since the limits of error have been unknown. In this research, the degree of accuracy is quantified with respect to modelling in the Karoo. Considering both short (< 1 km) and long (> 1 km) ranges, P.1546 and ITM models are found to yield reliably conservative estimates (which is good from an RFI protection point of view) while the Egli model is unsuitable for low antenna heights (< 10 m).
- *Clarity on the free space loss approximation*
  Frequently, it is suggested that propagation loss trivially reduces to free space loss at short ranges [16–19]. While there are conditions under which this holds true, the research shows that this assumption is generally incorrect. Even at a path length of 20 m, free space loss (FSL) was around 15 dB lower than the measured transmission loss. Hence, FSL must be considered as the propagation loss benchmark defining worst case scenarios in the context of managing RFI.
- *Method of modelling real finite ground*
  Using the uniform theory of diffraction, a new and very efficient approach for modelling real ground is established. A thin perfect electrical conductor (PEC) sheet is coated with a dielectric layer corresponding to real ground parameters and the thickness set to $\lambda/2$. The novelty of this method is that it can be used to efficiently model terrain obstacles provided they can be represented using canonical shapes.
- *Deterministic modelling techniques for scattering in complex environments*
  An existing code based on the method of moments (MoM) was exploited with physical

*Method for point-to-area predictions for terrestrial services in the frequency range 30 MHz to 3 000 MHz

optics (PO) to realise a ray model for computing scattering from large metallic surfaces. The power of this ray model is its ability to reproduce a deployment scenario (physical configuration) with high accuracy.

- *Attenuation mapping of the MeerKAT Core*
  Using the ray model, numeric data were obtained which provide high spatial resolution results that would otherwise be extremely cumbersome to achieve. The attenuation maps that were generated yield invaluable insights, revealing regions of high and low sensitivity (corresponding to low and high loss, respectively). This has profound benefit for RFI protection in relation to identifying potential problem areas.
- *Empirical modelling for the MeerKAT core*
  Based on numeric data from the ray model, a path loss exponent was derived. This makes it possible to quickly obtain representative results for a path through the MeerKAT core using the log-distance formula.

1.5 Dissertation Layout

Radio propagation essentials are presented in Chapter 2 where propagation effects and transmission loss are discussed. Zeroing in on modelling, a few empirical models are introduced in their respective classifications as irregular terrain, mobile radio or foliage propagation models. The chapter ends by discussing deterministic methods, that is, full-wave and ray-tracing techniques.
In Chapter 3, the scope of propagation modelling in the MeerKAT environment is set. Diffraction and reflection are considered in more detail to reveal the impact these effects could have on the propagation of RFI. Metrics for statistical evaluation are introduced and applied to ITM, P.1546 and Egli models. The evaluation is based on measurements in the Karoo and highlights both successes and shortcomings of these empirical models.

Development and verification of a deterministic model is the focus of Chapter 4. Here, (the commercial CEM software) FEKO is discussed in some detail with regard to the relevant solvers as well as some essential features. A ray model is formulated, combining the method of moments (MoM) and physical optics (PO). Verification is performed by comparing the ray model predictions to measurements conducted at the KAT-7 environment. Using the verified ray model, the MeerKAT core is analysed and mapped in Chapter 5.
The dissertation concludes with a summary of the research in Chapter 6. This also provides recommendations for further development of this work. Additional information relating to the modelling, GIS data and Matlab scripts are provided in the appendices.

Chapter 2

Radio Propagation Essentials

Propagation studies play a key role in network planning and spectrum management with respect to evaluation, prediction and mitigation of interference. For a given radio link, losses can readily be predicted using empirical propagation models. However, these results could be misinterpreted easily without a proper understanding of the underlying principles. The fundamental aspects of radio propagation are thus introduced, beginning with the plane wave approximation. This flows into a description of the link (power) budget wherein transmission loss is the key parameter of interest. A summary of propagation mechanisms and the resultant effect is also presented. The chapter ends with an overview of propagation modelling which highlights some of the more popular empirical models. The concepts of deterministic modelling involving ray-tracing and full-wave methods are also briefly described.

2.1 The Plane Wave Approximation

Generation of time-varying electric fields by time-varying magnetic fields and vice versa is the basis on which electromagnetic (EM) energy is transmitted through a medium. Maxwell's equations provide a description of this phenomenon in terms of interactions of electric and magnetic fields as well as their relations to charges and currents [20]:

$$\nabla \times \mathbf{E} = -\mu \frac{\partial \mathbf{H}}{\partial t} \tag{2.1a}$$

$$\nabla \times \mathbf{H} = \sigma \mathbf{E} + \epsilon \frac{\partial \mathbf{E}}{\partial t} \tag{2.1b}$$

$$\nabla \cdot \mathbf{D} = \rho \tag{2.1c}$$

$$\nabla \cdot \mathbf{B} = 0\,, \tag{2.1d}$$

where $\mathbf{E}$ ($\mathrm{V\,m^{-1}}$) and $\mathbf{H}$ ($\mathrm{A\,m^{-1}}$) are the electric field and magnetic field intensities, $\mathbf{D} = \epsilon\mathbf{E}$ ($\mathrm{C\,m^{-2}}$) and $\mathbf{B} = \mu\mathbf{H}$ ($\mathrm{Wb\,m^{-2}}$) are the electric flux and magnetic flux densities, $\mathbf{J} = \sigma\mathbf{E}$ ($\mathrm{A\,m^{-2}}$) is the (conduction) electric current density and ρ ($\mathrm{C\,m^{-3}}$) is the electric charge density. The constants μ, σ and ϵ are respectively the permeability ($\mathrm{H\,m^{-1}}$), conductivity ($\mathrm{S\,m^{-1}}$) and permittivity ($\mathrm{F\,m^{-1}}$) of the medium. For the purpose of propagation studies the practice is to uncouple the $\mathbf{E}$ and $\mathbf{H}$ fields which in the case of source free ($\nabla \cdot \mathbf{D} = 0$) and lossless media ($\sigma = 0$) yield the wave equations [20, 21]

$$\nabla^2 \mathbf{E} = \mu\epsilon \frac{\partial^2 \mathbf{E}}{\partial t^2} \equiv -\omega^2 \mu\epsilon \mathbf{E} \tag{2.2}$$

and

$$\nabla^2 \mathbf{H} = \mu\epsilon \frac{\partial^2 \mathbf{H}}{\partial t^2} \equiv -\omega^2 \mu\epsilon \mathbf{H}\,, \tag{2.3}$$

where ω is the angular frequency ($\mathrm{rad\,s^{-1}}$) and the substitution $\partial/\partial t = j\omega$ has been used to obtain the equivalent time-harmonic form in the far right-hand expressions. For a given medium,

the coefficient of **E** or **H** in the wave equation defines the square of the phase constant (or wave number) k^*, that is, $\omega^2\mu\epsilon = k^2$. Closely related to this is the velocity of propagation given by $v = 1/\sqrt{\mu\epsilon} = \omega/k$. In a rectangular coordinate system, a solution for the electric field vector is $\mathbf{E}(x,y,z) = \hat{\mathbf{x}}E_x + \hat{\mathbf{y}}E_y + \hat{\mathbf{z}}E_z$ and (2.2) can be decomposed into three scalar Helmholtz equations in E_x, E_y and E_z of the form [22]

$$\frac{\partial^2 E_x}{\partial x^2} + \frac{\partial^2 E_x}{\partial y^2} + \frac{\partial^2 E_x}{\partial z^2} + k^2 E_x = 0\,, \tag{2.4}$$

with $E_x = E_x(x,y,z)$ in general. Separating variables by setting $E_x = f(x)g(y)h(z)$ yields simple-harmonic differential equations (DE's) whose solution is typically chosen as $e^{\pm jk_x x}$. Hence a solution for E_x is

$$E_x = A_x e^{\pm jk_x x \pm jk_y y \pm jk_z z} = A_x e^{\pm j\mathbf{k}\cdot\mathbf{r}}\,, \tag{2.5}$$

where A_x is an amplitude constant. Similar solutions exist for E_y and E_z and hence, by letting $\mathbf{E_0} = \hat{\mathbf{x}}A_x + \hat{\mathbf{y}}A_y + \hat{\mathbf{z}}A_z$, the electric field vector may generally be expressed in phasor form as [22]

$$\mathbf{E}(x,y,z) = \mathbf{E_0} e^{\pm j\mathbf{k}\cdot\mathbf{r}}. \tag{2.6}$$

Since a plus sign in the exponent of (2.6) represents a backward travelling wave (negative $\hat{\mathbf{r}}$-direction) while a minus sign indicates a forward travelling wave (positive $\hat{\mathbf{r}}$-direction), it is customary to write

$$\mathbf{E}(x,y,z) = \mathbf{E_0^+} e^{-j\mathbf{k}\cdot\mathbf{r}} + \mathbf{E_0^-} e^{+j\mathbf{k}\cdot\mathbf{r}}\,, \tag{2.7}$$

where generally $\mathbf{E}_0^+ \neq \mathbf{E}_0^-$.

EM waves are typically regarded as propagating isotropically from the source and thus characterised by spherical wave fronts. At any point on the wave front, the direction of propagation is given by the Poynting vector which in time-harmonic form is $\mathbf{S} = \frac{1}{2}\mathrm{Re}(\mathbf{E}\times\mathbf{H}^*)$. The Poynting vector is actually the power density ($\mathrm{W\,m^{-2}}$) of the wave at a particular point in a direction specified by the vector. Since the radius of curvature becomes very large far away from the source, the spherical wave fronts are approximated as straight lines (plane waves) [23, 24]. For simplicity it is often assumed that power flows in the z-direction. Hence, assuming the electric field only has an x-component, (2.7) becomes

$$E_x(z) = E_0^+ e^{-jkz} + E_0^- e^{jkz}, \tag{2.8}$$

Substituting (2.8) into the time-harmonic form of (2.1a) and solving for the magnetic field intensity yields [20, 21],

$$H_y = \frac{1}{\eta}\left(E_x^+ - E_x^-\right) = H_y^+ + H_y^-\,, \tag{2.9}$$

where $\eta = \sqrt{\mu/\epsilon}$ is the intrinsic impedance of the medium and is equal to the wave impedance, $Z_w = E_x^+/H_y^+ = -E_x^-/H_y^-$ in the case of transverse electromagnetic (TEM) and plane waves

*The phase constant is sometimes denoted by β such as in [20]

[20]. With $H = E/\eta$, the Poynting vector is simply

$$P_{\text{av}}^{z+} = \frac{1}{2} E_x^+ H_y^+ = \frac{|E_0^+|^2}{2\eta}. \tag{2.10}$$

This shows that the net flow of power is always positive for a wave travelling in the positive direction.

2.2 Transmission Loss

Wireless technology exploits antennas as the interface between the intervening medium and a given radio system. That is, electromagnetic energy is transmitted and received by means of antennas. Received signal strength depends on the power density of the propagated wave and the effective aperture (area) of the receiving antenna. For an isotropic radiator the power density is [23, 25, 26]

$$s_0 = \frac{p_t}{4\pi d_m^2}, \tag{2.11}$$

so that the power received by a loss-free isotropic antenna is [25]

$$p_{0r} = s_0 a_{e0r} = p_t \left(\frac{\lambda}{4\pi d_m}\right)^2, \tag{2.12}$$

where p_t is the power radiated by the transmitter, λ (m) is the signal wavelength, d_m (m) is the distance to the receiver and $a_{e0r} = \lambda^2/4\pi$ (m^2) is the effective aperture of an isotropic receiver [25, 27]. Under these idealised conditions, the ratio of transmitted to received power defines the spreading loss [26]

$$\frac{p_t}{p_{0r}} = \left(\frac{4\pi d_m}{\lambda}\right)^2 = \left(\frac{4\pi f d_m}{c}\right)^2, \tag{2.13}$$

which is more commonly called *free space basic transmission loss*, l_{bf}. In (2.13) f (Hz) is the carrier frequency while $c = f\lambda$ is the speed of light in a vacuum and is equal to the free space wave velocity

$$v_0 = \frac{1}{\sqrt{\mu_0 \epsilon_0}} = 2.998 \times 10^8 \,\text{m}\,\text{s}^{-1},$$

with $\mu_0 = 4\pi \times 10^{-7}$ H m^{-1} and $\epsilon_0 = 8.854 \times 10^{-12}$ F m^{-1}. In the case of root mean square (RMS) field values the power density can also be expressed as

$$s_0 = \frac{e_0^2}{\eta_0} \simeq \frac{e_0^2}{120\pi}, \tag{2.14}$$

where e_0 denotes the (linear) free space electric field and $\eta_0 = 376.73\,\Omega \simeq 120\pi\,\Omega$. Equating (2.11) and (2.14) and solving for e_0 yields [25]

$$e_0 = \frac{1}{d_m}\sqrt{\frac{\eta_0 p_t}{4\pi}} = \frac{\sqrt{30 p_t}}{d_m}. \tag{2.15}$$

Practical antennas are directive and as such concentrate energy in a particular direction. This translates to an apparent power increase described as gain, $g(\theta, \phi)$ [26, 27]. Taking the direction

of maximum gain, the power density for a practical transmitting antenna is thus

$$s = \frac{p_t g_t}{4\pi d_m^2} \tag{2.16}$$

in the direction of g_t. With the receiver's effective aperture given as $a_{er} = g_r \lambda^2 / 4\pi$ the power received is

$$p_r = p_t g_t g_r \left(\frac{\lambda}{4\pi d_m} \right)^2 \tag{2.17}$$

or equivalently in dB

$$P_r = \text{EIRP} + G_r - L_{bf}\,, \tag{2.18}$$

where L_{bf} is the spreading loss (2.13) in decibels and $\text{EIRP} = P_t + G_t$ is the equivalent isotropically radiated power. Transmit and receive gains, G_t and G_r, are expressed in dBi, that is, relative to the gain of an isotropic antenna. In view of the fact that propagation rarely occurs under free space conditions there is in general a loss l_m (or L_m) due to the intervening medium which must be included in (2.17) (or (2.18)) such that [24, 28]

$$P_r = \text{EIRP} + G_r - L_{bf} - L_m\,. \tag{2.19}$$

Neglecting circuit losses, the *transmission loss* is defined as

$$L = 10 \log \left(\frac{p_t}{p_r} \right) = P_t - P_r = L_b - G_t - G_r\,. \tag{2.20}$$

The term $L_b = L_{bf} + L_m$ is the *basic transmission loss* – the loss that would occur if isotropic, loss-free radiators were used in place of the actual antennas [29, 30]. It is typically the parameter of primary interest in propagation studies*.

2.3 Propagation Effects

Radio waves will be affected differently depending on the frequency of transmission as well as the properties and features of the surrounding medium (environment). Network planning often involves statistical evaluations of the power budget in respect of interference to ensure a sufficiently high signal-to-noise ratio over a communication link. Generally, the intervening path influences the propagation mode and the kind of effects that may arise.

2.3.1 Diffraction

An obstruction in the propagation path will absorb photons, creating a shadowed region away from the oncoming radiation. If the top edge of the obstacle is much smaller than a wavelength it is considered 'sharp' and the radio shadow will be filled in spite of the obstacle [23, 31]. Most obstacles encountered in propagation studies can be treated as thin sheets provided that

*In the literature, path loss is frequently discussed as a key parameter of the power budget (equation (2.19)) wherein it is used as a synonym for L_b (e.g. Seybold [23]). While this is accepted in more recent literature, in former times path loss was a 'normalization' of L by subtracting gain [29].

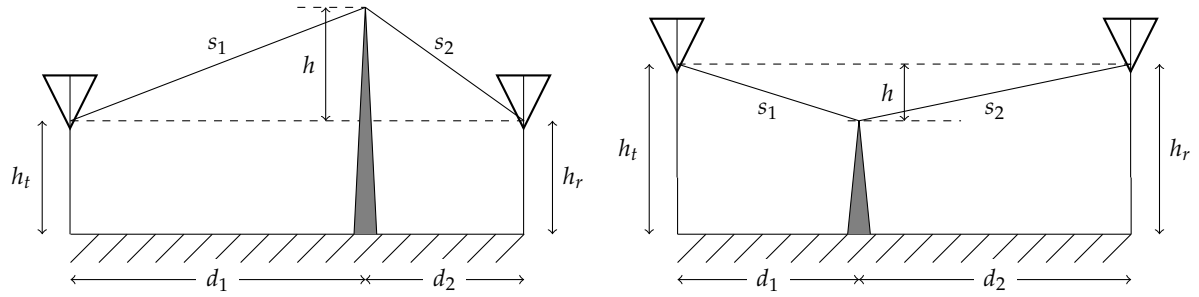

(a) positive h **(b)** negative h

Figure 2.1: Knife edge diffraction geometry (Adapted from [32])

the height h of the obstacle and the wavelength λ are both much smaller than the transmitter-obstacle and obstacle-receiver distances. Figure 2.1 illustrates basic knife-edge diffraction geometry for positive and negative clearance heights. Analysis of the configuration with respect to path difference, Δd, leads to the definition of the *Fresnel parameter* [23, 26, 33],

$$\nu_F = h\sqrt{\frac{2}{\lambda}\left(\frac{1}{d_1}+\frac{1}{d_2}\right)}, \tag{2.21}$$

such that the phase difference is given by

$$\Delta\phi = \frac{\pi}{2}\nu_F^2 . \tag{2.22}$$

Destructive interference occurs when

$$\Delta\phi = 2n\pi \implies \nu_F^2 = 4n\,, \quad n = 1, 2, 3, \ldots \tag{2.23}$$

that is, objects in even-numbered Fresnel zones are in phase opposition to the direct wave.

2.3.2 Reflection

Reflection occurs when an EM wave encounters an interface between two media. Due to wave impedance differences the incident radiation undergoes a change of direction whereby it is returned to the medium from which it originated [34]. A reflecting surface is regarded as smooth if irregularities are small in comparison to wavelength, giving rise to specular reflection. 'Rough' surfaces (structures with irregularities larger than the wavelength) give rise to diffuse reflection, also called scattering. Figure 2.2 illustrates the basic configuration of reflection in terrestrial radio links. The phase difference between the direct and reflected waves is

$$\Delta\phi = \frac{\omega}{c}\left(R_2 - R_1\right), \tag{2.24}$$

where

$$R_1 = d_m\sqrt{\left(\frac{h_t - h_r}{d_m}\right)^2 + 1} \tag{2.25}$$

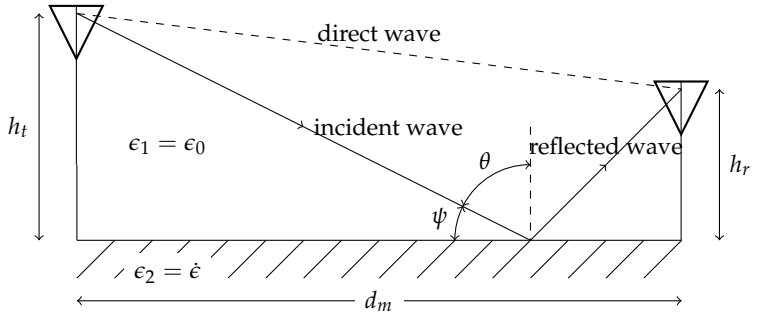

Figure 2.2: Geometry of ground-reflected waves

and

$$R_2 = d_m \sqrt{\left(\frac{h_t + h_r}{d_m}\right)^2 + 1} \tag{2.26}$$

are the lengths of the direct and reflected ray paths, while h_t and h_r are the transmitter and receiver heights (m) as before. The magnitude of the reflected wave depends on the reflection coefficient which in turn is a function of the ratio of the permittivity of the two media, polarization and angle of incidence. If the relative complex permittivity of the earth is $\dot{\epsilon}_r$, then the Fresnel reflection coefficients are [20, 35]

$$R_v = \frac{\dot{\epsilon}_r \sin\psi - \sqrt{\dot{\epsilon}_r - \cos^2\psi}}{\dot{\epsilon}_r \sin\psi + \sqrt{\dot{\epsilon}_r - \cos^2\psi}} \tag{2.27}$$

and

$$R_h = \frac{\sin\psi - \sqrt{\dot{\epsilon}_r - \cos^2\psi}}{\sin\psi + \sqrt{\dot{\epsilon}_r - \cos^2\psi}}, \tag{2.28}$$

for vertical (parallel) and horizontal (perpendicular) polarizations with

$$\psi = \arctan\left(\frac{h_t + h_r}{d_m}\right) \tag{2.29}$$

as the angle of incidence. Surface roughness is quantified using the Rayleigh criterion which in the simplest and idealised case is [23, 36]

$$H_R = \frac{\lambda}{8\sin\psi} = \frac{\lambda}{8\psi}, \tag{2.30}$$

where the far right-hand side is the approximation for small ψ. A surface is rough if H_R is greater than the difference Δh, between the mean surface height and the terrain features. This is based on the path length difference between AC and AB in the simplified geometry of Figure 2.3. If the variation in terrain can be described statistically the Rayleigh criterion is more precisely given as [35, 36]

$$C = \frac{4\pi\sigma_R \sin\psi}{\lambda} \simeq \frac{4\pi\sigma_R\psi}{\lambda} \begin{cases} < 0.1 & \text{for a smooth surface} \\ > 10 & \text{for a rough surface} \end{cases}, \tag{2.31}$$

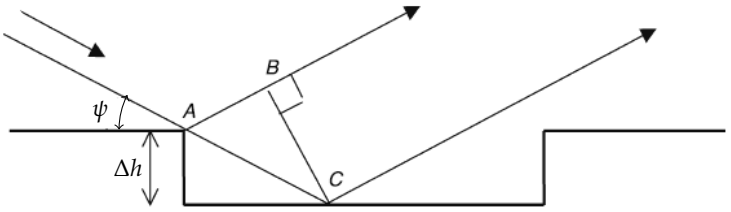

Figure 2.3: Simplified geometry for roughness criterion (Image credits: Bacon [34])

where σ_R is the standard deviation of the terrain variations relative to the mean surface height.

2.3.3 Multipath

Multipath occurs when there are two or more paths that a wave can travel towards a receiver. Differences in path length give rise to differences in phase which determine whether the waves cancel or reinforce. At a given frequency, constructive interference occurs when the path length difference is [37]

$$\Delta d = \left(n + \frac{1}{2}\right)\frac{c}{f}, \qquad n = 0, 1, 2, \ldots \tag{2.32}$$

which corresponds to a phase difference of

$$\Delta\phi = \frac{\omega}{c}\Delta d = (2n+1)\pi\,. \tag{2.33}$$

As a consequence of the superposition of multiple waves, multipath results in variations of frequency and amplitude as well as time delays. These effects are collectively referred to as *small-scale fading* [37, 38]. Such phenomena are particularly common in built up areas where line-of-sight (LOS) paths rarely exist.

2.3.4 Atmospheric Attenuation

At frequencies above 10 GHz the troposphere starts becoming lossy as a result of absorption and refraction. Absorption occurs when radio quanta collide with gaseous molecules (predominantly water vapour and oxygen), raising them to a higher energy state [28]. At 20 GHz the attenuation is approximately 0.2 dB km^{-1} and rises to $\sim$4 dB km^{-1} at 250 GHz. Due to resonance, strong absorption is observed around 60 and 119 GHz for oxygen (O_2), while water vapour (H_2O) exhibits strong peaks at 22, 183 and 325 GHz [26]. Hydrometeors (snow, hail, rain, clouds, fog) can also contribute significantly to path attenuation above 20 GHz but their effect is negligible below 5 GHz.

Variations of the refractive index, $n_t = \sqrt{\dot{\epsilon}_{rt}}$, of the troposphere result in ray paths that are longer than actual line-of-sight (LOS) ranges. To make the changes in n_t more apparent, it is customary to use the refractivity

$$N = (n_t - 1) \times 10^6\,, \tag{2.34}$$

Table 2.1: Frequency Allocations of the Radio Spectrum (Table credits: Seybold [23], Räisänen and Lehto [28])

Band Name	Frequency Range
very low frequency (VLF)	3 – 30 kHz
low frequency (LF)	30 – 300 kHz
medium frequency (MF)	300 – 3000 kHz
high frequency (HF)	3 – 30 MHz
very high frequency (VHF)	30 – 300 MHz
ultra-high frequency (UHF)	300 – 3000 MHz
super-high frequency (SHF)	3 – 30 GHz
extremely high frequency (EHF)	30 – 300 GHz

since n_t deviates only slightly from unity. The decrease of N with height is characterised as

$$N = N_s e^{-0.136h}, \tag{2.35}$$

where $N_s \simeq 300$ is the refractivity at the earth's surface under standard atmospheric conditions. Curvature is accounted for by defining an effective earth radius factor, k_e, whose value is $4/3$ under standard atmospheric conditions. Use of k_e allows for straight lines to be plotted for path profiles using the effective earth radius $a_e = k_e a$, where a is the earth radius.

2.3.5 Polarisation

Polarisation is not itself a propagation effect but has implications on signal strength and therefore range of transmission. By polarisation of an EM wave is meant *"the orientation of the plane in which the electric field resides* [23]." Linearly polarised waves are characterised as either aligned vertically (E-field in a plane perpendicular to the horizon) or horizontally (E-field in a plane parallel to the horizon). Provided they are orthogonal, a configuration comprising two linearly polarised waves with a phase difference of 90° gives rise to an elliptically polarised wave. If, in addition to a 90° phase shift the electric fields are also equal in magnitude, then the polarization will be circular [21, 26, 31]. Linear and circular polarizations are in fact regarded as special cases of elliptical polarization. A superposition of incoherent waves gives rise to a randomly polarised or simply an unpolarised wave. This is indeed the case for propagation via the ionosphere as a result of random variation in phase [21].
Polarisation is an important parameter to take into account as certain effects such as reflection may be minimized or enhanced depending on the orientation of the E-field.

2.4 Propagation Modes

The radio spectrum is divided into frequency bands on a per decade basis from 3 kHz to 300 GHz as listed in Table 2.1. Wireless services operate in various bands as predetermined by the nature of the service and this in turn has a bearing on the method of transmission.

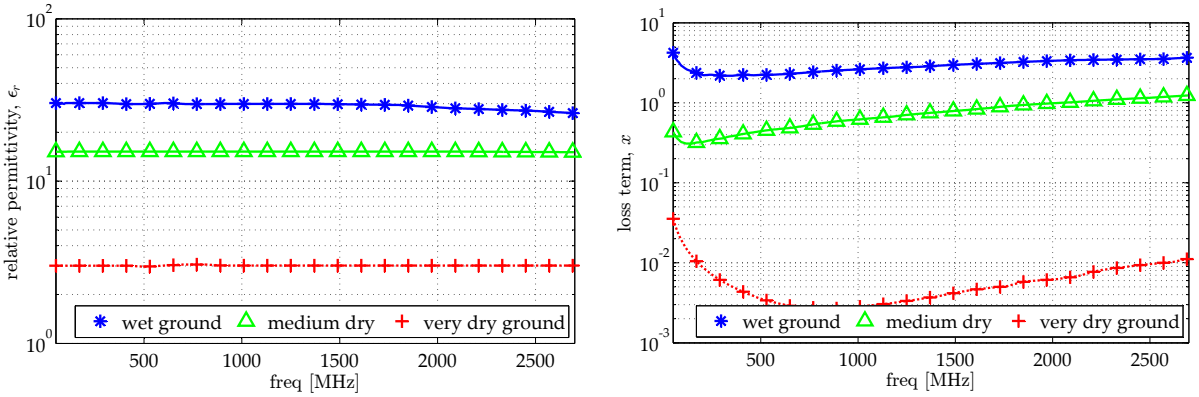

(a) relative permittivity **(b)** loss term

Figure 2.4: Real and imaginary parts of relative complex permittivity for wet, medium dry and very dry grounds. Data obtained from graphs presented in ITU-R P.527 [39].

2.4.1 Ground-wave Propagation

Radio wave transmission that takes place in the vicinity of the earth is called ground wave propagation. Three waves are to be considered in general: surface, direct and ground-reflected waves. Except for LF and MF bands, the contribution of the surface wave is negligible so that the received wave is predominantly the sum of the direct and ground-reflected waves, collectively called the space wave. In view of reflections, the electrical characteristics of the type of ground (dry, wet, water or ice) must be taken into account using the relative complex permittivity, $\dot{\epsilon}_r$. An expression for $\dot{\epsilon}_r$ is found by first writing the Maxwell-Ampere relation (2.1b) in time-harmonic form [34, 35]

$$\nabla \times \mathbf{H} = j\omega\epsilon\mathbf{E} + \sigma\mathbf{E} = j\omega\left[\epsilon - j\frac{\sigma}{\omega}\right]\mathbf{E} = j\omega\dot{\epsilon}\mathbf{E}\,, \tag{2.36}$$

where $\dot{\epsilon}$ is called the complex permittivity* that typifies the behaviour of a partially conducting dielectric. The relative complex permittivity can then be defined as

$$\dot{\epsilon}_r = \frac{\dot{\epsilon}}{\epsilon_0} = \epsilon_r - j\frac{\sigma}{\omega\epsilon_0} = \epsilon_r - jx\,. \tag{2.37}$$

Relative permittivity and the loss term x are shown in Figure 2.4 for three types of ground as provided in Recommendation P.527 of the International Telecommunication Union (ITU) [39].

2.4.1.1 Plane Earth Reflection

A simplified but practical approach to model ground-wave propagation is [40, 41]

$$\frac{e}{e_0} = 1 + Re^{-j\Delta\phi} + (1-R)\,Fe^{-\Delta\phi}\,, \tag{2.38}$$

where e and e_0 represent the received and free space electric fields, respectively. The term R represents the Fresnel reflection coefficients for vertical or horizontal polarization as shown in

*Strictly speaking complex permittivity is presented as $\dot{\epsilon} = \epsilon' - j\epsilon''$ [20]. However, in practice the macroscopic effect of the alternating field conductivity, $\omega\epsilon''$, is indistinguishable from the effect of σ.

(2.27) and (2.28); F is the attenuation factor defined as

$$F = \left\{1 - j\sqrt{\pi\nu}e^{-\nu}\left[\text{erfc}\left(j\sqrt{\nu}\right)\right]\right\}, \tag{2.39}$$

where erfc is the complementary error function. For vertical polarization, the term ν is given by

$$\nu_v = \frac{-j\omega d_m}{2\dot{\epsilon}_r c}\left(1 - \frac{\cos^2\psi}{\dot{\epsilon}_r}\right)\left[1 + \frac{\dot{\epsilon}_r \sin\psi}{\sqrt{\dot{\epsilon}_r - \cos^2\psi}}\right]^2, \tag{2.40}$$

while for horizontal polarization it is

$$\nu_h = \frac{-j\omega d_m}{2c/\dot{\epsilon}_r}\left(1 - \frac{\cos^2\psi}{\dot{\epsilon}_r}\right)\left[1 + \frac{\dot{\epsilon}_r^{-\frac{1}{2}} \sin\psi}{\sqrt{\dot{\epsilon}_r - \cos^2\psi}}\right]^2. \tag{2.41}$$

2.4.1.2 Surface Waves

Under the appropriate conditions, a surface wave exists at the boundary between two media, travelling bound to and in a direction tangential to the surface [28, 42]. In radio-wave propagation, this mode is 'activated' when antennas are close to the ground (relative to wavelength) such that the direct wave is cancelled by the reflected wave on account of a 180° phase shift between the two waves. This then leaves only the surface wave described analytically by the last term of (2.38) [43–45]. Surface waves are rapidly attenuated with increasing frequency and as such are primarily applicable for transmissions in the LF, MF and HF bands [28, 45]. Services utilising surface wave propagation include amplitude modulation (AM) radio broadcasting, long-distance shore to ship communications, radionavigation, short-range HF communication and high frequency surface wave radar (HFSWR) [45].
It is shown later (in Section 4.2.1.2) that for the scenarios of interest in this study it is not required to compute the contribution of the surface wave.

2.4.2 Sky-wave Propagation

Reflection off the ionosphere is utilised in high frequency (HF) transmissions over long distances, especially in international shortwave broadcasting. Aviation and shipping industries also utilise HF communications. Ionospheric reflection is actually the result of a series of refractions. Frequencies that are higher than the ionosphere's plasma frequency will not be refracted sufficiently to return to earth. While the conditions of free-space may be approached, there are space weather effects and ionospheric variability to contend with [23, 43].

2.4.3 Line-of-Sight (LOS) Propagation

Radio services operating in VHF, UHF, SHF and EHF bands generally require a straight, unobstructed path. This line-of-sight (LOS) configuration approximates free space if the antenna heights are at least tens of metres above the ground. However, atmospheric refraction cannot be neglected and diffraction effects may be present if there is even a partial obstruction in the path. Borrowing from ray theory techniques, a useful criterion for qualifying a link as an LOS

path is when no obstacle exists within an ellipsoid of radius [23, 28, 33]

$$F_1 = \sqrt{\frac{\lambda d_1 d_2}{d_1 + d_2}}, \tag{2.42}$$

where d_1 and d_2 are the respective horizontal distances from transmitter and receiver to an ellipsoid point (see Figure 2.1). The term F_1 is called the radius of the first Fresnel ellipsoid. VHF and UHF systems can also employ multipath propagation modes such as in mobile communications. In contrast, satellite communications (SHF and EHF bands) depend entirely on LOS paths wherein the main effect to consider is atmospheric attenuation.

2.5 Overview of Propagation Modelling

Propagation modelling is an important tool in the roll-out of a radio link with respect to assessing interference effects in the intervening path. The goal is to quantify the degree of signal degradation between wireless transceivers due to reflection, diffraction, scattering and other propagation phenomena besides spreading (free space) loss. The extent of signal degradation is measured by basic transmission loss, L_b, (also called path loss). It is a vital parameter for coverage mapping and spectrum management [23, 38]. Numerous path loss prediction tools utilizing theoretical, statistical, empirical and deterministic schemes have been developed over the last seven decades [46, 47]. This highlights the significance of propagation modelling in planning various types of wireless networks. Empirical models (synthesized based on measurements) tend to be most common due to their ease of implementation. However, the predictions quickly become inaccurate when they are employed in an environment other than the one on which the data is based. On the other end of the spectrum, deterministic models (derived from Maxwell's equations) offer high accuracy but require detailed information of the environment (site-specific) and are computationally expensive [47, 48].
Unsurprisingly, the vast majority of models focus on mobile radio services in urban areas as well as FM radio and television broadcast services. In the former case, propagation is typically by diffraction and scattering since there are seldom line-of-sight (LOS) paths. Consequently, a multipath environment exists since the received signal is a superposition of several delayed waves [49]. In this regime, multipath fading is particularly important and is accounted for using a Rayleigh probability distribution [28]. In the latter scenario, atmospheric scattering and refraction are the characteristic propagation effects, since the physical configuration involves transmitting (base) stations that are hundreds of metres high, with a coverage radius extending tens or hundreds of kilometres.

Modelling propagation is an attempt to satisfy the simplified link budget relation (2.19) restated here:

$$P_r = \text{EIRP} + G_r - L_b\,, \tag{2.43}$$

where

$$L_b = L_{bf} + L_m\,. \tag{2.44}$$

The term L_m is the loss due to reflection, diffraction or scattering depending on the propagation mode and surrounding medium* while (L_{bf}) is the spreading (free space) loss given as

$$L_{bf} = 10\log\left(l_{bf}\right) = 20\log\left(f\right) + 20\log\left(d\right) + 32.45\,, \tag{2.45}$$

where for practical purposes and henceforth, d denotes distance in kilometres (km) while frequency, f, is given in megahertz (MHz).
Propagation models strive to predict as accurately as possible the loss L_m. The general input parameters include frequency, antenna heights and transmitter-receiver (T-R) separation distance. More complex models such as the Longley-Rice Irregular Terrain Model (ITM) and the ITU-R P.452 model can incorporate terrain data in order to account for diffraction loss. Effectiveness of a model in predicting path attenuation depends on its input parameters as well as whether the model is applied within its coverage range. A wide survey of various models and how they predict L_b (more commonly denoted PL, for path loss in modern literature) is presented by Phillips *et al.* [46].

2.5.1 Terrain Models

2.5.1.1 Egli Model

Empirically-derived from data obtained in various cities around the United States, the Egli model is an irregular terrain prediction method based on the plane earth model. The average received power is computed from a direct and a reflected wave but with an adjustment to account for ground loss. The median path loss is [23, 50, 51]

$$L_E = 20\log(f) + 40\log(d) - 20\log(h_t) - \begin{cases} 10\log(h_r) + 76.3 & h_r \leq 10 \\ 20\log(h_r) + 83.9 & h_r > 10 \end{cases} \tag{2.46}$$

where h_t and h_r correspond to transmitter and receiver heights in metres as before and hereafter.

2.5.1.2 Longley-Rice Irregular Terrain Model

The Longley-Rice Irregular Terrain Model (ITM) attempts to account for propagation losses due to diffraction, refraction, soil and climatic conditions. It is a versatile, general purpose model with provision for both point-to-point and point-to-area predictions† in the range 20 MHz - 20 GHz [52]. Attenuation relative to free space basic transmission loss is denoted A_{ref} and given by [53, 54]

$$A_{\text{ref}} = \begin{cases} A_e + K_1 d + K_2\log(d) & \text{line-of-sight} \\ A_{ed} + m_d d & \text{diffraction} \\ A_{es} + m_s d & \text{scattering} \end{cases}. \tag{2.47}$$

*Small-scale fading effects are neglected here

†Point-to-point links involve a specific path between a transmitter and receiver while parametric results are obtained using point-to-area predictions [52] which may involve one transmitter and multiple receivers e.g. mobile radio communications

The coefficients A_e, K_1, K_2, A_{ed}, A_{es}, m_d and m_s are determined using the algorithms by Longley and Rice [53] and subsequently by Hufford [54]. Two-ray theory provides the physical basis for the computations in the LOS range while Fresnel-Kirchhoff theory is used to evaluate diffraction phenomena. Although it is a complex model, the ITM is appealing owing to historical success in planning television broadcasts and mobile radio during the 1970's. The capability to include terrain data makes it particularly powerful.
The ITM is actually an implementation of the Longley-Rice model by the National Telecommunications and Information Administration (NTIA) [23, 52, 55]. Other variants of the method include the Signal Propagation, Loss, And Terrain (*SPLAT!*) analysis package and Radio Mobile [56] while the Terrain Analysis Package (TAP) includes it as a module [57].

2.5.1.3 The ITU-R P.1546 Model

The International Telecommunication Union Radiocommunication Sector (ITU-R) recommendation P.1546 is a synthesis of previous recommendations (P.370[‡], P.529[§], P.1146[¶]) in order to address certain irregularities and inconsistencies that had been observed [58]. P.1546 is derived empirically from data collected in temperate climates (Europe and North America predominantly) [16]. The model is presented as tables of received electric field strength values and corresponding curves at nominal frequencies of 100, 600 and 2000 MHz for land and sea paths, and for time variabilities of 1%, 10% and 50%. The model is designed for a representative receiver height of 10 m while transmitter heights range from 10 to 3000 m. Interpolation to shorter path lengths and lower antenna heights is possible. Implementation can be with or without terrain information over distances of 1 km to 1000 km. The predictions are valid for frequencies spanning 30 to 3000 MHz.

2.5.2 Foliage Models

Attenuation due to vegetation may be a significant factor in certain propagation scenarios. Empirical vegetative attenuation formulae take the general form [59]

$$L_{\text{veg}} = A f^B d_v^C \,, \qquad \text{(dB)} \tag{2.48}$$

where f is the frequency, d_v (m) is the vegetation depth (length of path through foliage) and A, B and C are determined empirically. The values of the empirical parameters for a few models are summarized in the Table 2.2.

2.5.3 Models for Mobile Radio

Mobile communication normally involves RF transmission in built up environments where wave polarization, frequency, the height, geometry and density of buildings are particularly

[‡]VHF and UHF propagation curves for the frequency range from 30 MHz to 1 000 MHz

[§]Prediction methods for the terrestrial land mobile service in the VHF and UHF bands

[¶]The prediction of field strength for land mobile and terrestrial broadcasting services in the frequency range from 1 to 3 GHz

Table 2.2: Summary of foliage empirical attenuation models [23, 59, 60]

Model	f	d	A	B	C	Scenario
ITU-R P.833	MHz	<400 m	0.25	0.39	0.25	woodland
Weissberger	GHz	0 m – 14 m	0.45	0.284	1	dense vegetation
		14 m – 400 m	1.33	0.284	0.588	
COST235	GHz	<200 m	26.6	-0.2	0.5	out-of-leaf
		<200 m	15.6	-0.009	0.26	in-leaf

important [23]. Since base stations are elevated while (mobile) terminals are more or less at ground level, propagation in urban environments involves targets in a shadowed zone.

2.5.3.1 Okumura-Hata Model

Extensive measurements in Japan led to the development of the Okumura model which utilised empirically-derived curves. Hata formulated Okumura's curves into equations for ease of implementation. Considered practical and accurate, the Okumura-Hata model is ideal for large cells and can be applied to both urban and rural areas for distances of 1 to 20 km. Here, median path loss is expressed as [23, 26, 47, 61]

$$L_{\text{OH}} = \begin{cases} L_{\text{OH}}^{\text{urban}} & \text{for urban areas} \\ L_{\text{OH}}^{\text{urban}} - 2\left[\log(f_c) - 1.4472\right]^2 - 5.4 & \text{for suburban areas} \\ L_{\text{OH}}^{\text{urban}} - 4.78\left[\log(f_c)\right]^2 - 18.33\log(f_c) - 40.9 & \text{for open areas} \end{cases} \tag{2.49}$$

where

$$L_{\text{OH}}^{\text{urban}} = 69.55 + 26.16\log(f_c) - 13.82\log(h_b) - a(h_m) + \left[44.9 - 6.55\log(h_b)\right]\log(d)\,, \tag{2.50}$$

where f_c must be in the range 150 to 1920 MHz, h_b is the effective height of the base station (30 – 200 m) and h_m is the mobile antenna's effective height (m). The term $a(h_m)$ is the mobile height correction factor given by

$$a(h_m) = \left[1.1\log(f_c) - 0.7\right]h_m - \left[1.56\log(f_c) - 0.8\right]. \tag{2.51}$$

2.5.3.2 Walfisch-Ikegami Model

The Walfisch-Ikegami model is a composite realised by the European Cooperation in the field of Scientific and Technical Research (COST) project 231. Also known as COST-WI, the prediction method combines Walfisch and Bertoni's approach for modelling diffraction and scattering over rooftops [62] with the ray-theoretical method of Ikegami *et al.* for computing the mean field strength at street level [63]. Detail such as width and orientation of streets is thus included in the model. Predictions are valid in the range 0.02 to 5 km and frequencies between 800 and 2000 MHz, while base station height is restricted to within 4 to 50 m.

Loss over rooftops is modelled by the sum [47, 64]

$$L_{\text{ex}} = L_{\text{rts}} + L_{\text{msd}}, \tag{2.52}$$

where L_{ex} is the excess loss relative to free space basic loss, L_{rts} is the rooftop-to-street loss, and L_{msd} is the multi-screen diffraction loss. Rooftop-to-street loss depends on frequency, f, variation in height between base station and mobile receiver Δh_{m}, street width w, and orientation loss L_ϕ, given by the equation [47, 61]

$$L_{\text{rts}} = -16.9 + 10\log\left[\frac{f(\Delta h_{\text{m}})^2}{w}\right] + L_\phi, \tag{2.53}$$

where

$$L_\phi = \begin{cases} -10 + 0.354\phi & \text{for } 0° \leq \phi < 35° \\ 2.5 + 0.075(\phi - 35) & \text{for } 35° \leq \phi < 55° \\ 4.0 - 0.114(\phi - 55) & \text{for } 55° \leq \phi \leq 90° \end{cases}. \tag{2.54}$$

Multi-screen diffraction loss accounts for field reduction due to propagation between rows of buildings. It is computed using the building separation distance, b, a factor k_a representing the increase in path loss due to differences between base station and rooftop height as well as multi-screen diffraction loss factors, k_d and k_f, that dictate the dependence on distance and frequency, respectively. Thus, L_{msd} is given by [47, 51, 61, 65, 66]

$$L_{\text{msd}} = L_{\text{bsh}} + k_a + k_d\log(d) + k_f\log(f) - 9\log(b)\,. \tag{2.55}$$

With rooftop height represented by h_0 and defining $\Delta h_b = h_b - h_0$,

$$L_{\text{bsh}} = \begin{cases} -18\log\left[1 + \Delta h_b\right] & \text{for } h_b > h_0 \\ 0 & \text{for } h_b < h_0 \end{cases}, \tag{2.56}$$

$$k_a = \begin{cases} 54 & \text{for } h_b > h_0 \\ 54 - 0.8\Delta h_b & \text{for } h_b < h_0 \text{ and } d \geq 0.5\,\text{km} \\ 54 - 1.6\Delta h_b & \text{for } h_b < h_0 \text{ and } d < 0.5\,\text{km} \end{cases}, \tag{2.57}$$

$$k_d = \begin{cases} 18 & \text{for } h_b > h_0 \\ 18 - 15\dfrac{\Delta h_b}{h_0} & \text{for } h_b \leq h_0 \end{cases}, \tag{2.58}$$

$$k_f = \begin{cases} -4 + 0.7\left(\dfrac{f_c}{925} - 1\right) & \text{in medium tree density suburban} \\ & \text{areas and medium-sized cities} \\ -4 + 1.5\left(\dfrac{f_c}{925} - 1\right) & \text{in large cities} \end{cases}. \tag{2.59}$$

2.5.4 Deterministic Modelling

2.5.4.1 Ray-tracing Models

Geometrical optics (GO) is a model of light propagation in terms of rays (straight line paths) which may only be refracted or reflected. Diffracted rays are accommodated via the geometrical theory of diffraction (GTD). These models are applicable to high frequency (UHF and SHF bands) RF transmissions. The approach is to analyse individually all the possible propagation scenarios from a source. Significant mechanisms are then added to obtain a field strength estimate [26, 47]. Although highly accurate and capable of three-dimensional predictions, the GTD is not valid in the shadow region. However, the uniform theory of diffraction (UTD) – a derivative of the GTD – overcomes this limitation.

Ray-tracing (RT) models are efficient for electrically large problems. In principle, a RT model can incorporate all multipath mechanisms providing not only amplitude but phase and time delay information. Thus, system design of mobile networks frequently employs RT methods. The downside of RT models is that they are computationally taxing [47, 67].
The *image method* is one of two RT techniques whereby the ray path is determined via image generation of a source at every plane. The images in turn become secondary sources [47, 64] as illustrated in Figure 2.5. Accuracy of the image method is however limited to non-complex

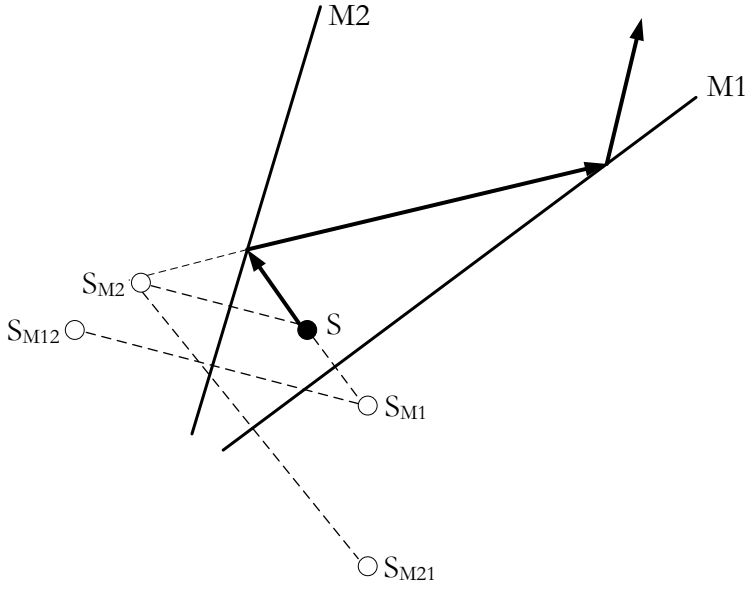

Figure 2.5: Ray trajectory for a source between two mirrors. Adapted from [47]

environments. The second RT approach involves launching rays in selected directions and is hence known as the *shooting-and-bouncing ray* (SBR) or ray-launching (RL) technique. Geometry and electrical properties of objects encountered determine which propagation effects are considered [47, 64]. Having taken all ray paths into account, the received field is computed as [68]

$$\mathbf{E}(Rx) = \mathbf{E}_{\text{ref}} \cdot \prod_{\nu=1}^{n} \mathrm{R}(\theta_i) \cdot \prod_{\mu=1}^{m} \mathrm{D}(\varphi, \varphi') A(\{\mathbf{r}_i\}) \exp\left[-jk \sum_i |\mathbf{r}_i|\right], \tag{2.60}$$

where $\mathbf{E}_{\text{ref}}$ is the field at a unit distance from the transmitter while R and D are dyadic[11] reflection and diffraction coefficients, respectively.

2.5.4.2 Full-wave Models

Ray-tracing models are not efficient at predicting scattered fields from lossy obstacles, particularly where electrically small objects are concerned. It is here that full-wave numerical solutions such as the Method of Moments (MoM) and the Finite-Difference Time-Domain (FDTD) can be used for accurate and detailed structure analyses [47]. Full-wave techniques offer solutions to Maxwell's equations with no *a priori* physical approximations. A solution may be obtained using either partial differential equations (PDE's) or integral equations. The PDE's may either be hyperbolic (wave equation) or parabolic (diffusion equation) with respect to the form of differential operator [69, 70]. Both PDE types can be solved using time-stepping methods such as the FDTD.

The parabolic equation (PE) is also known as the diffusion equation on account of wide application in modelling heat flow and processes involving transport of molecules along a gradient [71]. In electromagnetics, the PE can be derived as a two-dimensional solution to the scalar wave equation

$$\frac{\partial^2 \varphi}{\partial x^2} + \frac{\partial^2 \varphi}{\partial z^2} = -k_0^2 n_t^2 \varphi \,, \tag{2.61}$$

where φ is an EM field component, k_0 is the free space wave number and $n_t = \sqrt{\dot{\epsilon}_{rt}(x,z)}$ is the refractive index of the atmosphere. Forward propagation along the x-axis is assumed while height variation is given by the z-axis. Of interest is the scenario where wavelength is small compared to field variation and hence the field is chosen as $\varphi(x,z) = u(x,z)e^{jk_0 x}$, where u represents the amplitude of the EM field component. Since u is slow varying, the second order derivative with respect to x is negligible and (2.61) reduces to [68, 72]

$$\frac{\partial u}{\partial x} = \frac{1}{2jk_0}\left[\frac{\partial^2 u}{\partial z^2} + k_0^2\left(n_t^2 - 1\right)u\right] . \tag{2.62}$$

On account of n_t the PE (2.62) is well suited to modelling tropospheric propagation.

An integral equation (IE) of the form [68, 69, 73]

$$\frac{\varphi(\mathbf{r})}{2} + \oint_S \left[G(\mathbf{r},\mathbf{r}')\frac{\partial \varphi(\mathbf{r}')}{\partial n'} - \varphi(\mathbf{r}')\frac{\partial G(\mathbf{r},\mathbf{r}')}{\partial n'}\right] \mathrm{d}S' = \varphi^{\text{inc}}(\mathbf{r}) \tag{2.63}$$

can be derived from inhomogeneous Helmholtz equations of the EM field and an appropriate Green function, G, to solve for the unknown field φ given the incident field φ^{inc}. In (2.63), $\partial/\partial n$ is the normal derivative on the surface S and the primed values denote source coordinates. Boundary conditions may simplify the IE which is typically solved for the current density using the MoM.

[11] tensors of rank two

2.6 Summary

Radio propagation studies are multi-faceted and have varying complexity depending on the application. In this work the focus shall be on large-scale effects with basic transmission loss as the key parameter of interest. Consequently, the modelling objective is to minimize as much as possible the deviation between predicted and measured results for the loss due to environmental effects.

Empirical models frequently used in the context of surveys at the MeerKAT site have been introduced and will be examined in greater detail in the following chapter by way of evaluating their prediction accuracy.

Chapter 3

Evaluation of Selected Models

Typical radio frequency interference (RFI) control measures for radio observatories involve legislation (establishment of astronomy advantage areas and radio quiet zones), online/offline RFI removal from recorded data (subtracting, excising and filtering) and surveys to identify RFI culprits [74, 75]. In addressing self-generated RFI, good electromagnetic compatibility (EMC) practices play a critical role. For the Karoo Array Telescope (MeerKAT) much attention has been given to structure grounding and cable layout, since most (∼90%) RFI is associated with common mode (CM) currents [76]. Other EMC interventions include cable shielding arrangements exploiting Karoo soil and hardening of receptors against lightning.
Evidence from previous surveys and studies [11, 13] suggests that there is a need to probe signal propagation in the Karoo further in order to characterise the environment. Within this framework, suitable models for propagation studies must be established. Thus, with on-site measured data as the 'control', this chapter presents an evaluation of ITU-R P.1546, the Longley-Rice Irregular Terrain Model (ITM) and the Egli model for basic transmission loss predictions in the semi-desert Karoo region. Implementation of these models has previously not been verified for short (< 1 km) distances in an arid environment. The results presented here are an expansion and correction of the evaluation performed by Phiri *et al.* [77].

3.1 Interference Phenomena

The objective in modelling propagation for the Karoo SKA site is to characterise the environment rather than ensure (network) coverage. Consequently, fading, attenuation due to atmospheric gases, atmospheric refraction, weather effects (rain) and variations in time are not considered in this study. Atmospheric absorption becomes significant above 10 GHz while atmospheric refraction is of concern in terrestrial links. Diffraction, reflection and multipath are thus the propagation effects of interest in this work.

3.1.1 Diffraction Effects

Over large distances diffraction may occur due to the apparent protrusion of the surface (earth bulge). However, for the configurations of interest ($d < 1$ km and $h_t, h_r < 10$ m) smooth earth diffraction is zero. For 'simple', isolated obstacles the knife-edge approximation introduced in Section 2.3.1 is used to model diffraction loss as [26, 33]

$$L_d(\nu_F) = 6.9 + 20\log\left(\nu_F - 0.1 + \sqrt{(\nu_F - 0.1)^2 + 1}\right), \tag{3.1}$$

where L_d is a contribution to the loss L_m in (2.44). As before, $\nu_F = h\sqrt{2(d_1 + d_2)/\lambda d_1 d_2}$ is the Fresnel parameter while d_1 and d_2 are the respective distances (m) from the top of the obstacle to the antennas. The height h is the diffraction point as measured above or below the line-of-

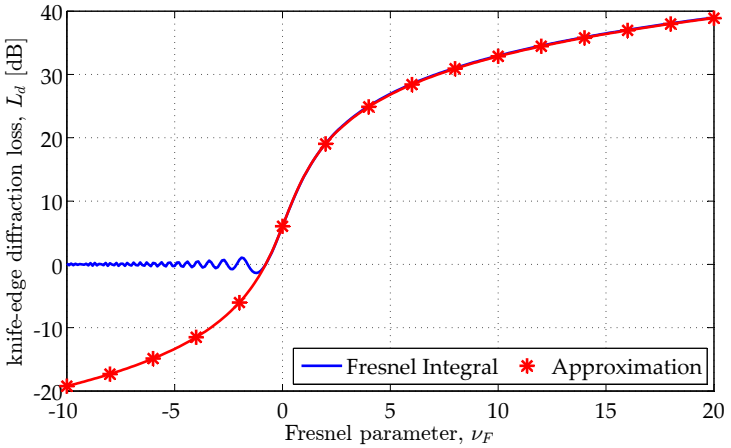

Figure 3.1: Knife-edge diffraction loss as a function of Fresnel parameter

sight (LOS) path. By definition, h represents the radius of a Fresnel ellipsoid and hence can be computed using (2.42), namely

$$h = F_n = 547.7\sqrt{\frac{n}{f}\cdot\frac{d_1 d_2}{d_1+d_2}}, \qquad \text{(m)} \tag{3.2}$$

where $n = 1, 2, 3, \ldots$ refers to a Fresnel zone, f is in megahertz, d_1, d_2 are in kilometres and it is assumed $d_1, d_2 \gg h$. The approximation (3.1) is valid for $\nu_F > -0.78$ [32, 33] otherwise diffraction can be regarded as zero on account of the behaviour of the explicit expression

$$J(\nu_F) = \frac{1 - C(\nu_F) - S(\nu_F) + j\left[C(\nu_F) + S(\nu_F)\right]}{2} \tag{3.3}$$

when $\nu_F < -0.78$. This can be seen in Figure 3.1.The functions $C(\nu_F)$ and $S(\nu_F)$ are the real and imaginary parts of the complex Fresnel integral

$$F(\nu_F) = \int_0^{\nu_F} e^{j\pi s^2/2} \mathrm{d}s\,. \tag{3.4}$$

It is clear that knife-edge diffraction loss will increase with frequency since $\nu_F \propto \sqrt{f}$ by reference to (2.21) and Figure 3.1.

More complex obstacles can be modelled by appropriate modifications to the single-obstacle model such as applying knife-edges in succession. For an obstruction with a rounded top, an attenuating factor accounting for curvature is added to (3.1) [33]. On the other hand, over intermediate terrain, diffraction loss can be computed as a function of path clearance [78]:

$$L_d = -20\left(\frac{h_c}{F_1}\right) + 10\,, \qquad \text{(dB)} \tag{3.5}$$

where

$$F_1 = 547.7\sqrt{\frac{d_1 d_2}{f(d_1+d_2)}} \tag{3.6}$$

is the radius of the first Fresnel zone and h_c is the clearance height such that $h_c < 0$ denotes blockage. Strictly speaking, (3.5) is only valid when the loss is above 15 dB but can be used

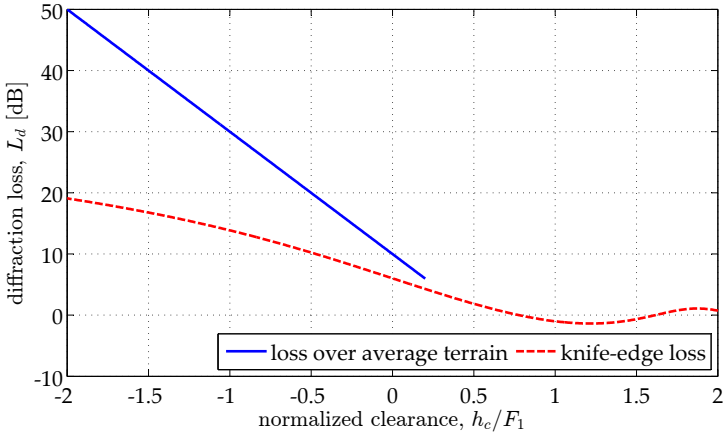

Figure 3.2: Diffraction loss over intermediate terrain. Knife-edge is included as a reference where $\nu_F = -h_c/F_1$.

down to 6 dB [78]. Figure 3.2 shows the diffraction loss over average terrain alongside knife-edge loss plotted against normalized clearance h_c/F_1. Values of $h_c/F_1 > 0$ indicate that the obstruction is below the LOS path. Diffraction effects cause signal attenuation and thereby increase loss by decreasing interference. If it is determined that diffraction must be accounted for, the values obtained are added to the (basic) transmission loss.

3.1.2 Reflection and Multipath Effects

For most configurations, wave reflections generally have the effect of increasing the resultant signal (decreasing loss). Reinforcement or cancellation of the waves depends on the path length difference, Δd, between the direct and reflected waves:

$$\Delta d = \frac{n\lambda}{2} = \frac{150n}{f} \begin{cases} n = 1,3,5... & \text{for reinforecement} \\ n = 2,4,6... & \text{for cancellation} \end{cases} . \tag{3.7}$$

With respect to the physical configuration, expanding (2.25) and (2.26) using the binomial expansion leads to the path length difference approximation

$$\Delta d = R_2 - R_1 \simeq \frac{2h_t h_r}{d_m} \tag{3.8}$$

which corresponds to a difference in phase of

$$\Delta\phi = k\frac{2h_t h_r}{d_m} = \frac{\pi f}{75}\frac{h_t h_r}{d_m}, \tag{3.9}$$

where $k = 2\pi/\lambda$ and f is in MHz. Equations (3.8) and (3.9) apply when $d_m \gg ht, hr$, that is when ψ is small. From (2.38), the field due to direct and reflected waves can be computed as

$$e_{\text{ref}} = \frac{e}{e_d} = 1 + Re^{-j\Delta\phi}, \tag{3.10}$$

where

$$e_d = \sqrt{\eta_0 p_r}\, e^{-jkR_1} = \frac{c}{4\pi f}\frac{\sqrt{\eta_0 p_t g_t g_r}}{R_1} e^{-jkR_1},$$

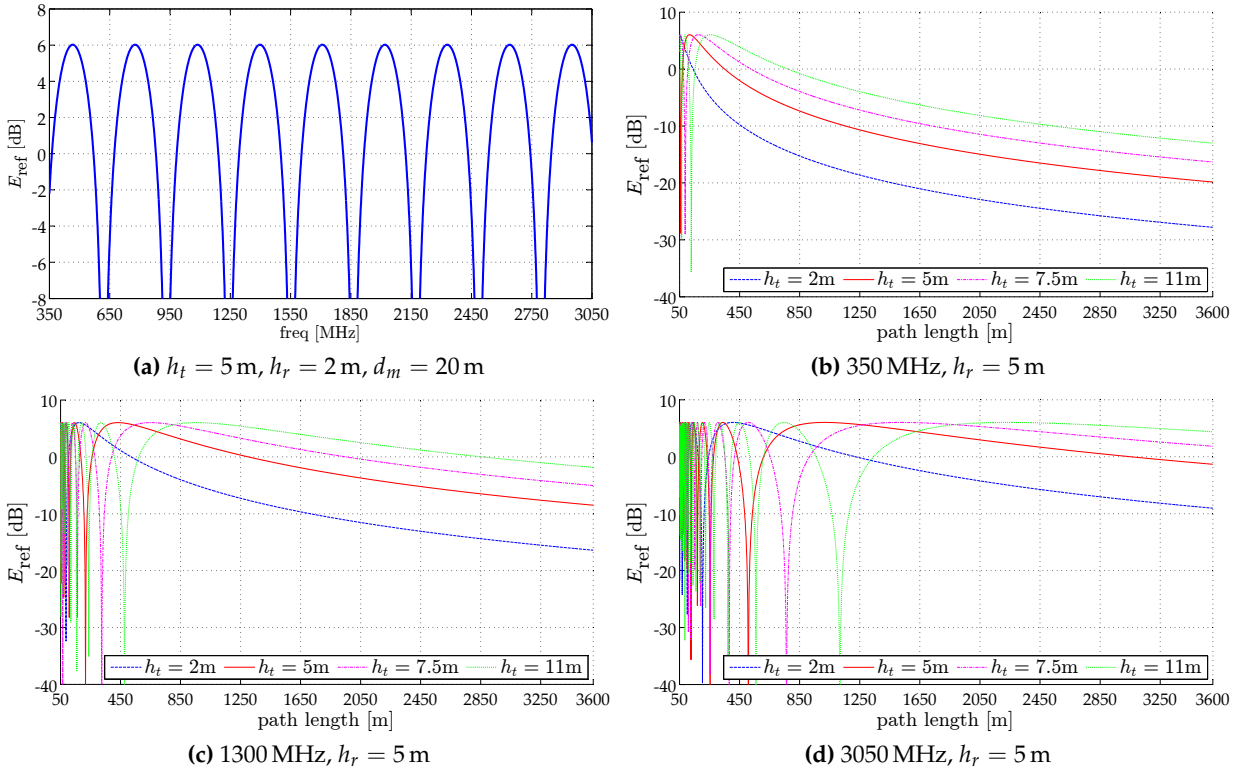

(a) $h_t = 5\,\text{m}$, $h_r = 2\,\text{m}$, $d_m = 20\,\text{m}$

(b) 350 MHz, $h_r = 5\,\text{m}$

(c) 1300 MHz, $h_r = 5\,\text{m}$

(d) 3050 MHz, $h_r = 5\,\text{m}$

Figure 3.3: Magnitude of received field relative to the free space field given a single reflection. For the same frequency, the smaller the path length difference, the more the received field fades and peaks.

is the direct field received by an antenna of gain g_r due to the numeric EIRP, $p_t g_t$. Because of slow variation, the approximation $R_2 = R_1$ is used in the amplitude term of (3.10). On the assumption of grazing incidence, $R_v = R_h = -1$ and the magnitude of the received field relative to free space is [36, 66]

$$|e_{\text{ref}}| = \left[(1-\cos\Delta\phi)^2 + \sin^2\Delta\phi\right]^{\frac{1}{2}} = 2\sin\frac{\Delta\phi}{2} = 2\sin\left(\frac{\pi f h_t h_r}{150 d_m}\right). \tag{3.11}$$

In terms of power, this translates to a gain of 6 dB (Figure 3.3a) when there is reinforcement ($\Delta\phi/2 = n\pi/2$, odd n) since $p_r \propto |e_{\text{ref}}|^2$. Evidently from Figure 3.3, for a single frequency transmission more nulls (lobes) occur the higher the frequency (shorter wavelength) and smaller path length differences. For a fixed path length difference, fading will be observed at a frequency interval of $300/\Delta d$ MHz. Basic transmission loss in the case of the interaction between direct and reflected waves becomes

$$L_r = 10\log\left[\left(\frac{\pi f d_m}{75}\right)^2 \frac{1}{|e_{\text{ref}}|^2}\right] = L_{bf} - 20\log\left(|e_{\text{ref}}|\right), \tag{3.12}$$

where subscript r indicates reflection. Deviation of L_r from L_{bf} is shown in Figure 3.4. Path length difference decreases with increasing range and this results in a larger frequency interval over which fading and peaking happens. The result is at a certain range, the plane earth reflection loss, L_r, will be greater than free space loss.

Returning to Figure 3.3, it is apparent that for a given configuration there is a particular range after which fades cease to occur. In terms of single frequency transmissions, this distance cor-

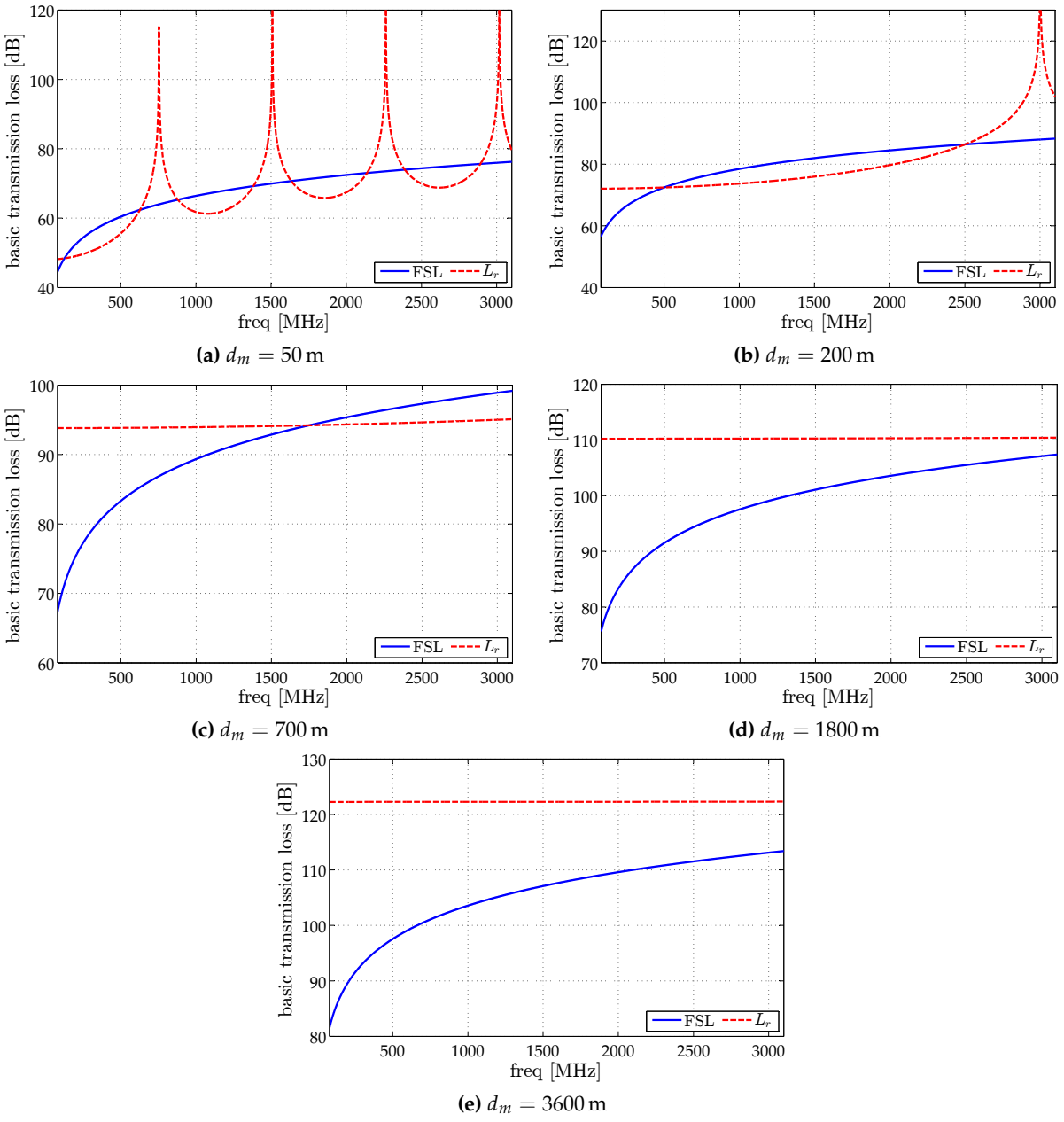

(a) $d_m = 50\,\text{m}$ **(b)** $d_m = 200\,\text{m}$

(c) $d_m = 700\,\text{m}$ **(d)** $d_m = 1800\,\text{m}$

(e) $d_m = 3600\,\text{m}$

Figure 3.4: Variation of basic transmission loss for ground reflections. With $h_t = 5\,\text{m}$ and $h_r = 2\,\text{m}$, in (a) $\Delta d = 39.77\,\text{cm}$ and nulls occur every 754 MHz; (b) $\Delta d = 10.0\,\text{cm}$ and nulls occur every 3001.1 MHz; (c) $\Delta d = 2.86\,\text{cm}$ and nulls occur every 10.5 GHz; (d) $\Delta d = 1.11\,\text{cm}$ and nulls occur every 27.0 GHz; (e) $\Delta d = 0.56\,\text{cm}$ and nulls occur every 54.0 GHz.

responds to the last field maximum occurrence and is called the breakpoint, d_b [66], defined by $\Delta\phi/2 = \pi/2$. Thus,

$$d_b = \frac{f h_t h_r}{75}. \tag{3.13}$$

For $d_m > d_b$, $|e_{\text{ref}}|^2 \simeq 4(\pi f h_t h_r / 150 d_m)^2$ since the field no longer fades and peaks, and the ratio of received to transmitted power can be approximated as

$$\frac{p_r}{p_t} = 4\left(\frac{\pi f h_t h_r}{150 d_m}\right)^2 g_t g_r \left(\frac{75}{\pi f d_m}\right)^2 = g_t g_r \left(\frac{h_t h_r}{d_m^2}\right)^2, \tag{3.14}$$

from which it is clear the basic transmission loss is

$$l_p = \left(\frac{d_m^2}{h_t h_r} \right)^2 \tag{3.15}$$

or equivalently

$$L_p = 40\log(d) - 20\log(h_t) - 20\log(h_r)\,, \tag{3.16}$$

The result in (3.14) is referred to as the plane earth equation. It is valid in the limit where $d_m \gg h_t, h_r$ such that $\sin(\Delta\phi/2) \simeq \Delta\phi/2$. Equations (3.14) and (3.15) indicate that after the breakpoint transmission loss will depend only on the physical configuration (geometry) of the path given reflection as the dominant propagation mechanism.

When there are three or more paths energy can travel towards a receiver, the vectorial combination of these waves produces unpredictable patterns due to time and path length differences. It will be shown later in Chapters 4 and 5 that a multipath environment does exist in the 'canyon' of receptors at KAT-7 and MeerKAT, respectively. Because of the presence of a LOS path, it would be natural to consider characterising the fading by a Ricean (also Rician in the literature) distribution or equivalently the Ricean factor [25, 36, 38]

$$K = 10\log\left(\frac{A^2}{2\varsigma^2} \right)\,, \tag{3.17}$$

where A is the peak amplitude of the direct (dominant) signal and ς^2 is the variance of the received signal. However, Ricean statistics address the probability of the fades exceeding a certain value [23] and this is not required here.

3.2 Prediction Evaluation Metrics

Objective assessment of a propagation model requires error analysis in terms of statistical metrics. Perhaps it is easiest to track variability by means of the standard deviation (SD), ς (dB), of the prediction error between measured and modelled results [48, 79–81]. An alternative and more representative metric is the root mean square error (RMSE) since it compares the predictions to measured results directly rather than through dispersion of the mean prediction error as with the SD.

3.2.1 Prediction Error and Root Mean Square Error

The prediction error, ε, is the most basic of metrics in evaluating a propagation model. It is the difference between the measured* and predicted values of path loss, namely [15, 81, 82]

$$\varepsilon_{m,i} = PL_{\text{meas},i} - PL_{m,i}, \qquad i = 1, 2, ..., N \tag{3.18}$$

where subscript m denotes a model and and N is the number of samples (frequency or distance)

*Ideally the mean of several measurements

points. It is more useful to quote the mean of (3.18) in describing model performance. However, this can lead to erroneous conclusions if a model over-predicts the loss in certain regions and under-predicts in other others. Hence, here mean prediction error will actually be the mean of the absolute values of the (3.18):

$$\bar{\varepsilon}_m = \frac{1}{N}\sum_{i=1}^{N}|\varepsilon_{m,i}| \ , \qquad \text{(dB)} \tag{3.19}$$

The associated standard deviation is [81]

$$\varsigma_{\bar{\varepsilon}_m} = \sqrt{\frac{\sum_{i=1}^{N}\left(\varepsilon_{m,i}-\bar{\varepsilon}_m\right)^2}{N-1}}. \qquad \text{(dB)} \tag{3.20}$$

A more quantitative description of a model's performance is the RMSE defined as [15, 82]

$$\text{RMSE} = \sqrt{\frac{1}{N}\sum_{i=1}^{n}\varepsilon_{m,i}^2}\,. \qquad \text{(dB)} \tag{3.21}$$

It is a metric of deviation from the measured value and in this way serves as the standard error of the predictions. It is the key metric of interest in this study.

3.2.2 Relative Error and Accuracy

Relative Error (RE) is the magnitude of the prediction error weighted by the measured (true) value of path loss. It is the fractional error

$$\text{RE}_m = \frac{1}{N}\sum_{i=1}^{N}\frac{|\varepsilon_{m,i}|}{PL_{\text{meas},i}}, \tag{3.22}$$

from which the average accuracy $A_m = (1-\text{RE}_m)\times 100$, can be calculated. The accuracy provides a confidence level for a model's prediction for a given measurement configuration (or parameter space).

3.2.3 Correlation Coefficient

Linear closeness between measurement and predictions is determined by the correlation coefficient [81, 83]

$$\rho = \frac{N\sum_{i=1}^{N}PL_{\text{meas},i}PL_{m,i} - \sum_{i=1}^{N}PL_{\text{meas},i}\sum_{i=1}^{N}PL_{m,i}}{(N-1)\sum_{i=1}^{N}PL_{\text{meas},i}\sum_{i=1}^{N}PL_{m,i}}. \tag{3.23}$$

It must be noted here that strong correlation does not necessarily mean a model performs well but rather indicates that the model exhibits similar trends as the measured data. Thus the correlation coefficient must not be used in isolation but rather in tandem with RMSE.

3.3 Propagation Models for the South African SKA Site

The question of which propagation models are most suitable for predictions in the Karoo has arisen frequently within the context of the SKA. Jessner *et al.* [76] recommend ITU-R P.526 (Propagation by Diffraction) to compute diffraction for ranges greater than 1 km. This is not directly relevant as the primary purpose here is to investigate path loss predictions at short ranges (<1 km). Owing mostly to ease of implementation, P.1546 and Egli models have found application in reports and studies, albeit to conceptualize actual requirements [11, 13, 76]. Predictions involving the more complex Longley-Rice model as implemented in *SPLAT!* have been reported by EMC Consultants MESA Solutions [13, 84]. It has generally been stated that results are satisfactory but there has been no analysis to ascertain the degree of accuracy or lack thereof. This was the primary objective of the evaluation of ITM, P.1546 and Egli models undertaken by Phiri *et al.* [77].

It should be noted that this evaluation considers only generic (or point-to-area) predictions which require only frequency and geometrical information (antenna heights and path length) for input data. If the model has the capability, electrical soil parameters (complex permittivity) can be used in the predictions. Of the models evaluated, only the ITM had this provision and this was limited to frequency-independent values corresponding to average, poor and good grounds*. Justification for this choice in modelling is that the available data were measured over relatively flat terrain such that the main effect would be reflection. In addition, this way all the models are evaluated under similar conditions.
A correction is required for P.1546 with respect to basic transmission loss computation. The documentation prescribes the formula [16]

$$L_b = 139.3 - E + 20\log(f)\,, \tag{3.24}$$

where E is the received field in dBµV and f is in MHz. Since this is based on the assumption of effective radiated power (ERP) equal to 1 kW, a receiver gain of 2.14 dB must be added to (3.24) otherwise the result is not precisely basic transmission loss.

3.3.1 Measurement Environment and Procedure

The data used here are a subset of a terrain loss survey conducted at the MeerKAT site during July 2014. The campaign was driven by EMC specialists MESA Solutions who have been consulting for the SKA-SA. Although these data have been reported previously [13], the presentation and analysis here is unique to this dissertation.

The approach was to inject a fast-rising time domain (TD) pulse into the transmitting antenna (R&S LPDA for 80 - 1000 MHz; EM-7020 horn for 1000 - 2500 MHz). The receiving unit consisted of an LPDA connected to a real-time analyser (RTA) – an improved iteration of the sampling system developed by Botha [85] – from which frequency domain (FD) data was obtained

*The respective relative permittivities are 15, 4 and 25, while the conductivities are 0.005, 0.001 and 0.020 S/m

Table 3.1: Equipment used for on-site measurements in the Karoo during July 2014.

Equipment	Function	Gain	BW/Freq [MHz]
CPS1	pulser (2.5 kV)	-	6000
R&S HL033	Tx	6.5 dBi	80 – 2000
EM-7020		12 dBi	1000 – 2500
R&S HL023	Rx	6 dBi	80 – 1300
GLPDA‡		5 dBi	176 – 8000
RTA	TD sampler	-	80 – 2500

in four frequency bands† via a Fourier transformation computed within the RTA itself. Cable loss at the transmitting end was calibrated out by connecting the output of the pulse generator directly into the RTA to determine the power received at the antenna terminals. On the receiving end, cable loss was compensated for during data processing. A summary of the equipment used is provided in Table 3.1.

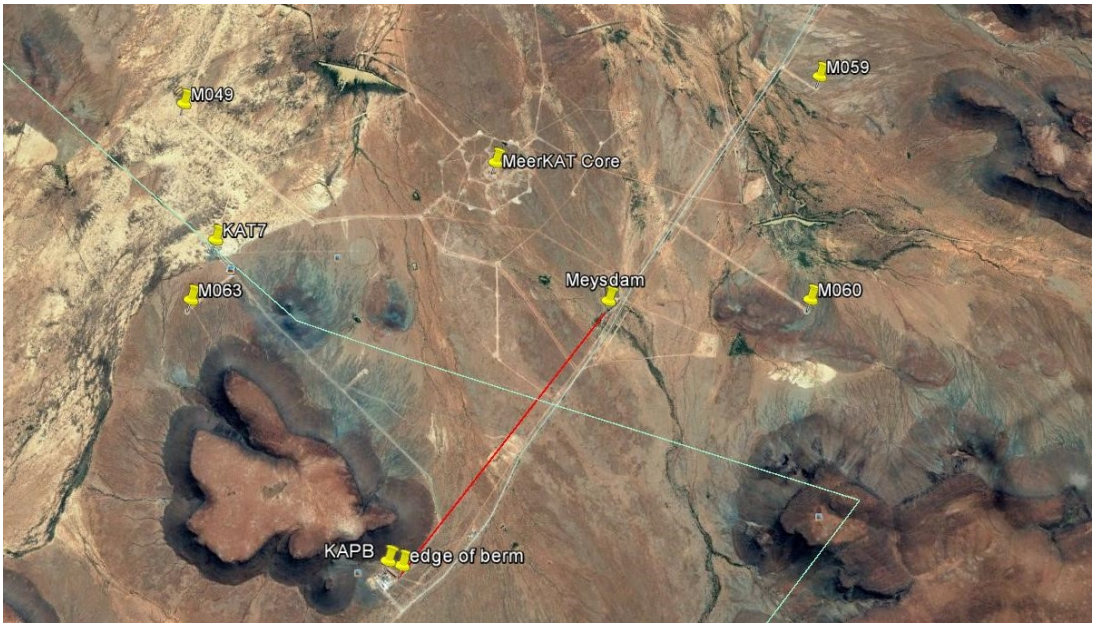

Figure 3.5: Overview of the MeerKAT site. The hill at the bottom-left of the picture is Losberg at whose edge are marked the Karoo Array Processor Building (KAPB) and the edge of the artificial berm. KAT-7 and the MeerKAT core lie approximately in north-north west (NNW) and north-north east (NNE) directions from the KAPB, respectively. Image credits: Google Earth

Figure 3.5 shows a satellite image of the MeerKAT environment. As can be seen, the site is surrounded by several hills but is otherwise flat. The hills provide a measure of shielding (via diffraction) especially to signals of external origin. Propagation measurements were performed for vertical polarization at distances of 50, 200, 700, 1800 and 3600 m along the path indicated by the (red) line from 'edge of berm' to 'Meysdam' in Figure 3.5. At each distance, data were

†80 - 850 MHz; 850 - 1050 MHz; 1050 - 1700 MHz; 1900 - 2500 MHz

‡printed circuited board log-periodic dipole array (PCB-LPDA) developed specially for the SKA-SA by Dr P. Gideon Wiid at the E&E Department, Stellenbosch University

recorded for transmitter heights (h_t) of 5 and 7.5 m while the receiver height (h_r) was fixed at 2 m. These two sets of measurements were respectively dubbed dataset-1 (DS1) and dataset-2 (DS2), and are the basis on which the models were evaluated. It should be noted that at the time of measurement, the RTA sampling was not seamless across the respective frequency bands. The gaps were filled in by interpolation using a kriging (Gaussian process regression) method [86].

3.3.2 Observations and Statistical Analysis

The curves in Figures 3.6 and 3.7 show the measured and predicted values of basic transmission loss for the two datasets, respectively. Decisive conclusions cannot be drawn based on eye inspection, but suffice to make the following general observations:

- Even at the shortest path length, the measured basic transmission loss is at least 15 dB higher than free space loss.
- The best-fit model at one range is not necessarily the best for other path lengths.
- At 50 and 200 m the measured data exhibit the characteristic increase in loss with frequency. A limiting value is approached around 1000 MHz when $d \geq 700$ m.
- ITM and P.1546 predictions are generally favourable at all ranges. However, P.1546 is clearly not ideal for very short ranges ($\sim$50 m) since the primary input in the interpolation utilises free space electric field values [16]. For $d \geq 700$ m neither ITM nor P.1546 model the lower frequencies well but start to converge with the measured data at around 1500 MHz.
- Egli and Egli-2 models perform poorly for the most part. Both Egli predictions yield favourable results at 200 m, with the Egli-2 model also following the trend fairly well at 700 m.

Tables 3.2 and 3.3 summarize the results, showing quantitative (prediction error, SD, RMSE) and qualitative (relative error, accuracy, correlation coefficient) statistics for the models under consideration. Quantitative analysis relates to the extent of deviation (spread) from the measured data while qualitative metrics describe model performance with regard to underlying trends.

Comments on Dataset 1

For rural areas, the acceptable RMSE margin is 10 - 15 dB [15, 83]. In this respect, the free space loss (FSL) model is the worst performing with an overall RMSE of 19.27 dB. The Egli model yields acceptable RMSE values for path lengths under 700 m but falls short otherwise. Best performance was at 50 m where a relative error (RE) of 0.11 and RMSE of 5.62 dB were achieved. On the other hand, the Egli-2 model satisfied the criteria for acceptable predictions at all ranges. At 200 m, Egli-2 had an impressive prediction quality yielding a RE of 0.02 (or accuracy of 97.73%), while the RMSE was 2.57 dB. P.1546 had the second best overall RMSE of 6.86 dB although the prediction at 50 m was poor (11.56 dB RMSE, 0.14 RE). Otherwise, performance of P.1546 is consistent and good at all distances as seen in the low values of RE (≤ 0.05 except at 50 m). With an overall RMSE of 6.90 dB the ITM was the best-performing model under DS1. This can also be seen in the overall relative error of 0.05 which translates to the best overall

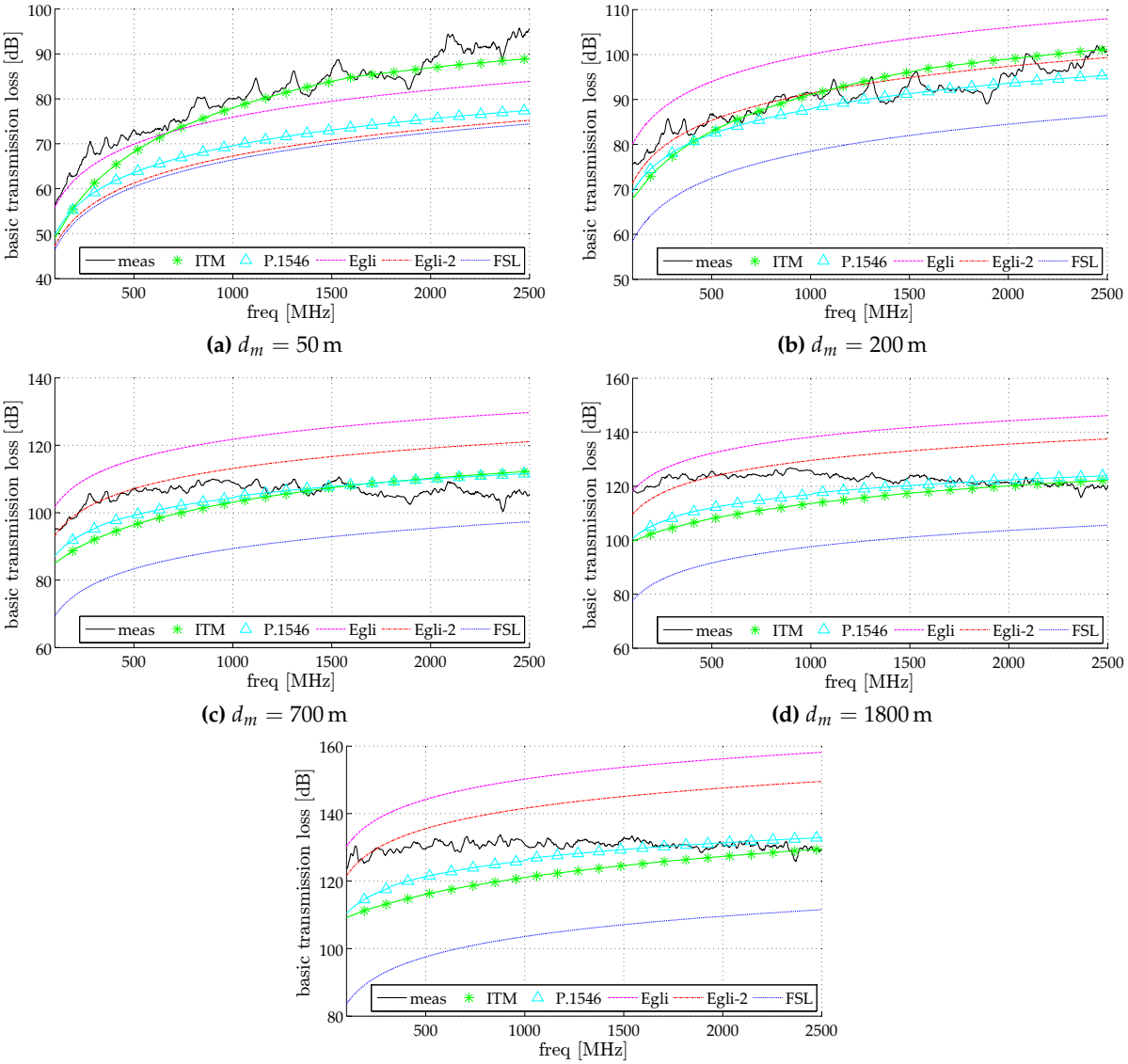

(a) $d_m = 50\,\text{m}$ **(b)** $d_m = 200\,\text{m}$

(c) $d_m = 700\,\text{m}$ **(d)** $d_m = 1800\,\text{m}$

(e) $d_m = 3600\,\text{m}$

Figure 3.6: Basic transmission loss, L_b, for dataset-1: $h_t = 5\,\text{m}$, $h_r = 2\,\text{m}$

accuracy at 94.76%. Somewhat ironically though, the ITM showed the least correlation to the measurements. Thus, although ITM predictions are the least spread, they are lacking in as far as 'tracking' the data variation is concerned. It is interesting to note, however, that all the models are poorly correlated for $d \geq 700\,\text{m}$ and especially at 1800 m where there is slight anti-correlation. The 'flattening' of the measurements is related to the effect of wave reflections as explained in Section 3.1.2 (Figure 3.4). There is thus a failure on the part of the models to represent this mechanism in a certain regime.

The result of a generic prediction is said to be acceptable if the standard deviation (SD) lies within 8 dB [79]. Such a threshold value is clearly inappropriate for the Karoo environment since all the models – including FSL – have values of ς less than 8 dB. Even more astounding is the fact that the two Egli and FSL models have the same value of deviation at all path lengths. The underlying similarity in the models is made apparent: they differ only by a constant factor which is inconsequential in the calculation of ς.

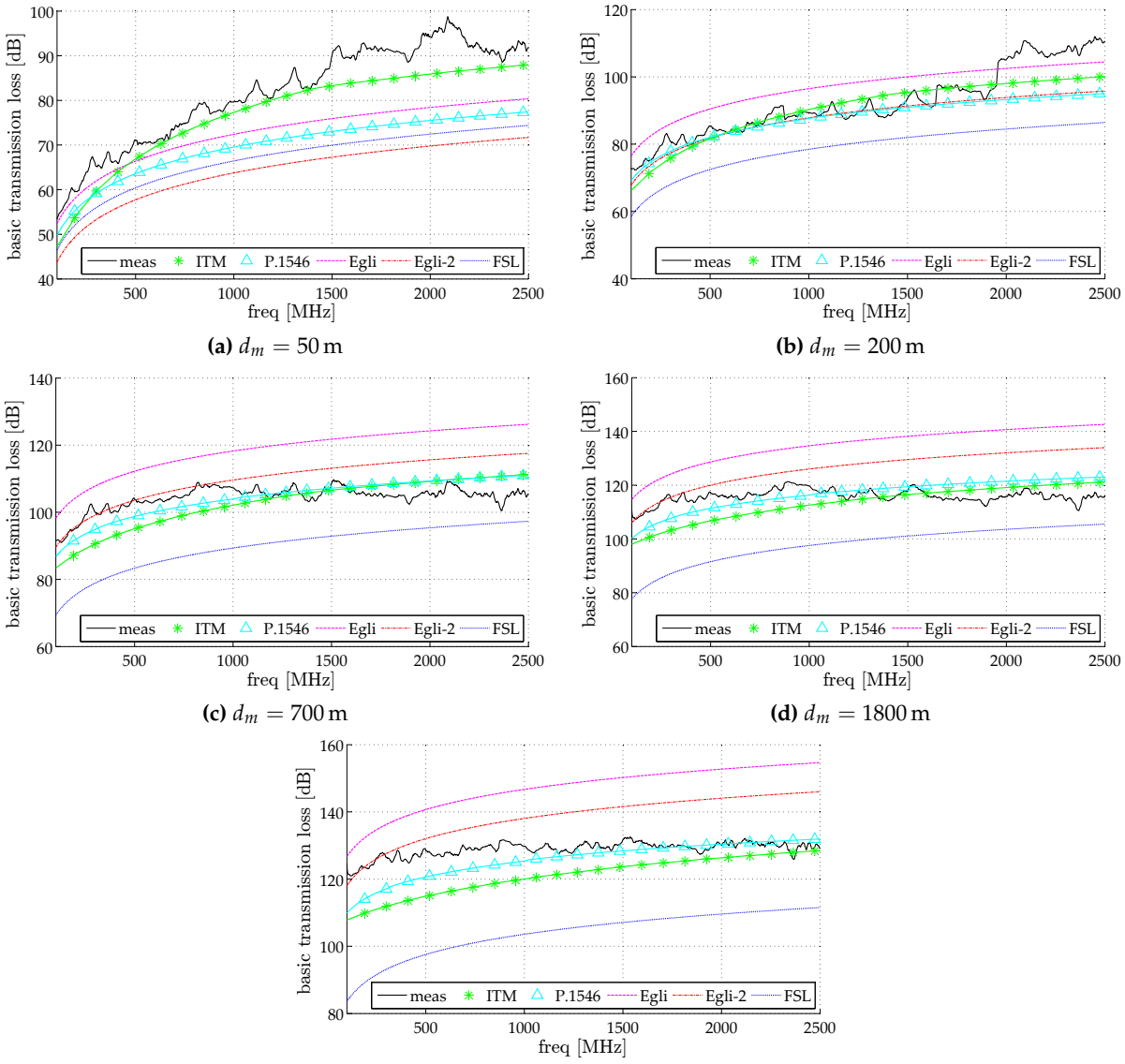

(a) $d_m = 50\,\text{m}$ **(b)** $d_m = 200\,\text{m}$

(c) $d_m = 700\,\text{m}$ **(d)** $d_m = 1800\,\text{m}$

(e) $d_m = 3600\,\text{m}$

Figure 3.7: Basic transmission loss, L_b, for dataset-2: $h_t = 7.5\,\text{m}$, $h_r = 2\,\text{m}$

Comments on Dataset 2

Error prediction analysis results on dataset-2 (DS2) are very similar to DS1. Broadly speaking, DS2 modelling is slightly more accurate since all the models show fairly strong correlation ($\rho \geq 0.72$). Comparing to DS1, there is a decrease in correlation at 200 m where ρ is 0.88 for ITM and 0.89 for the other models, versus 0.94 in DS1. The least average RMSE (across all path lengths) was 6.25 dB corresponding to the ITM which also had the least overall RE (0.05).

In spite of the improvement in linearity, RE and accuracy values were much the same. P.1546 achieved 0.04 for $d \geq 700\,\text{m}$ and thus possessed a higher degree of accuracy ($\sim$96%) at these ranges. Overall relative errors for Egli and Egli-2 were respectively 0.12 and 0.10 – two times outside the ≤ 0.05 threshold.

Table 3.2: Error statistics for DS1: $h_t = 5\,\text{m}$, $h_r = 2\,\text{m}$

d_m	mean prediction error, $\bar{\varepsilon}$ [dB]					standard dev., ς [dB]					RMSE [dB]				
[m]	ITM	P.1546	Egli	Egli-2	FSL	ITM	P.1546	Egli	Egli-2	FSL	ITM	P.1546	Egli	Egli-2	FSL
50	3.10	11.17	4.81	13.45	14.29	2.71	2.96	2.92	2.92	2.92	3.83	11.56	5.62	13.77	14.59
200	3.13	2.70	9.72	2.04	11.81	3.74	2.15	2.34	2.34	2.34	3.88	3.19	9.99	2.57	12.04
700	5.79	4.59	16.26	7.84	16.15	6.34	5.10	5.75	5.75	5.75	6.64	5.19	17.25	9.54	17.14
1800	8.36	6.32	16.32	8.99	24.38	6.98	6.45	7.39	7.39	7.39	10.42	8.07	17.84	10.59	25.47
3600	8.23	4.82	20.25	11.88	26.38	5.28	5.11	6.24	6.24	6.24	9.71	6.29	21.19	13.18	27.11
mean	5.72	5.92	13.47	8.84	18.60	5.01	4.36	4.93	4.93	4.93	6.90	6.86	14.38	9.93	19.27
	relative error					accuracy [%]					correlation coefficient				
50	0.04	0.14	0.06	0.16	0.17	95.98	86.41	94.34	83.55	82.50	0.97	0.97	0.97	0.97	0.97
200	0.04	0.03	0.11	0.02	0.13	96.48	97.00	89.28	97.73	86.88	0.94	0.94	0.94	0.94	0.94
700	0.06	0.04	0.15	0.07	0.15	94.49	95.63	84.66	92.60	84.72	0.47	0.51	0.52	0.52	0.52
1800	0.07	0.05	0.13	0.07	0.20	93.20	94.85	86.61	92.60	80.12	-0.30	-0.22	-0.21	-0.21	-0.21
3600	0.06	0.04	0.16	0.09	0.20	93.68	96.29	84.47	90.89	79.75	0.30	0.39	0.40	0.40	0.40
mean	0.05	0.06	0.12	0.09	0.17	94.76	94.04	87.87	91.47	82.80	0.47	0.52	0.53	0.53	0.53

Table 3.3: Error statistics for DS2: $h_t = 7.5\,\text{m}$, $h_r = 2\,\text{m}$

d_m	mean prediction error [dB]					standard dev., ς [dB]					RMSE [dB]				
[m]	ITM	P.1546	Egli	Egli-2	FSL	ITM	P.1546	Egli	Egli-2	FSL	ITM	P.1546	Egli	Egli-2	FSL
50	4.46	14.10	9.10	17.75	15.06	2.58	4.82	4.77	4.77	4.77	5.15	14.90	10.27	18.38	15.80
200	4.13	6.80	6.45	4.76	13.80	4.94	5.55	5.32	5.32	5.32	5.32	8.77	6.78	6.93	14.79
700	4.82	3.79	14.30	5.89	14.59	5.31	3.91	4.60	4.60	4.60	5.51	4.43	15.02	7.29	15.30
1800	5.47	4.61	19.21	10.73	17.89	5.97	5.22	6.23	6.23	6.23	6.41	5.36	20.19	12.26	18.95
3600	7.74	5.29	18.26	9.84	24.87	4.34	3.94	5.20	5.20	5.20	8.84	6.48	18.97	10.91	25.41
mean	5.32	6.92	13.46	9.79	17.24	4.63	4.69	5.22	5.22	5.22	6.25	7.99	14.25	11.15	18.05
	relative error					accuracy [%]					correlation coefficient				
50	0.05	0.17	0.11	0.21	0.18	94.55	83.27	89.48	78.71	82.05	0.97	0.97	0.97	0.97	0.97
200	0.04	0.07	0.07	0.05	0.15	95.70	93.10	92.87	95.27	85.40	0.88	0.89	0.89	0.89	0.89
700	0.05	0.04	0.14	0.06	0.14	95.33	96.34	86.34	94.39	85.95	0.73	0.76	0.76	0.76	0.76
1800	0.05	0.04	0.17	0.09	0.15	95.26	96.01	83.42	90.73	84.55	0.30	0.36	0.36	0.36	0.36
3600	0.06	0.04	0.14	0.08	0.19	93.96	95.87	85.87	92.39	80.65	0.73	0.77	0.78	0.78	0.78
mean	0.05	0.07	0.12	0.10	0.16	94.96	92.92	87.60	90.30	83.72	0.72	0.75	0.75	0.75	0.75

3.3.3 Discussion of Results

It is clear that even in 'simple', short range scenarios basic transmission loss does not trivially reduce to free space loss as it is sometimes suggested. However, in context of the SKA, using the FSL predictions can be regarded as a conservative benchmark, because predicted transmission losses are typically lower than actual transmission losses. The limiting factor in such an approach is it could lead to an over-design in terms of the required shielding of RFI-generating equipment.

Performance evaluation via statistical metrics has ascertained the validity of ITM and P.1546 models for basic transmission loss predictions in the Karoo. Although evaluations of these models have been performed already [81, 87–89], to the best of our knowledge none has been undertaken for low antenna heights (< 10 m) and short range (< 1 km) in a semi-arid region. Superiority of the ITM was evident in the consistent predictions across all path lengths, yielding overall RMSE's of 6.90 dB and 6.255 dB for the two respective datasets. Mention should be made that this is not to say the ITM outperformed the other models at all path lengths. It is to state that the ITM yielded RMSE values that were well below the threshold value at all path lengths.

In both DS1 and DS2, P.1546 exhibited good performance except at 50 m where the prediction is approximately equal to spreading loss (FSL), as expected at short ranges. RMSE was 6.86 dB in DS1 and 7.99 dB in DS2.

Regarding the predictions of the Egli models, even though acceptable overall RMSE's were obtained, they are not recommended for modelling propagation in the Karoo under the specified parameter space. This is on account of the fact that they tend to overestimate the loss. If used, erroneous conclusions might be drawn. Furthermore, the standard Egli model showed a rather inconsistent performance. It only met the RMSE criteria at 50 and 200 m in both datasets.

Based on the physical configuration, the main propagation mechanism at play was reflection. Yet, evidence of cancellation and reinforcement is observed neither in the measurements nor predictions as would be expected at 50 and 200 m from theory (see Figure 3.4). For the measurements, this is most likely due to the fact that the sampling system records mean rather than peak values [90]. In respect of the models, this indicates that they are not designed to model this kind of behaviour. The 'flattening' of the transmission loss at 700 m and greater does however correlate to reflection when path length differences are small. Fading and peaking is not observed since the frequency interval is much larger than the bandwidth. In fact, this frequency-independent behaviour corresponds to regions of maxima in the received power. This would be apparent if the frequency range of theoretical predictions were extended. An alternative way to look at it is that for the measurement bandwidth, the breakpoint, d_b, is encountered such that the received power follows the plane earth model. However, this should not apply to frequencies greater than 1671 MHz at 700 m. That is, 700 m is the break distance for 1671 MHz, whereas at the highest frequency (2500 MHz) $d_b = 1047.2$ m.

3.4 The Question of Measurement Uncertainty

Assuming negligible systematic error, quantifying the uncertainty in the measurements would require multiple recordings for each physical configuration. This, however, could not be done due to time and logistical constraints. Instead, a reference measurement involving a direct LOS path was obtained at 10 m. By applying the FSL model, a comparison was made between this reading and the direct signal of the generator as measured on the RTA. A good match was obtained, providing confidence in the setup.

Since the measurements were not particularly extensive and the error is unknown, the analysis presented must be regarded as a reference point for future propagation studies.

3.5 Summary

Mechanisms of relevance to signal propagation in the Karoo have been considered in greater detail with emphasis on reflection. Against this backdrop, ITM, ITU-R P.1546 and Egli models were evaluated against measured results to assess their suitability for modelling in the Karoo. We have shown that P.1546 and ITM models are valid for path loss predictions in the MeerKAT environment at ranges greater and less than 1 km. The main metric of this assessment was the root mean square error (RMSE). The suitability of these two models further lies in the fact that their mean prediction errors are always positive*, indicating that they predict a higher received power (lower loss). This is ideal as overestimating the loss would be very problematic for the SKA. In other words, a good (low RMSE) but conservative (positive $\bar{\varepsilon}$) prediction is preferred.

Since reflections reduce loss, it is very important that this effect is modelled with accuracy. Though ITM and P.1546 satisfy the performance criteria, they evidently lack the capacity to represent even basic reflection. ITM predictions could of course be improved by using terrain data, but it is sufficient to herald its suitability for generic predictions. This is because precise modelling of the MeeerKAT environment must incorporate scattering effects in the vicinity of receptors – something that no amount of fine-tuning can achieve for any empirical or semi-empirical model. We now shift the discussion towards deterministic modelling involving full-wave and physical optics techniques in order to capture complex reflection (scattering) phenomena.

*This is with respect to the prediction error definition, $\varepsilon = PL_{\text{meas},i} - PL_{m,i}$

Chapter 4

Deterministic Modelling: Development and Verification

Undoubtedly, propagation models derived from a solution of Maxwell's equations yield very accurate predictions. Full wave techniques are those that do not involve *a priori* physical approximations in the numerical evaluation of some wave equation, while asymptotic methods are based on approximations in the high frequency limit. By their nature, full-wave and asymptotic techniques tend to be computationally taxing even for what may be regarded as basic scenarios. As such, empirical models are favoured over these numeric methods. Yet, the limitations of empirical path loss modelling were apparent in Chapter 3: failure to accurately model real ground, inability to incorporate scattering phenomena and inadequacy in representing underlying physical processes. Hence, to meet the accuracy demands of the SKA-SA pertaining to characterising the complex environment of MeerKAT, a numeric model becomes a compelling solution. Utilising FEKO, a hybrid model involving full-wave and ray-tracing techniques has been conceived. Verification of the model is performed by comparison to measurements at the KAT-7 array.

4.1 Overview of FEKO

FEKO[*] is a commercial computational electromagnetics (CEM) code based on the method of moments (MoM). It is a comprehensive software package capable of both full-wave and (high frequency) asymptotic analyses/solutions [92]. Full-wave methods involve exact numerical solutions to Maxwell's equations while asymptotic techniques make use of approximations to evaluate Maxwell's equations in the high frequency limit. To cater to a host of electromagnetic (EM) problems of varying electrical size and material properties, FEKO is equipped with a variety of solvers whose details are explained in the FEKO User Manual [91]. Of particular interest here is the MoM, large element physical optics (LE-PO), uniform theory of diffraction (UTD) and ray launching geometrical optics (RL-GO).

4.1.1 FEKO Solvers

In general, MoM, finite element method (FEM) and finite difference time domain (FDTD) are ideal for geometrically complex problems while the multilevel fast multipole method (MLFMM), physical optics (PO), and UTD methods are best suited to problems of large electrical size. Hybridisation of the MoM/MLFMM with FEM or MoM with ray methods can be implemented as dictated by the regions/parts contained in a model (e.g. a parabolic reflector can be solved with PO while the feed is treated with the MoM).

[*] *FEKO* is an acronym for the phrase ***FE****ldberechnung bei* ***K****örpern mit beliebiger* ***O****berfläche* which is translated, *"Field computations of arbitrary shape."* [91]

4.1.1.1 Method of Moments

The method of moments (MoM) is a well known and widely used frequency domain, full-wave method. It forms the default and core aspect of the FEKO solver. Being ideal for radiation and scattering problems, the MoM is widely used in antenna engineering.
MoM formulation utilises an appropriate Green's function to derive an integro-differential form of Maxwell's equations. To reduce the number of unknowns and make the problem tractable computationally, a suitable boundary condition and basis functions must be selected. This results in a system of linear equations of the form [69, 70],

$$V_m = \sum_{n=1}^{N} Z_{mn} I_n, \qquad m = 1, 2, ..., N \tag{4.1}$$

where Z_{mn} is called the system matrix, V_m is the source vector and I_n is the unknown vector (typically surface current) that is solved for using lower and upper triangular matrix factors (LU-factorization) of the system matrix. Subscript m represents sampling points while n refers to source points. Basis functions supported in FEKO are triangular rooftop Rao-Wilton-Glisson (RWG) functions and higher order basis functions (HOBF). A larger mesh is made possible by HOBF's and this reduces the memory requirements for electrically larger problems [93].
As can be seen from (4.1), a MoM solution resolves the fields due to a radiator/scatterer by computing equivalent surface currents represented by I_n [70]. A major advantage of this solution is that discretisation is limited to the object(s) of interest (source method) rather than the surrounding free space as well. Predominant application of the MoM is to metallic structures. However, implementation in the FEKO includes extensions that enable the modelling of dielectrics. Of special interest here is the Sommerfeld formulation and reflection coefficient approximation (RCA) that are used to simulate 'real ground' via an infinite dielectric plane [91, 93].

4.1.1.2 Large Element Physical Optics

Physical optics is an asymptotic numerical method whereby the scattered field is computed from the induced surface current density, $\mathbf{J}_s = 2\hat{\boldsymbol{n}} \times \mathbf{H}^{\text{inc}}$, in the illuminated region and taken as zero in the shadowed zone [69, 94]. Assumptions here are that the scatterer is perfectly conducting and large compared to wavelength. To overcome limitations in resolving diffracted fields, PO implementation in FEKO includes correction factors for currents near edges and wedges [95]. By virtue of its formulation the PO solver is ideal for regions of larger electrical size than can be modelled comfortably with the MoM or MLFMM. Extension is also provided to support modelling of dielectrics.

Large element physical optics (LE-PO) is a slightly different formulation of the PO solver that permits a larger mesh ($9\lambda/5$ compared to $\lambda/8$ for PO [91]). Consequently, it can handle electrically larger structures provided they are 'smooth' and the incident field is continuous.

4.1.1.3 Ray Launching Geometrical Optics

Geometrical optics (GO) assumes electromagnetic (EM) waves travel in straight line paths called rays. GO considers an interface to be of infinite extent and furthermore presumes planar reflected and refracted (transmitted) waves. Fresnel reflection and transmission coefficients are used to determine the amplitudes of the resultant fields [94, 96].
In FEKO, GO is applied using a technique known as ray launching (RL) or shooting and bouncing rays (SBR). Hence, the solver is referred to as ray launching geometrical optics (RL-GO). It is ideal for modelling very large ($> 20\lambda$) dielectric and metallic structures [91]. Hybridisation with the MoM is supported but may prove computationally taxing if the MoM region is very detailed since rays are launched from every radiating element. Nonetheless, because a coarse mesh is employed for the RL-GO region (assuming a 'smooth' surface), it is an effective method for modelling thin dielectric sheets (TDS) and dielectric-coated metallics [97].

4.1.1.4 Uniform Theory of Diffraction

The geometrical theory of diffraction (GTD) extends GO to incorporate the effect of diffraction and thereby predict the field in the shadow zone. There exists, however, a discontinuity at the boundary between the illuminated and shadowed regions. This limitation of the GTD is addressed by the uniform (geometrical) theory of diffraction (UTD) which ensures continuity of the field across all regions [98, 99].
The UTD solver is an expedient asymptotic solution for electrically extremely large regions since the memory requirements are independent of frequency [100]. Surface reflections and edge/corner diffractions are computed without the need for meshing the UTD region. However, problems that can be solved with UTD are limited to those resembling canonical form [101].

4.1.2 Interfacing with FEKO

FEKO models are built via computer-aided design (CAD) using a graphical user interface (GUI) called *CADFEKO*. By default, material properties of objects are set as perfect electrical conductor (PEC) with the surrounding medium as free space. As a matter of fact, the material properties of a wire or thin sheet cannot be changed unless a coating or layer is applied to it. However, the material properties of a region defined by a closed volume (e.g. cuboid or cylinder) can be changed and the faces will correspond to the interior [91]. Once construction of geometry is complete, physical and electrical connections are made by a union operation. At least one source must be added to the model and this is applied to a port that must be defined by the user. After the frequency has been selected the model can then be meshed, the general guideline being a step size of $\lambda/10$, with λ corresponding to the highest frequency. Possible solution requests include near- and far-fields, currents and scattering parameters (S-Parameters), which may be exported each to their own ASCII[†] text file for analysis in another program.
Results can be viewed and further processed in another GUI, *POSTFEKO*. Information such as received power that lacks a save-to-file option within the CADFEKO environment can be

[†]American Standard Code for Information Interchange

exported as text data from POSTFEKO. Additional or customized information can be added to a model using the special text editor, EDITFEKO. This is done by editing/adding 'cards' in the automatically generated `*.pre` files which contain the geometry and solution request details. Detailed specifics on the solvers and their applications can be found in the FEKO User Manual [91] and online documentation [93, 95, 97, 100].

4.2 Deterministic Propagation Modelling with FEKO

FEKO has been used with great success in the design and analysis of antennas [102–105] and investigations on radiation, coupling and shielding to address electromagnetic compatibility (EMC) [9, 11, 106]. In terms of modelling a full scale propagation environment using FEKO, Pienaar [11] achieved this with respect to diffraction and shielding effectiveness characterisation of the (artificial) soil berm at the SKA-SA site, while Kuja [106] confirmed the inherent embedding of path loss data in scattering (S) parameters using dipoles in free space and over a PEC ground – the focus of this work being investigating MeerKAT dish-to-dish coupling. In view of the above, we recognised the capabilities and potential of utilising FEKO for propagation modelling. We have explored and achieved a deterministic model that accurately reproduces a deployment scenario by modelling antenna characteristics, scattering objects and real ground. Additionally, capacity to model topography is demonstrated. To the best of our knowledge the work here is the first of its kind to exploit the existing MoM-based code FEKO to generate numeric data for path loss predictions.

4.2.1 Full Wave Propagation Modelling

Using the default MoM solver in FEKO, a full-wave propagation model (FWPM) was achieved. This involved modelling transmit and receive antennas in the presence of real ground via an infinite dielectric ground plane. This approach is advantageous since the infinite plane does not need to be discretised (meshed). Three types of ground were modelled as per the relative permittivity and conductivity data corresponding to wet, medium dry and very dry grounds extracted from the curves in ITU-R P.527 [39].
Given an S-parameter request, the simulated path loss, L_{bs}, is computed as

$$L_{bs} = -20 \log \left| S'_{21} \right| + 2G \,, \tag{4.2}$$

where for identical antennas G (dBi) is the gain of the transceivers as extracted from the far-field (`*.ffe`) file, and the mismatch-corrected transmission coefficient is

$$\left| S'_{21} \right| = \frac{|S_{21}|}{\sqrt{(1 - |S_{11}|^2)(1 - |S_{22}|^2)}} \,,$$

with S_{11} and S_{22} being the respective reflection coefficients at the ports of the transmit and receive antennas.
Another approach is to place a matched load at the port of the receiving antenna. Received power can be obtained from POSTFEKO via the power dissipated in the load. With the input

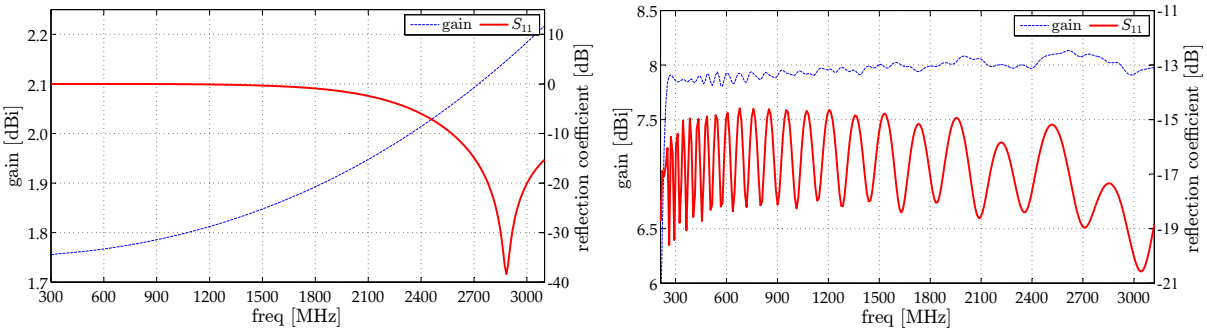

(a) half-wave dipole characteristics

(b) LPDA characteristics

Figure 4.1: Gain (dBi) and reflection coefficient (S_{11}, dB) of antennas used for FWPM simulations. In spite of poor matching, the dipole bandwidth can be extended to any desired range. At the lowest frequency the configuration is that of a short dipole as evidenced by the gain of 1.76 dBi. The LPDA is shows a good S_{11} response of less than −14 dB across the band.

power scaled to 1 W such that there is no mismatch loss at the transmitter, the simulated path loss is simply

$$L_{bs} = -10\log\left(p_r'\right) + 2G\,, \tag{4.3}$$

where $p_r' = p_r/(1-|S_{22}|^2)$ is the received power (W) corrected for mismatch.

4.2.1.1 Antenna Modelling

Two types of antenna were used during simulation: half-wavelength ($\lambda/2$) dipoles and log-periodic dipole arrays (LPDAs). The design of a wire dipole is straightforward, the length being set to $0.5 \times c/f_{\max}$, where c is the speed of light in a vacuum as before. An input impedance of 73 Ω was loaded at the ports as per the radiation resistance of thin $\lambda/2$ antennas [27]. It is clear from the S_{11} in Figure 4.1a that the dipole was poorly matched across most of the band. Yet, this did not compromise the quality of the data generated since mismatch corrections were made during analysis.

Antenna Magus was used to design an LPDA with a bandwidth of 175 % centred at 1664 MHz. Thus the frequency range extended from 208 to 3120 MHz and averaged a gain of ∼8 dB. Parametrized by a spacing factor of 0.131, the LPDA consisted of 33 elements. Load and input impedances were 292.19 Ω and 200 Ω, respectively. As shown in Figure 4.1b, the LPDA was well-matched with an S_{11} response of less than −14 dB over the entire band.

4.2.1.2 Real Ground Modelling

A significant part of predicting propagation losses relates to modelling both the variation of the ground (terrain) and its electrical properties (complex permittivity). The latter can be achieved easily in FEKO via the reflection coefficient approximation (RCA) or exact Sommerfeld integrals. In both cases an infinite ground plane (homogeneous half-space) is modelled based on the electrical soil parameters of a user-defined dielectric. Sommerfeld integrals are the general solution to the problem of radiation above an imperfectly conducting surface. Norton recast Sommerfeld's formulation into a simpler, more applicable form from which the RCA is obtained [40, 107]. With respect to implementation in FEKO, surface waves are computed in the

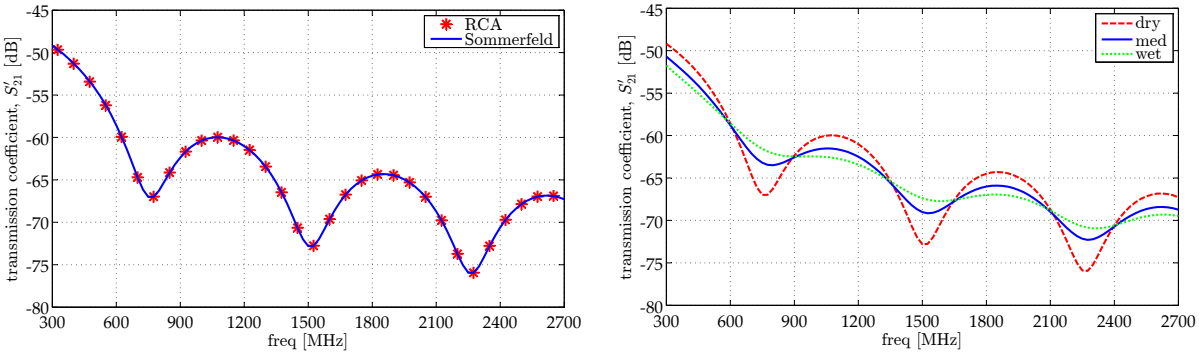

(a) comparison of real ground methods

(b) comparison of different grounds using RCA

Figure 4.2: Mismatch-corrected transmission coefficient (S'_{21}) as a function of frequency over real ground with $d_m = 50\,\text{m}$. As can be seen in (a), the RCA coincides very well with the Sommerfeld formulation. The comparison of different grounds in (b) reveals that nulls due to cancellation are more pronounced for very dry ground. Conversely, the received field over very dry ground is 1 to 2 dB higher than medium and wet grounds at maximum reinforcement.

Sommerfeld formulation while the RCA only accounts for the space wave (direct and ground-reflected waves). Since surface wave contributions are negligible in the propagation scenarios of interest, the RCA will be used, having with it the advantage of faster computations than the Sommerfeld formulation. For instance, it took 15.31 h on 12 cores (78 MB per core) to obtain the Sommerfeld result in Figure 4.2a, while the corresponding RCA simulation took 40.165 s on 3 cores (218.65 kB per core).

As stated earlier, the complex permittivity used in this study was based on relative permittivity (ϵ_r) and conductivity (σ) curves corresponding to wet, medium dry and very dry grounds as provided in ITU-R P.527. With the conductivity expressed by the loss term $x = \sigma/\omega\epsilon_0$, these data are presented in Figure 2.4. Although it is observed that the frequency dependence of the dielectric constants of especially medium dry and very dry grounds are small (respective differences of 0.14 and 0.09 between maximum and minimum values), it is a matter of prudence to use the recommended values in their entirety.

Corrected transmission coefficients (S'_{21}) obtained over the three types of ground are shown in Figure 4.2b. In view of the slight differences, the best-fit must be sought from predictions involving all three grounds since in general the ground constants are not known. Comparison via S'_{21} of the modelling methods in Figure 4.2a shows that the RCA is indeed a very accurate approximation of the fields obtained over a real ground.

4.2.2 Ray-based Modelling

Full scale representation of terrain irregularities and obstacles such as hills becomes challenging to solve with the MoM due to the high memory requirements associated with modelling dielectrics. It is here that asymptotic methods become particularly appealing since they utilize much coarser mesh sizes. Careful implementation can yield very accurate mock-ups of a given radio environment.

4.2.2.1 Equivalent Sources and Ideal Receivers

Hybridisation of the MoM with asymptotic methods can result in long solution times due to the fact that illumination must be determined from each current element in the case of PO, while ray contributions must be traced from each radiating element for GO. Computational resources can therefore be minimised by replacing antennas with equivalent sources and ideal receivers. A key advantage of this approach is that perfect matching is assumed and hence no correction for mismatch is required during analysis. The method relies on some antenna (spherical mode expansion coefficients, near- or far-field) data obtained under free space conditions and subsequently imported into a given model [91].
As dictated by the problems of interest, here equivalent sources and ideal receivers were modelled using far-field data. This approximation allows for the transmitter to be represented as a point-source while the ideal receiver is reciprocal to it [91]. To illustrate the concept, Figure 4.3 shows a comparison of the power received, gain and basic transmission loss obtained for $\lambda/2$ a dipole and its point-source/ideal receiver representation. Transmit and receive dipoles were simulated in the presence of real ground separated by 200 m. This setup was repeated for an equivalent source and ideal receiver as depicted in Figure 4.3a. In both cases, the transmitted power was scaled to 1 W (no mismatch). Maximum deviations of 0.92 dB and 0.46 dBi were observed for the power and gain respectively. Evidently, the equivalent source is a slightly different antenna than the one on which it is modelled. One possible explanation is that the point source approximation by definition does not incorporate near-field effects while these are present for the actual dipoles above a ground plane. However, in terms of basic transmission loss there is no difference since antenna characteristics are removed from the computation as can be seen in Figure 4.3d.

Further simplification of a model can be made by eliminating the receiving antenna altogether. This can be done by requesting the electric field at any desired location(s) via a near-field request. With the source power scaled to 1 W (no mismatch) as before, basic transmission loss is then

$$L_{bs} = 2G - 20\log(E) + 20\log(f) \begin{cases} -12.79 & \text{for } E \text{ in dBV/m} \\ +107.2 & \text{for } E \text{ in dB}\mu\text{V/m} \end{cases}. \tag{4.4}$$

By requesting the electric field in a phi-cut ($\theta = 90°$) centered about a source, a path loss map such as in Figure 4.6b can be generated using (4.4).

4.2.2.2 Finite Ground Planes

Finite ground planes are difficult to implement for propagation studies yet may be needed for a solution involving RL-GO or UTD which currently support neither infinite nor real grounds. A basic finite ground plane can be achieved using a PEC surface created by the rectangle dialogue. However, this is limiting since the face properties cannot be changed. Alternatively, a slab can be constructed (using either the cuboid dialogue or applying a 'sweep' operation to a rectangular surface) whose region properties can then be set to the desired dielectric. Regrettably, this is problematic to solve. A solution is possible with RL-GO but accuracy is not

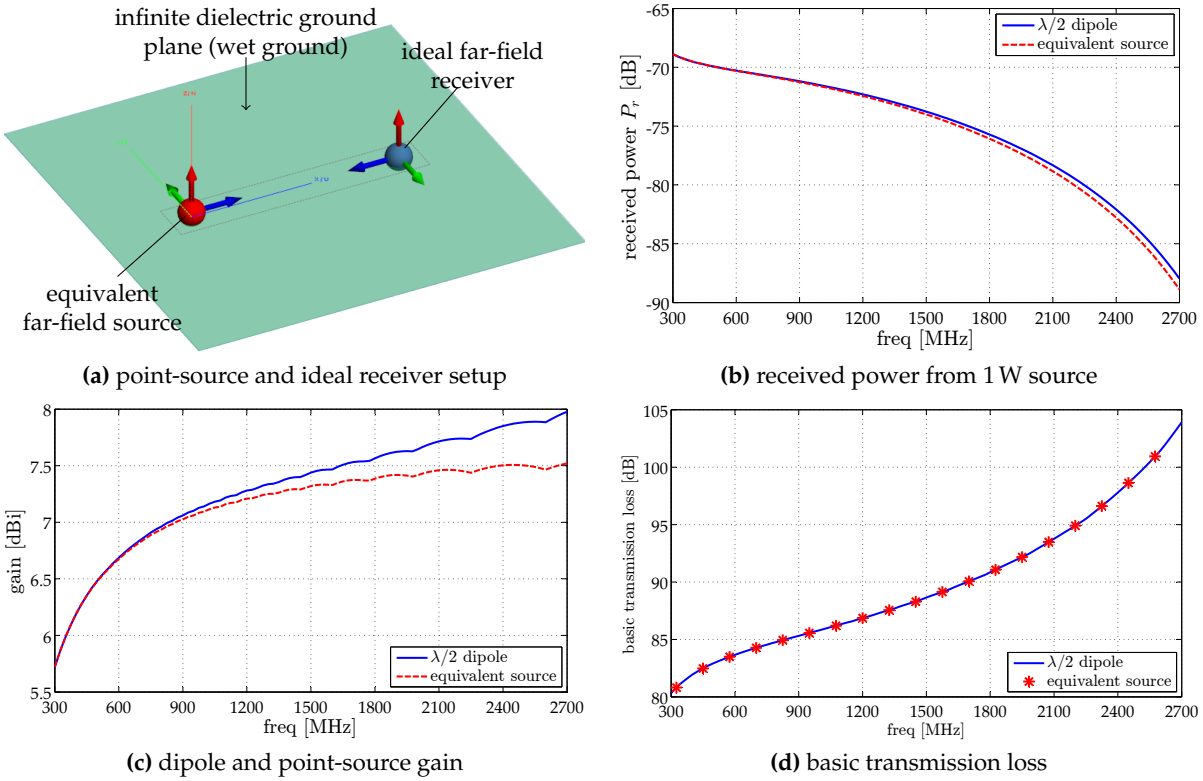

(a) point-source and ideal receiver setup

(b) received power from 1 W source

(c) dipole and point-source gain

(d) basic transmission loss

Figure 4.3: Numerical path loss modelling using an equivalent source and ideal receiver based on $\lambda/2$ dipole far-field data. The setup is shown in (a), the path length being 200 m with $h_t = 5$ m and $h_r = 2$ m. Power received by both dipole and ideal receiver is plotted in (b) while the corresponding gains are represented by the curves in (c). As can be seen in (d), the equivalent source and ideal receiver approximations yield the same value of basic transmission loss as the full dipole simulation.

guaranteed. Furthermore, it is computationally expensive and rather slow requiring at least 2 h for a ground plane only solution for 51 frequency points. Adding layers of complexity in the form of obstructions would only aggravate the situation further.

The simpler and faster approach conceived in this work was to coat a PEC sheet with a dielectric (corresponding to the aforementioned types of ground) and solve this with the UTD. Thickness of the layer is key to obtaining correct results since the solution relies on the thin dielectric sheet (TDS) approximation. Consequently, this method works best for single frequency setups rather than frequency sweeps. Initially a thickness of $\lambda/10$ was applied but on further examination we found that a thickness of $\lambda/2$ was optimal, yielding results coinciding very well with the FWPM (RCA) result as shown in Figure 4.4.

Implementation of this method requires a separate simulation of the source over real ground (corresponding to the layer applied to realise the finite ground) in order to obtain the correct antenna gain. Received electric field or power obtained over the finite ground otherwise coincide with the corresponding values over real ground.

4.2.2.3 The KAT-7 Mock-Up

A key area of interest for the SKA-SA is prediction and analysis of interference within the MeerKAT core. As a starting point to develop a deterministic model capable of simulating the

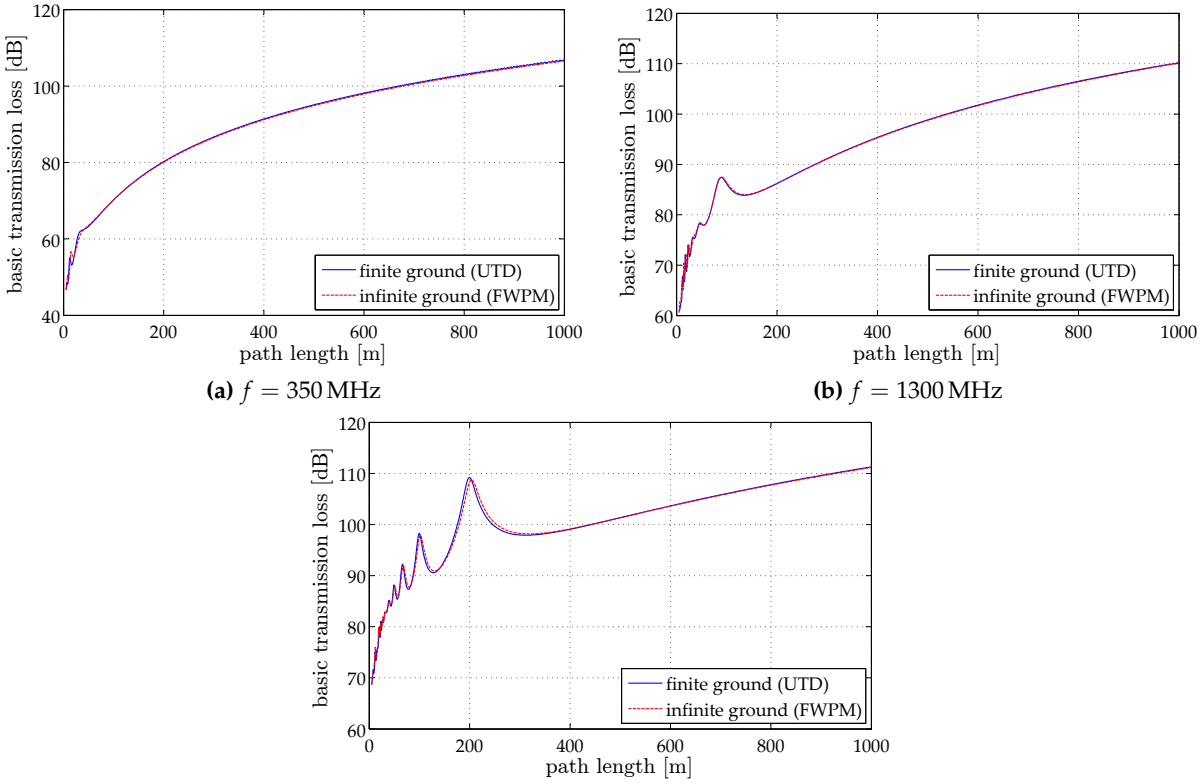

(a) $f = 350\,\text{MHz}$ **(b)** $f = 1300\,\text{MHz}$

(c) $f = 3050\,\text{MHz}$

Figure 4.4: Comparison of basic transmission loss over infinite and finite ground planes. The finite ground plane is a PEC surface coated with a dielectric layer (wet ground in this case) and solved using UTD while the infinite plane is real (wet) ground modelled using the RCA. For all three cases, $h_t = 5\,\text{m}$ and $h_r = 2\,\text{m}$.

full scale MeerKAT receptors*, we first developed a mock-up of the KAT-7 array with fewer dishes and a much smaller area. We took the detailed $1/20^{\text{th}}$ computational scale model of a KAT-7 receptor developed by Wiid *et al.* for RFI and lightning protection studies [9, 109] and scaled it up to full size: a combined pedestal and yoke height of 6 m and a dish diameter of 12 m. To avoid geometry errors due to the many faces and edges, the receptor model was converted to a 'primitive' part†. Using the positioning data available on the SKA-SA public science/engineering site [110], a mock-up of the KAT-7 array to full scale was realised as shown in Figure 4.5, all receptor surfaces being set to PEC. Because it is not permitted for objects to rest on a real ground, the receptors were raised to a height of $\lambda/10$.

Taking computational requirements and geometrical considerations (multiple faces and curved surfaces) into account, the receptors were solved using large element physical optics (LE-PO). Evolution of path loss in the vicinity of the array was investigated using two complementary setups. The first involved a frequency sweep from 350 to 3100 MHz at a T-R separation of 150 m with the line-of-sight (LOS) path going through the centre of the array (as illustrated in Figure 4.5). In the second setup, the source was placed at the centre of the array and trans-

*Within SKA-SA circles, "a receptor is the complete antenna structure, with the main reflector, sub-reflector and all receivers, digitisers and other electronics installed [108]." Here, *receptor* refers to the complete but simplified dish structure without the electronics

†This is a FEKO operation that simplifies a complex model by representing it as a single part rather than several faces

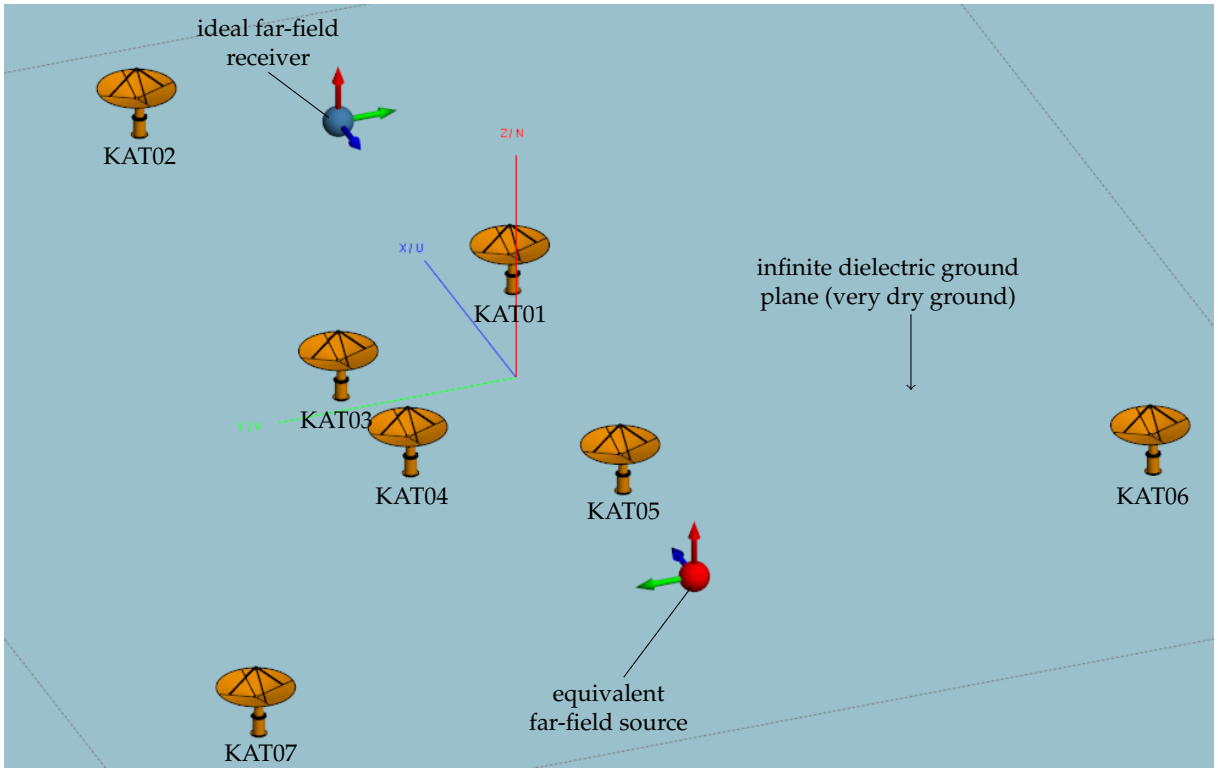

Figure 4.5: Full scale computational model of the KAT-7 array with the dishes in the stowed position.

mission was only at one frequency in order to compute the loss as a function of path length outward from the centre. For both configurations, the transmitting and receiving heights were 5 m and the ground plane properties were set to very dry.
Figure 4.6a reveals that the reference attenuation (basic transmission loss relative to free space) changes quite dramatically due to the presence of the receptors. While the reference attenuation, A_{ref}, is on average around 11 dB for the regular half-space, it reduces to as little as 2.8 dB at 1354 MHz. Similarly, the alternative picture provided by the path loss map in Figure 4.6b demonstrates very clearly that the KAT-7 array is a complex multipath environment where the loss will not follow the typical trend. Regions of high loss are not of concern – it is the regions and frequencies of decreased loss that could be problematic. Invaluable information can be obtained by way of this type of modelling, the validation of which is addressed in Section 4.5.

4.3 Model Verification by Theory

4.3.1 Assessment via the Friis Transmission Equation

The power received by an antenna in free space was given by (2.18) as

$$P_r = \text{EIRP} + G_r - L_{bf}\,, \tag{4.5}$$

where it is recalled $\text{EIRP} = P_t + G_t$. Equation (4.5) is the well known Friis transmission formula [111] which provides a theoretical relation between transmitted and received power under the presumption of matched antennas with respect to load (reflection) and polarization.

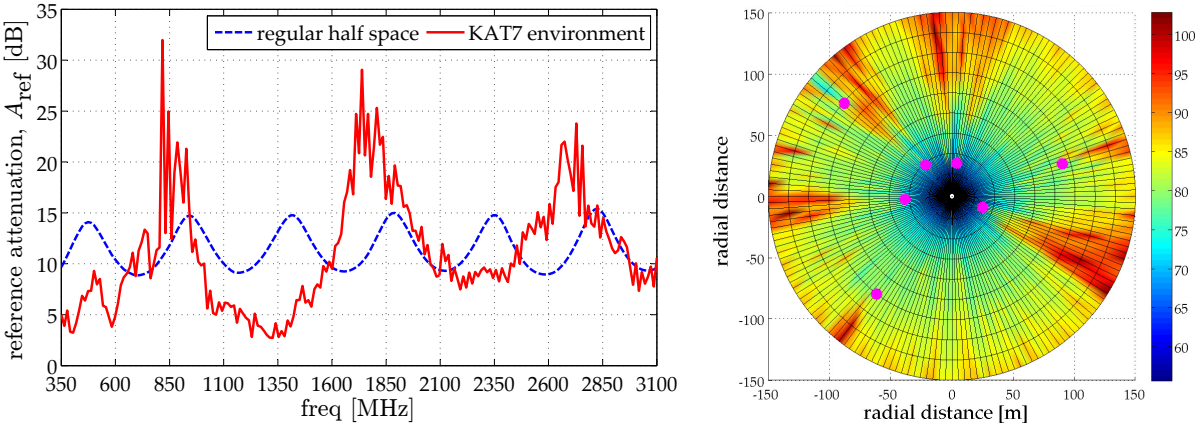

(a) reference attenuation at 150 m

(b) path loss map for 350 MHz

Figure 4.6: Evolution of basic transmission loss in the vicinity of KAT-7. The magenta dots in (b) represent the receptor locations.

Rearranging (4.5) in terms of free space basic transmission loss gives

$$L_{bf} = \text{EIRP} + G_r - P_r\,, \tag{4.6}$$

which is equivalently given by (2.45):

$$L_{bf} = 20\log(f) + 20\log(d) + 32.45\,, \tag{4.7}$$

where f is in MHz and d is in km. Hence, validity of the full-wave propagation model (FWPM) introduced in Section 4.2.1 can be determined by comparing the prediction offered by (4.6) to the theoretical loss given by (4.7). That is, in free space, the prediction of (4.2) should yield the result predicted by (4.7).

As can be seen in Figure 4.7, the FWPM result is in agreement with the theoretical formulation of the free space loss term in the Friis transmission equation. This is of course the expected result since a full-wave solution encapsulates the physics of propagation.

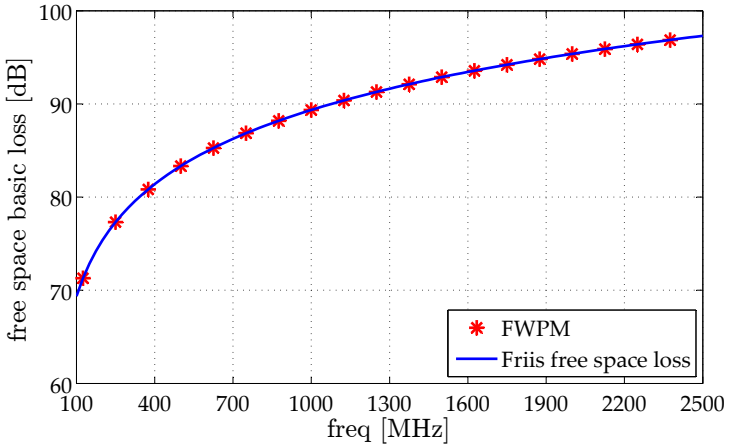

Figure 4.7: Free space path loss predictions at a path length of 700 m

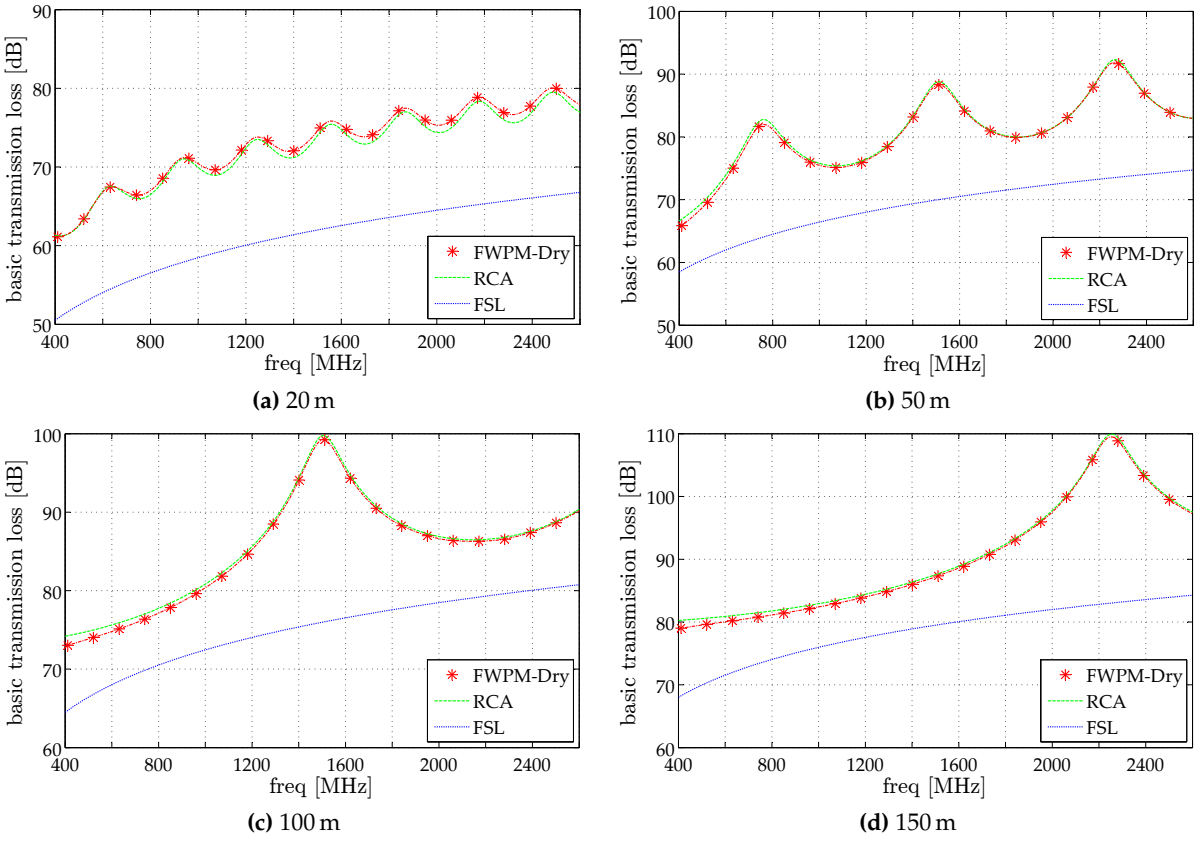

Figure 4.8: Basic transmission loss over very dry ground (reflection coefficient approximation).

4.3.2 Comparison to the Analytic RCA Solution

Verification of the reflection coefficient approximation (RCA) solution of the FWPM was performed by an equivalence check to the Sommerfeld formulation (see Figure 4.2a). To further ascertain the validity of the FWPM prediction, a comparison was made to the analytic expression of the RCA in terms of basic transmission loss, namely,

$$L_b^{\mathrm{RCA}} = 20\log\left(\frac{4\pi f d_m}{c}\frac{h_{gt}+h_{gr}}{|1+R_v\exp(-j\Delta\phi)|}\right), \tag{4.8}$$

where $|1+R_v\exp(-j\Delta\phi)|$ is the magnitude of the electric field due to direct and reflected waves relative to free space and $\Delta\phi = k\Delta d$ is the phase difference arising due to the path length difference Δd as before. The terms h_{gt} and h_{gr} are 'height gain' geometric factors due to the half-space configuration and given for vertical polarization by [112]

$$h_{gt,gr} = \left|\frac{d_m^2 r}{R_1^3}e^{-jkR_1} + \frac{d_m^2 r}{R_2^3}e^{-jkR_2}\right|_{\max} \begin{cases} r = \sqrt{d_m^2+h_t^2} & \text{for } h_{gt} \\ r = \sqrt{d_m^2+h_r^2} & \text{for } h_{gr} \end{cases} \tag{4.9}$$

where R_1 and R_2 are the respective path lengths of the direct and reflected waves. With free space loss as a reference, Figure 4.8 shows FWPM and Matlab-implemented RCA basic transmission loss curves over very dry ground. Maximum deviations of 1.07 dB were noted between the predictions at 20 and 50 m, while differences of 1.26 dB and 1.29 dB were registered at 100

(a) (b)

Figure 4.9: Open area test site for FWPM validation measurements. An overview of the field and its surrounding is shown in (a). The measurement setup is illustrated by the picture in (b) corresponding to a 20 m path length. Under the tent in the bottom left corner is the signal generator, battery and inverter. Image credits: Gideon Wiid

and 150 m, respectively. The disparity is in all probability due to the limitation in computing the height gain factors which are representative of the change in radiation pattern and hence antenna gain due to the presence of the ground.

4.4 FWPM Verification by Measurement

It has been observed that path loss results can change quite dramatically when transmission takes place in the vicinity of the ground. Over relatively flat terrain reflections will generally cause the most dramatic effects. With respect to FWPM predictions the key issue is establishing the value of $\dot{\epsilon}_r$ for a given environment in order to accurately model the ground. As shown in Figure 4.2b, $\dot{\epsilon}_r$ determines the severity of cancellation/reinforcement and thereby the quality of the prediction as shall be shown. Since conditions of the soil change with seasonal variations, the actual electrical parameters will seldom be known and a working approximation must thus be established.

4.4.1 Open Area Measurements

A field akin to an open area test site was identified just outside Stellenbosch in order to conduct measurements under conditions resembling the simulation environment in terms of flat ground. Thus, during December 2015, measurements were specifically carried out as part of this dissertation to establish the integrity of the modelling setup. An overview of the field and a representative configuration are shown in Figure 4.9. A printed circuited board (PCB) LPDA (henceforth designated KLPDA*) was connected to the battery-operated Anapico signal generator to form the transmitting unit while the receiver unit comprised a similar KLPDA and a Rohde & Schwarz handheld spectrum analyser (FSH4). With the transmitting antenna fixed at a height of 5 m and the receiving antenna at 2 m, the maximum received power was recorded at five distances between 20 and 200 m. Correction was made for attenuation through 12 m of Huber+Suhner SF104 sucoflex cable during data analysis. A summary of the equipment used is

*This antenna was designed by Prof Keith D. Palmer

Table 4.1: Equipment used for Open Area Measurements

AnaPico APSIN6010 Generator	
output power (used)	20 dBm
frequency range (total)	0.009 – 6100 MHz
Tx and Rx: PCB-LPDA (KLPDA)	
average gain	∼5 dBi
frequency range	400 – 6000 MHz
FSH4 Handheld Spectrum Analyser (SA)	
sensitivity	−141 dBm
frequency range	0.009 – 3600 MHz

presented in Table 4.1 while the results – designated dataset-3 (DS3) – are shown in Figure 4.10. Most apparent in the transmission loss curves is the manifestation of phase changes which are a consequence of ground reflections. The fading and peaking leads to some deviation from the well-known path loss curve represented by free space loss (FSL), yet is tracked very well by the numeric data. It is interesting to note that in all but the 20 m case, the FWPM predictions were synchronized in phase, albeit with noticeable differences in amplitude (∼5.1 dB between dry and medium dry grounds and ∼7.2 dB between dry and wet grounds). Although all three FWPM predictions yielded very good results (RMSE < 6 dB), the best approximation to the measured data was the medium dry ground setup with an overall RMSE of 5.43 dB (see Table 4.2).

Observed deviations for $d_m > 20$ m are plausibly due to a difference in the radio path length encountered during measurement versus the ideal environment in simulation. Although rare for the configuration in question, a possible explanation is that a surface duct occurred due to layers of cool and warm air close to the ground. This would result in a path length longer than the geometric distance [113]. Indeed, post-analysis revealed that better matches would be obtained by increasing the path length in the FWPM setups.

Table 4.2: Mean Prediction Error and RMSE Analysis for the FWPM Validation by Open Area Measurements

d_m	Prediction Error, $\bar{\varepsilon}$ [dB]				RMSE [dB]			
[m]	dry	med	wet	FSL	dry	med	wet	FSL
20	3.94	4.07	4.39	15.47	4.46	4.43	4.78	15.58
50	5.32	5.50	5.84	16.68	6.22	6.41	6.81	17.18
100	6.76	6.10	5.82	15.52	7.46	6.90	6.69	15.81
150	4.86	4.49	4.37	14.36	5.80	5.59	5.61	15.08
200	3.17	3.14	3.14	11.50	3.80	3.85	3.91	11.93
mean	4.81	4.66	4.71	14.71	5.55	5.43	5.56	15.12

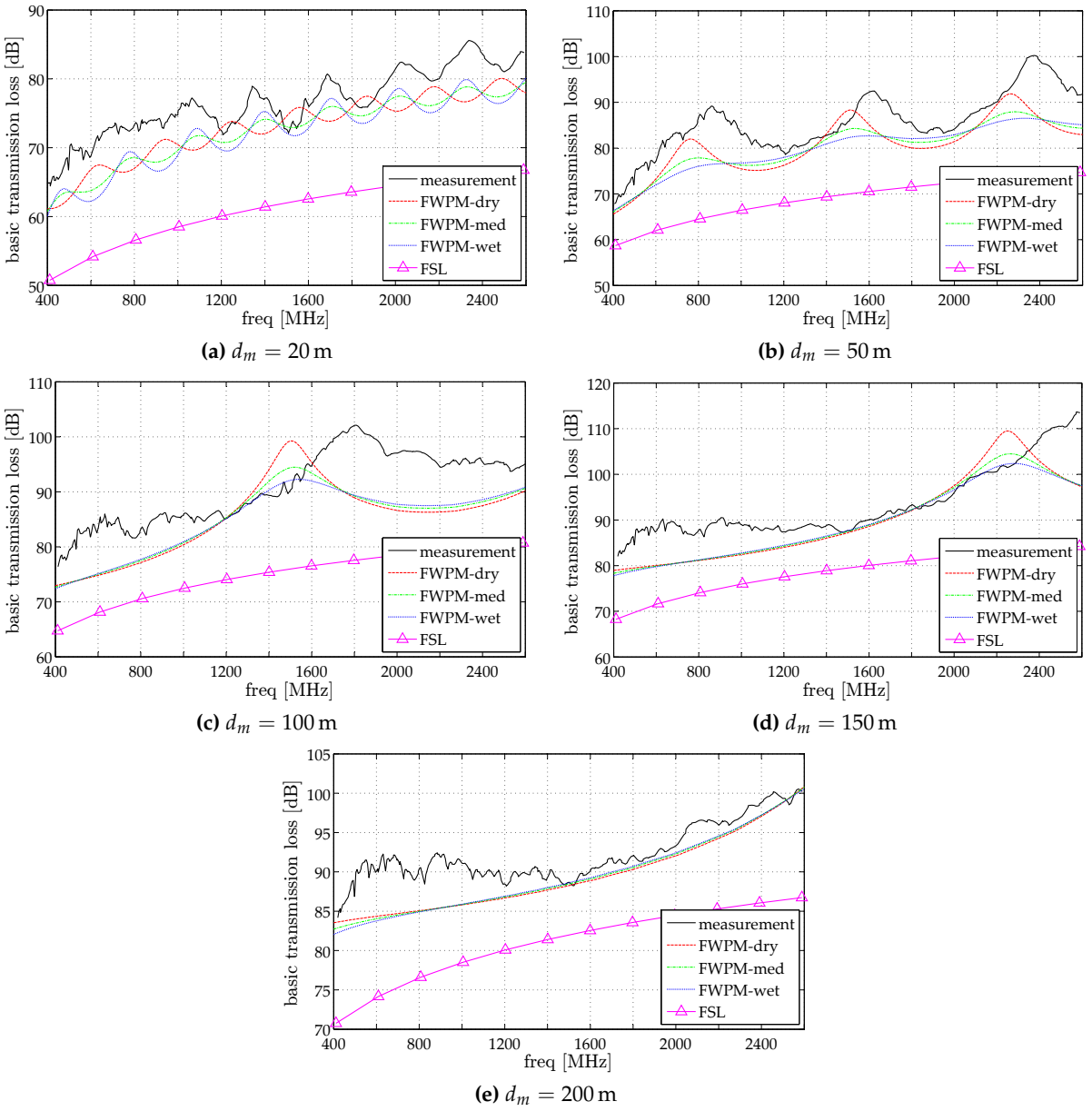

(a) $d_m = 20\,\text{m}$ **(b)** $d_m = 50\,\text{m}$

(c) $d_m = 100\,\text{m}$ **(d)** $d_m = 150\,\text{m}$

(e) $d_m = 200\,\text{m}$

Figure 4.10: Open area measurements and predictions of basic transmission loss for dataset-3. In all cases $h_t = 5\,\text{m}$ and $h_r = 2\,\text{m}$

4.4.2 Terrain Measurements (DS1 and DS2)

Dataset-1 (DS1) and dataset-2 (DS2) were obtained during a measurement survey at the MeerKAT site in July 2014 and were the basis of the evaluation of standard propagation models in Section 3.3. Receiver height (h_r) was fixed at 2 m while transmitter heights were 5 and 7.5 m, respectively. For both configurations, recordings were taken at 50, 200, 700, 1800 and 3600 m.

Measured and predicted (FWPM) path loss curves are shown in Figures 4.11 and 4.12, with free space loss (FSL) included as a familiar reference. As with DS3, the FWPM predictions diverge a little at frequencies corresponding to cancellation and reinforcement but otherwise yield much the same results. Overall, the numeric data provide an excellent fit to the measurements for both configurations which interestingly are more accurate at the longer path lengths. Statistical

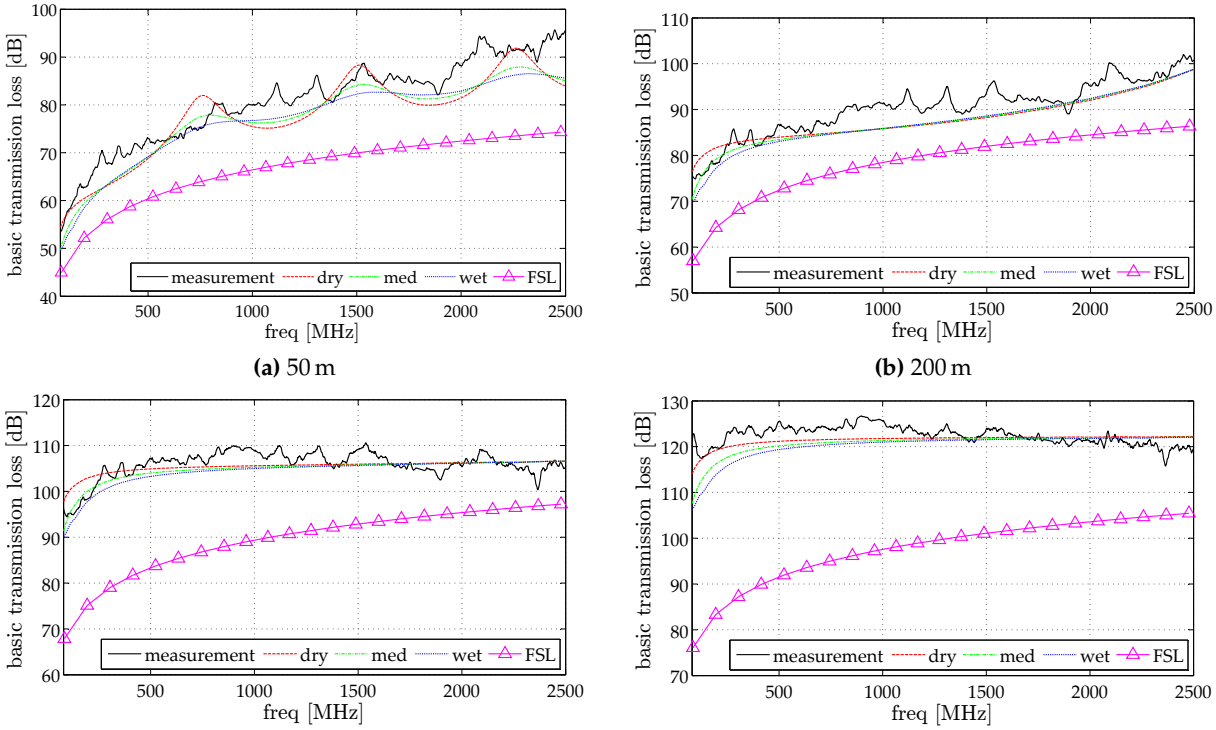

(a) 50 m **(b)** 200 m

(c) 700 m **(d)** 1800 m

Figure 4.11: Comparison of FWPM basic transmission loss predictions to dataset-1: $h_t = 5\,\text{m}$, $h_r = 2\,\text{m}$

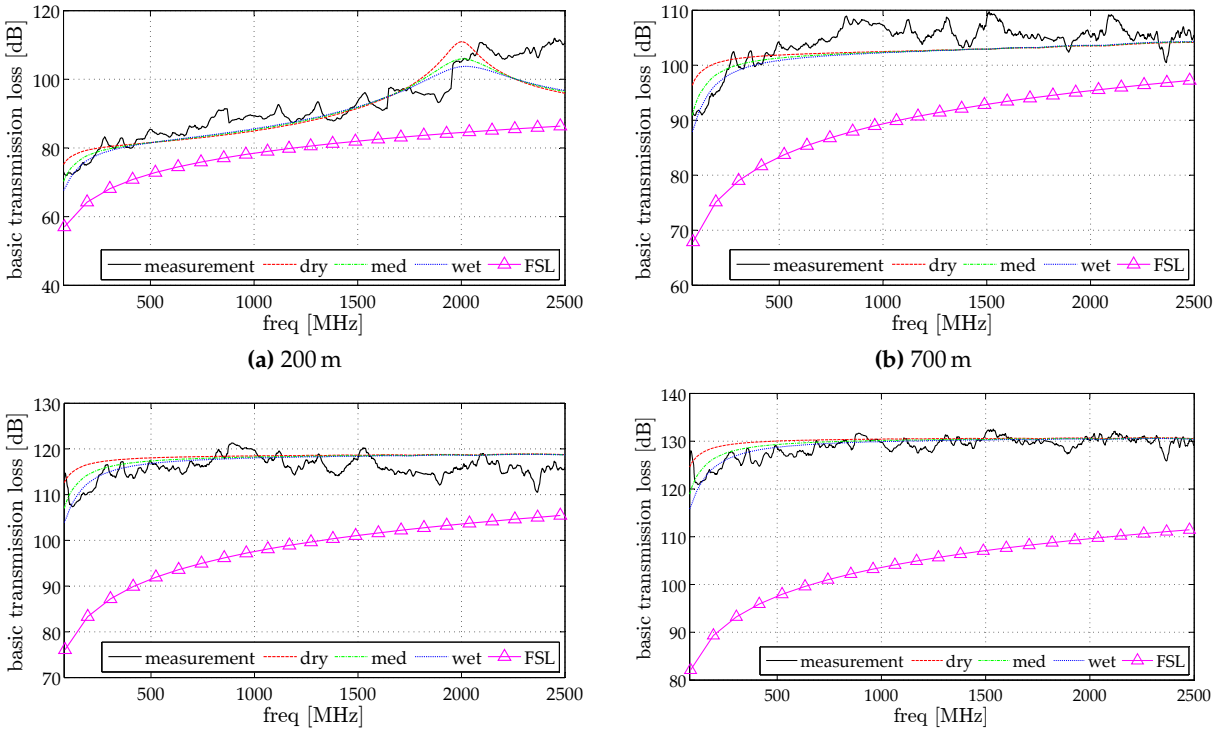

(a) 200 m **(b)** 700 m

(c) 1800 m **(d)** 3600 m

Figure 4.12: Comparison of FWPM basic transmission loss predictions to dataset-2: $h_t = 7.5\,\text{m}$, $h_r = 2\,\text{m}$

analysis on the FWPM predictions is provided in Table 4.3. Highly impressive values of RMSE were obtained for all three types of ground ($< 4\,\text{dB}$ RMSE). However, taking the overall mean, medium ground provides the best approximation with an RMSE of 3.46 dB. This finding is not

Table 4.3: Statistical Analysis of FWPM: Path Loss Predictions over Karoo Terrain

	Dataset-1							
d_m	Prediction Error, $\bar{\varepsilon}$ [dB]				RMSE [dB]			
[m]	dry	med	wet	FSL	dry	med	wet	FSL
50	3.96	3.76	3.93	14.29	4.80	4.41	4.54	14.59
200	2.99	2.84	2.98	11.81	3.50	3.38	3.44	12.04
700	1.89	1.90	2.17	16.15	2.34	2.30	2.59	17.14
1800	1.93	2.50	2.92	24.38	2.35	3.12	3.75	25.47
3600	3.14	2.63	2.42	26.38	3.37	2.96	2.88	27.11
mean	2.78	2.72	2.88	18.60	3.27	3.23	3.44	19.27
	Dataset-2							
50	4.94	4.51	4.53	15.06	5.92	5.63	5.71	15.80
200	4.30	3.82	3.75	13.80	5.68	5.23	5.11	14.79
700	2.74	2.59	2.57	14.59	3.29	3.06	3.05	15.30
1800	2.77	2.45	2.26	17.89	3.23	2.85	2.74	18.95
3600	1.61	1.27	1.08	24.87	2.13	1.65	1.56	25.41
mean	3.27	2.93	2.84	17.24	4.05	3.69	3.63	18.05

to be taken to imply that Karoo soil absolutely corresponds to medium dry ground, which is characterised by a relative permittivity (ϵ_r) of $\sim$15. On the contrary, attempts to extract the electrical parameters of Karoo soil yielded a value of 3.8 for ϵ_r [114]. However, this contradiction is not problematic since this work does not attempt to determine the value of ϵ_r but focuses on accounting for its effects with respect to obtaining the best predictions. Determining the exact value of complex permittivity is desirable but highly challenging particularly since properties such as compactness and moisture content of the soil change as soon as it has been removed from its locale. Hence, for propagation modelling, finding the best fit using existing data may be the most practical approach.

4.5 Measurements at KAT-7: Ray Model Verification

Capacity to deterministically model scattering effects from full scale radio astronomy receptors was demonstrated in Section 4.2.2.3. To establish the prediction accuracy, it is necessary to assess the ray model (MoM-PO hybrid) against measured data. Thus, a measurement campaign was conducted at the KAT-7 site during August 2016. These measurements comprise dataset-4 (DS4).

Essentially the same equipment as for the open area measurements was used except that the FSH4 spectrum analyser (SA) was replaced with an FSH8. The transmitting KLPDA was placed at the estimated centre of the array (21.4107, -30.721441) and set to a height of 3.6 m. With the receiving antenna fixed at a height of 2.51 m and the SA on maximum hold, recordings were made in three respective radial arms (from the centre) at 10, 20, 50, 70 and 100 m while sweeping

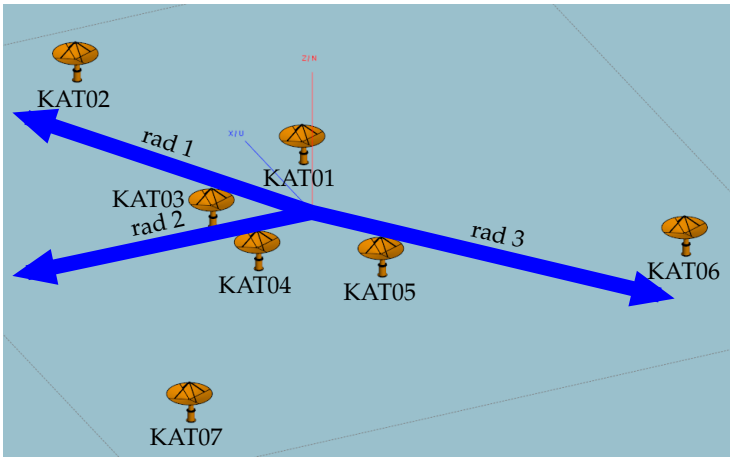

Figure 4.13: Orientation of radial arms relative to KAT-7 array configuration

in frequency from 400 to 3100 MHz. The geographical coordinates were logged at each receiver position so as to reproduce those locations precisely in simulation. To make certain that no external signals would be mistaken for data points, background noise was measured at each receiving position. The respective radial arms are illustrated in Figure 4.13 while some images of measurements in progress are shown in Figure 4.14.

In the interest of EMC, the output power of the Anapico signal generator had to be limited to −20 dBm as per the guidelines from the SKA-SA. Consequently, a ∼25 dB low-noise amplifier (LNA) was used at the receiving antenna, otherwise the signal rapidly faded into the noise floor of the FSH8 SA. Cable loss at the transmitter was removed by connecting the signal generator directly to the FSH8 to obtain the power arriving at the antenna port. Attenuation through the cable at the receiving end was accounted for during post-processing.

4.5.1 Repeatability and Uncertainty

Besides uncertainty in the measuring equipment, a source of error during the survey included the presence of maintenance staff and vehicles/machinery close to the measurement locations (see Figure 4.14b), potentially resulting in some unwanted scattering effects. Random error due to misalignment could have also been aggravated by the occasional strong winds beating against the antennas. Hence, it was essential to establish the uncertainty in the measurements. This was done by repeating recordings at 70 m in radial arms 1 and 2 and at 20 m in radial arm 3. Results are displayed in Figure 4.15. Based on the residue between the primary and repeated values at each frequency point, the standard deviation, s^*, was computed and subsequently expressed as a standard error, SE [115]. The maximum values of the respective errors were 3.71, 2.55 and 0.73 dB. Taking the worst case scenario, the SE of the measurements is determined to be 3.71 dB. Hence, the uncertainty in the measurements (to two significant figures) was ±1.9 dB.

*Deliberately, s is used here so that there is no confusion with ς for path loss analysis in the previous chapter

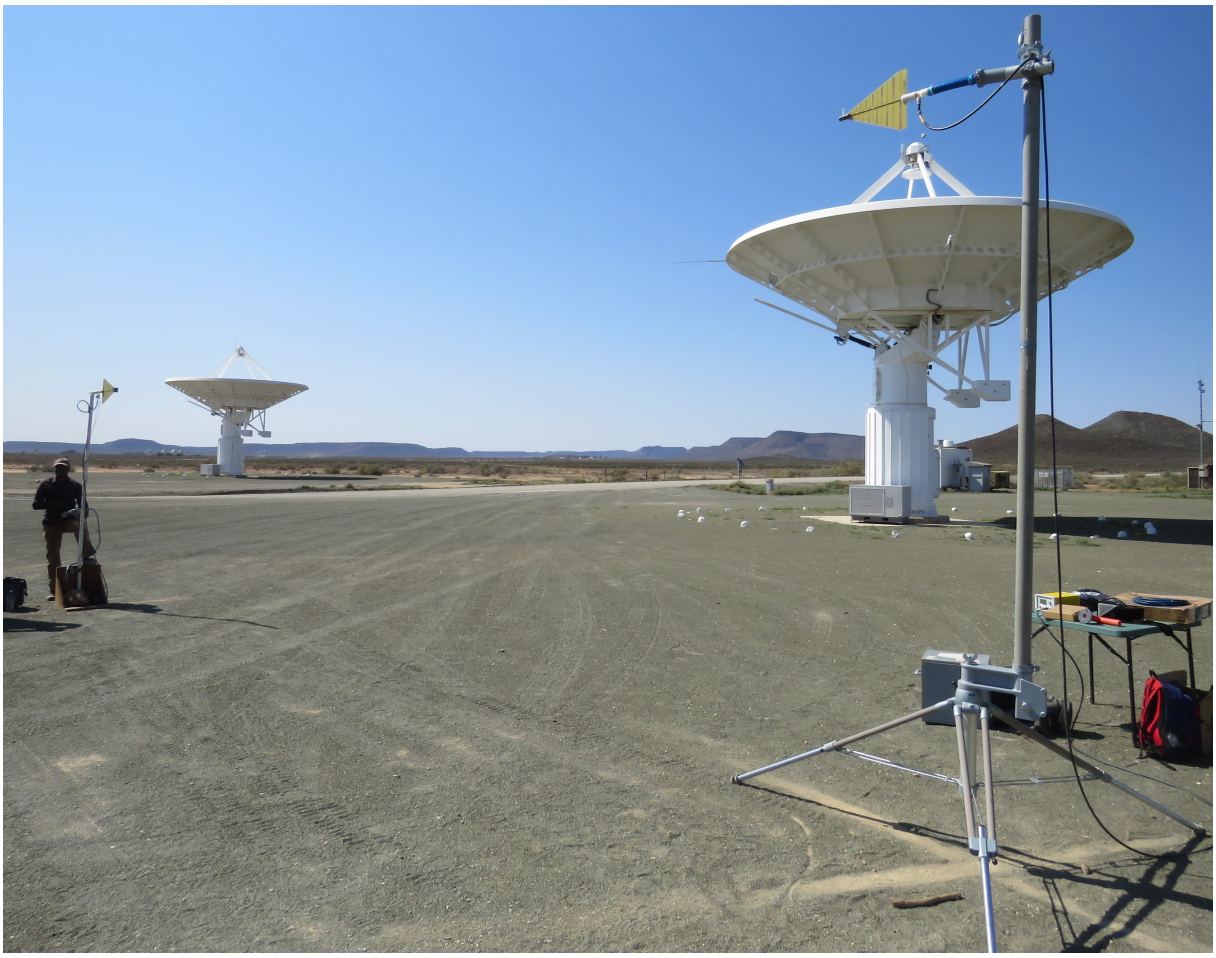

(a) radial arm 1, 20 m

(b) radial arm 2, 20 m

Figure 4.14: Measurement campaign at KAT-7 during August 2016. KAT1 (right) and KAT2 (left) can be seen in the background of (a), while KAT4 (right) and KAT5 (left) form part of the background in (b). Image credits: The author

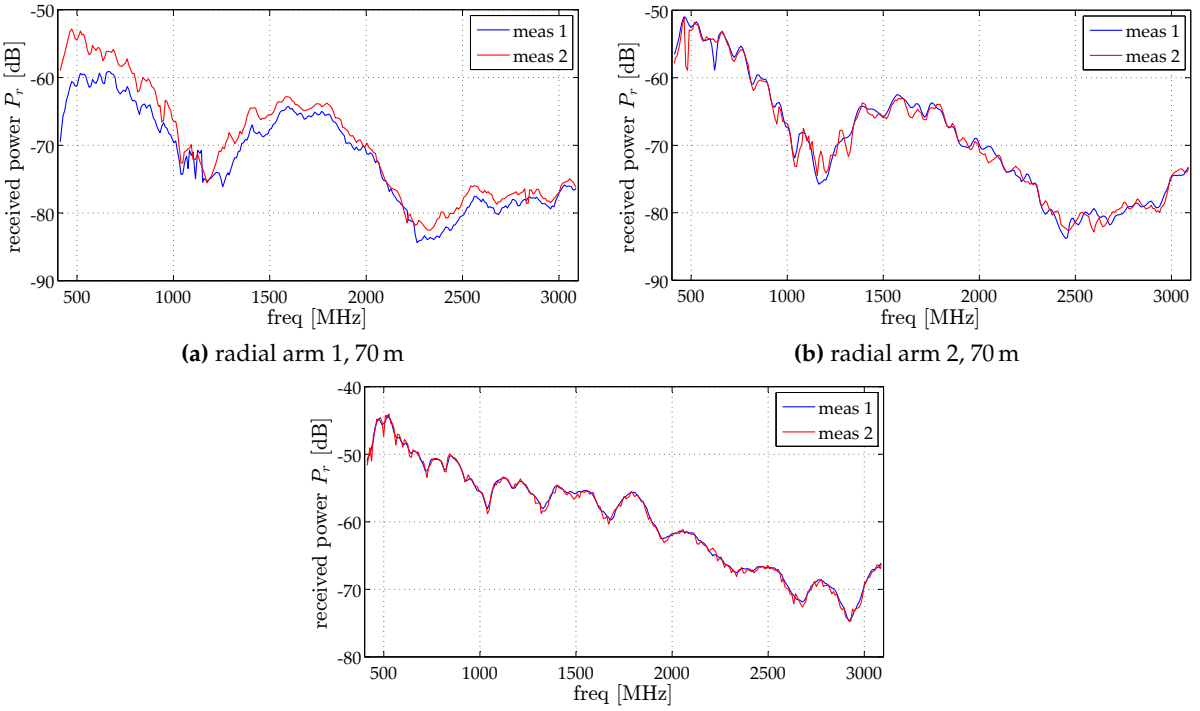

(a) radial arm 1, 70 m

(b) radial arm 2, 70 m

(c) radial arm 3, 20 m

Figure 4.15: Repeatability check for measurements at KAT-7

4.5.2 Results and Analysis

The measured and simulated data are plotted in Figures 4.16 to 4.18. Even though the number of scatterers in each path was greatly minimised by the setup, the data exhibit fluctuations in amplitude which are representative of fading. As can be seen by comparison to the case of a regular half-space (full-wave solution over real ground), multipath effects did not significantly affect the magnitude of the received field. What is remarkable here is that the ray model provides all the information that would be revealed by measurement, namely, the rapid amplitude variations and the particular frequencies where nulls occur. This is confirmed by the strong linearity given by the correlation coefficient ($\rho \geq 0.91$) demonstrated for 12 out of 15 radio links in DS4 (see Table 4.4).

Table 4.4: Statistical analysis of the ray model predictions with respect to DS4

d_m	radial arm 1				radial arm 2				radial arm 3			
[m]	RE	ρ	$\bar{\varepsilon}$ [dB]	RMSE [dB]	RE	ρ	$\bar{\varepsilon}$ [dB]	RMSE [dB]	RE	ρ	$\bar{\varepsilon}$ [dB]	RMSE [dB]
10	0.02	0.95	1.33	1.62	0.07	0.95	4.91	5.41	0.04	0.98	2.78	3.28
20	0.03	0.93	2.77	3.32	0.03	0.93	2.05	2.62	0.03	0.93	2.33	2.97
50	0.04	0.93	3.28	3.74	0.04	0.83	3.33	4.40	0.03	0.93	2.25	2.80
70	0.05	0.91	4.14	4.71	0.03	0.91	2.96	3.63	0.04	0.84	3.41	4.23
100	0.04	0.85	3.47	4.38	0.04	0.92	3.59	4.53	0.03	0.92	2.81	3.53
mean	0.03	0.91	3.00	3.55	0.04	0.91	3.37	4.12	0.03	0.92	2.72	3.36

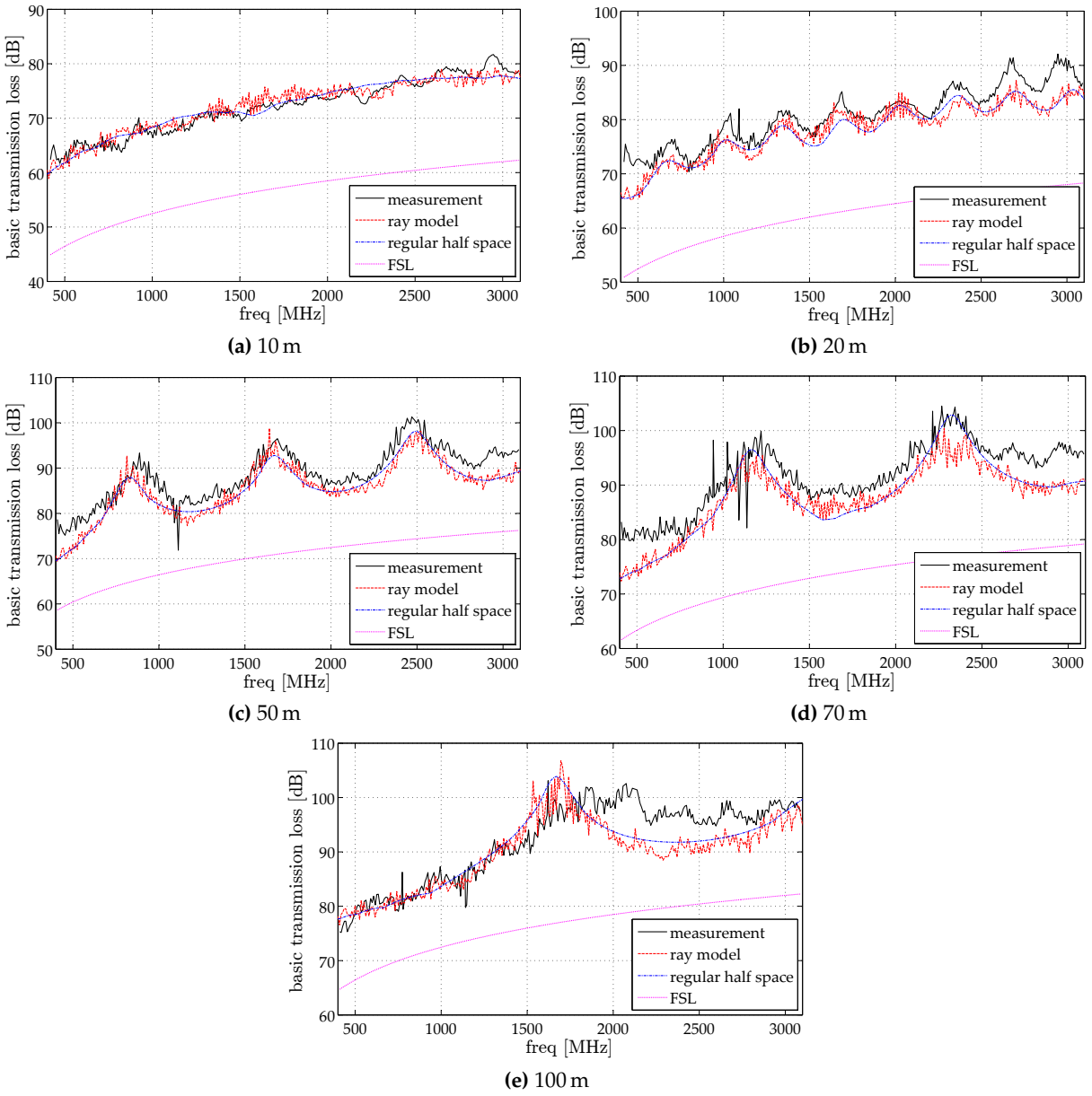

(a) 10 m **(b)** 20 m

(c) 50 m **(d)** 70 m

(e) 100 m

Figure 4.16: Basic transmission loss in radial arm 1

Predictions for radial arm 1 were particularly good – synchronised in fading and peaking as well as amplitude. There was little deviation from the measurements as evidenced by the small prediction error ($\bar{\varepsilon}$) and RMSE values of 3.0 and 3.55 dB, respectively, for the subset.

Amplitude and phase differences were more apparent in the comparison of results for radial arm 2, particularly at 20 and 50 m (see Figure 4.17). However, on a statistical level the forecasting was actually accurate as attested to by an RMSE of 5.41 dB corresponding to the worst prediction. Overall for the subset, the prediction error was 3.37 dB while RMSE was 4.12 dB.

Predictions for radial arm 3 compare well with the measurements yielding a RMSE of 3.36 dB overall. Clear deviation was observed at 70 m, plausibly on account of radio path length differences between measurement and simulation. It is no surprise then that the corresponding linearity was somewhat poor (ρ <0.9). Nonetheless, a good relative error of 0.04 and favourable prediction error of 3.41 dB was obtained for the link.

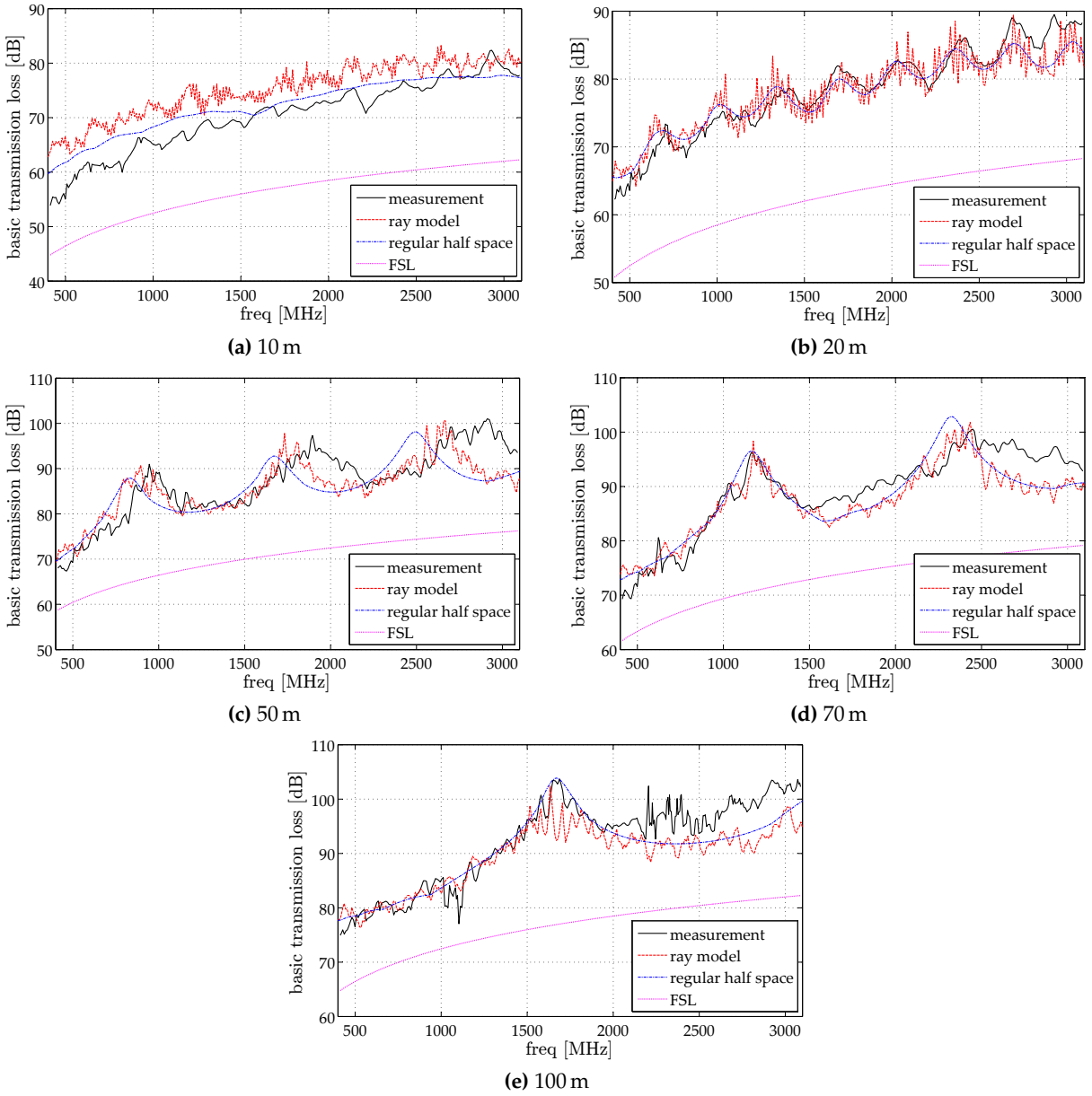

(a) 10 m **(b)** 20 m

(c) 50 m **(d)** 70 m

(e) 100 m

Figure 4.17: Basic transmission loss in radial arm 2

On the whole, the ray tracing model is without question extremely accurate within the sampled parameter space. Taking the overall mean values, the relative error for the predictions was 0.03 with a correlation coefficient of 0.91. Although there was some significant deviation observed for a few links, the prediction errors did not exceed 5 dB and the gross RMSE was an unprecedented 3.68 dB.

Three simulations were run for the respective radial arms. Computational resources for each run were 12 cores and a total memory of 2.81 GB for a runtime of 1.15 h. Antennas were modelled based on the far-field data of the LPDA mentioned in Section 4.2.1.1. With respect to ground, the relative permittivity and conductivity were set to very dry ground as this gave the best prediction. A shortcoming of the numerical modelling is the fact that waves reflected

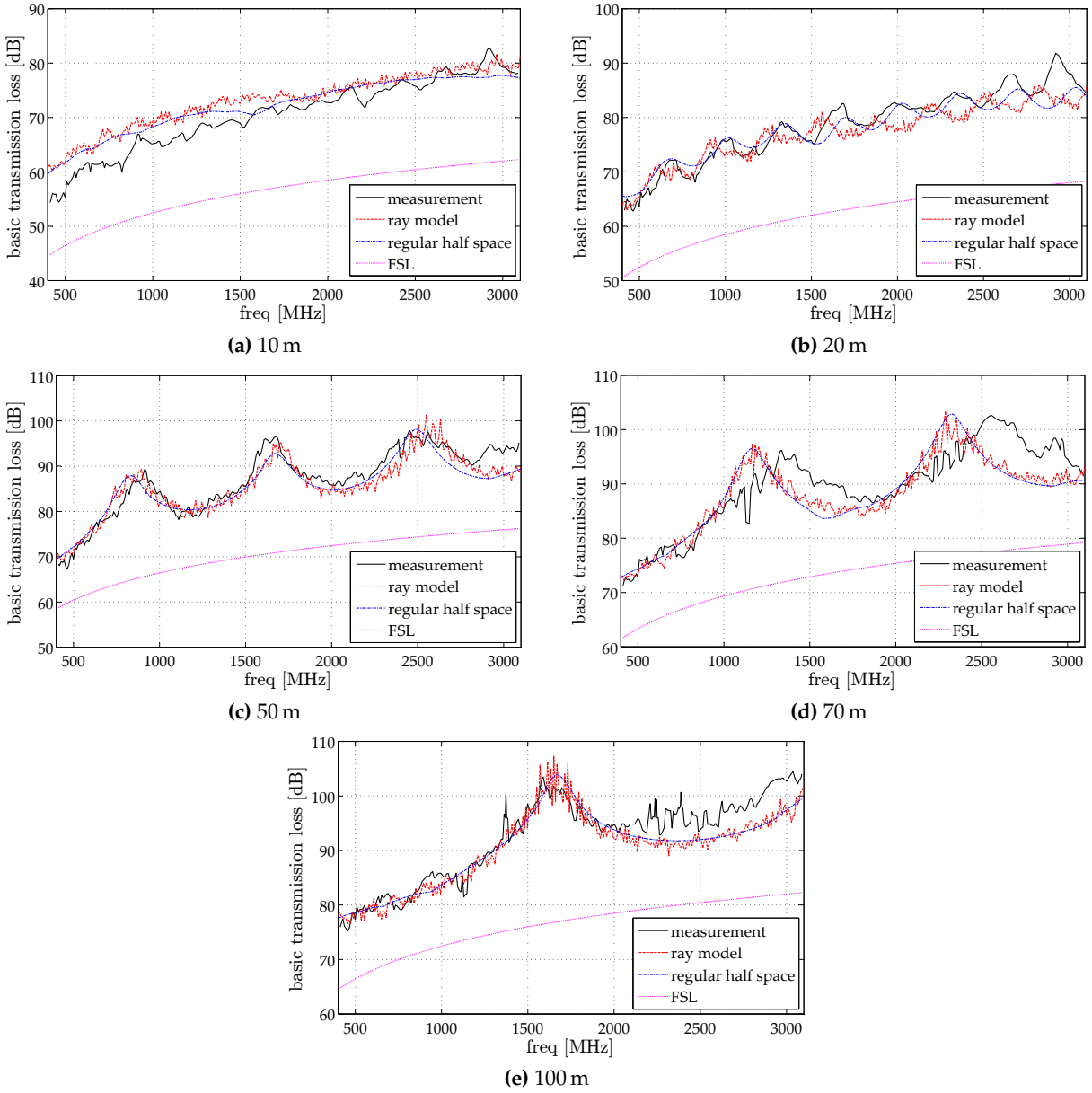

(a) 10 m **(b)** 20 m

(c) 50 m **(d)** 70 m

(e) 100 m

Figure 4.18: Basic transmission loss in radial arm 3

from real ground are not taken into account on a PO region. Even so, this did not seem to compromise the quality of the predictions.

4.6 Summary

Numerical path loss modelling techniques in FEKO have been presented. Using the method of moments (MoM), we realised the full-wave propagation model (FWPM) which can be used for predictions over relatively flat terrain with great success (refer to Section 4.4.2). Comparison to measured data yielded aggregated root mean square errors (RMSE's) of 5.51 and 3.55 dB for open area and Karoo terrain measurements, respectively. Considering the 15 dB threshold for acceptable RMSE in rural areas, these values are impressive.

Extension was made to address scattering from metallic surfaces via a MoM-PO hybrid. Validation of this ray model was performed by checking the predictions against measurements conducted at the KAT-7 array: strong correlation ($\rho = 0.91$) and minimal error (RE $= 0.03$) were observed. This corresponded to a notable RMSE of 3.68 dB.

Thus, in the FWPM and ray model, we have validated deterministic models for path loss predictions over flat terrain and environments characterised by multiple scatterers, respectively. The novelty here is first that antenna characteristics above a real ground are modelled and taken into account in the path loss prediction. Second and most important, we have shown that the ray model is a powerful technique that can be used to realistically reproduce a deployment scenario with high accuracy. Hence, this tool can be used to characterise complex electromagnetic environments such as the MeerKAT core. This is the subject of the next chapter.

Chapter 5

Characterising the MeerKAT Core

A deterministic, ray model was developed in Chapter 4. It utilises the method of moments (MoM) for antenna and real ground modelling, while physical optics (PO) is applied for scattering from metallic surfaces – the MeerKAT dishes in this case. Having verified the predictions by comparison to measurements at KAT-7, the ray model is now applied to model 44 MeerKAT receptors within a 1 km radius of the core.

5.1 Computational Representation of the MeerKAT Core

The first step in reproducing the MeerKAT configuration was to obtain a suitable representation of a single dish. This was relatively easy to do based on previous work by Wiid and Reader [116] on characterisation of lightning-induced RFI on a MeerKAT dish, and by Kuja and Wiid [117] on investigations of signal coupling between MeerKAT telescopes. Both these studies utilised a $1/20^{\text{th}}$ computational electromagnetic (CEM) scale model of the initial MeerKAT dish design. Since the final design differs only in substructure layout, we employed the same CEM model here and scaled it up to full size. Considering the dishes themselves neither transmit nor receive signals in this work, the full scale CEM model was simplified by excluding detail such as wires and receiver indexer, as can be seen in Figure 5.1. At the highest simulation frequency of 3050 MHz, the receptor was discretised into 85 160 flat triangles with an average edge length of 0.1337 for a solution involving large element physical optics (LE-PO).

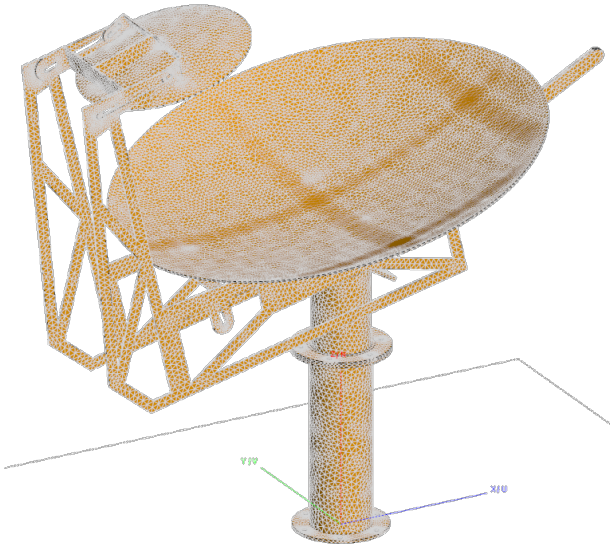

Figure 5.1: Simplified, full scale computational electromagnetic (CEM) model of a MeerKAT receptor in the stowed position.

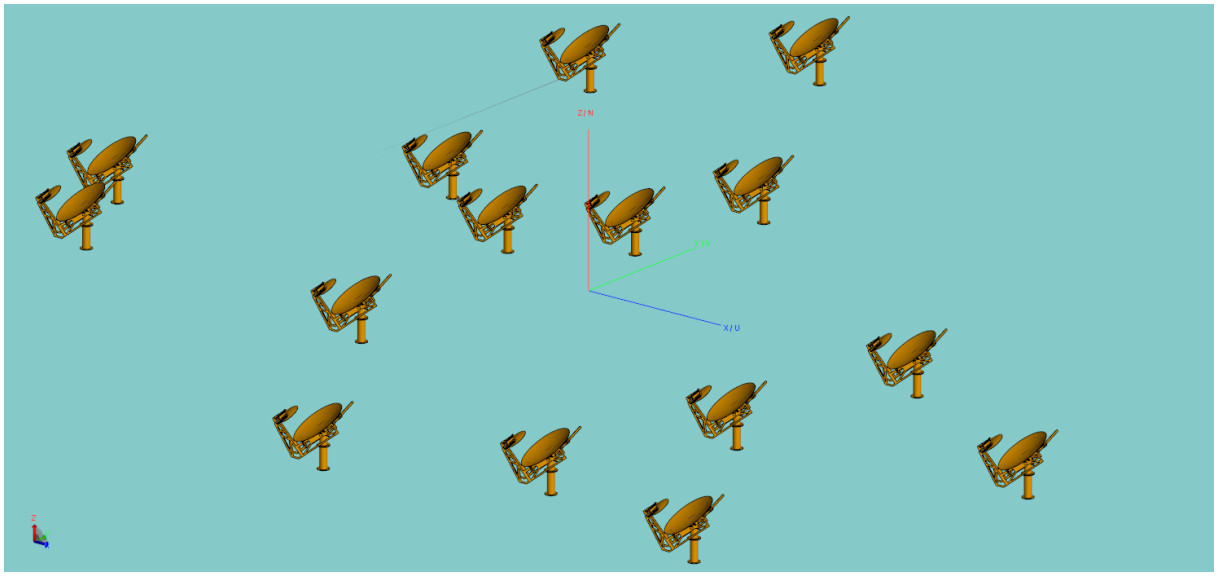

Figure 5.2: Computational representation of the MeerKAT core showing 15 dishes.

Using the positioning data from the SKA-SA public science/engineering site [118], the computational mock-up of the MeerKAT core was populated by repeated copy-paste-and-translate operations. Restricting the range to a radius of 1 km from the array centre, the total number of receptors in the computational model was 44. Based on findings from the measurements at KAT-7 (dataset-4, DS4), the properties of the infinite ground plane were set to very dry ground. Figure 5.2 shows a section of the core with 15 receptors in view.

5.2 Evolution of Transmission Loss through the MeerKAT Core

It is a given that transmission loss in the environment of MeerKAT will be characterised by multipath. The challenge is to determine whether this might have any impact on the RFI protection integrity as an unwanted signal propagates through the core. Using LPDA and $\lambda/2$ dipole data, directional and omni-directional noise sources were respectively modelled. For both cases, the source was placed at the centre of the array.

5.2.1 Reference Attenuation as Function of Height

Sweeping in frequency from 350 to 3050 MHz, the LPDA equivalent source was positioned at a height of 11 m. The received power at a distance of 900 m from the array centre was then computed at heights between 2 and 11 m along the four cardinal directions (east, north, west, south) in succession. This simulation setup was solved for the receptors orientated in southwest and northeast directions, dubbed orientation 1 and orientation 2, respectively. The corresponding results are shown in Figures 5.3 and 5.4.

The presence of fast fading can be seen in the sharp amplitude fluctuations. Yet, it is also clear that the deviation from the regular half-space (real infinite ground with no dishes) is minimal. In fact, except for the northern direction, the reference attenuation (A_{ref}) does not deviate significantly from the regular half-space. In both Figures 5.3 and 5.4, A_{ref} in the northern direction

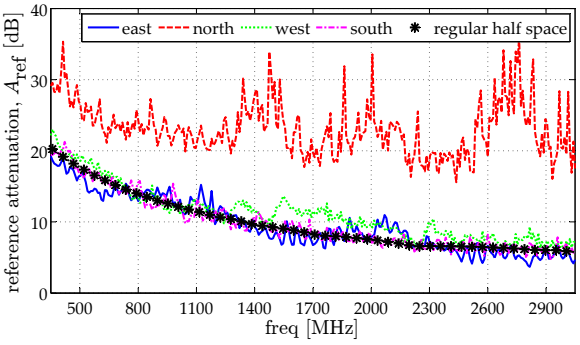

(a) $h_r = 2\,\text{m}$

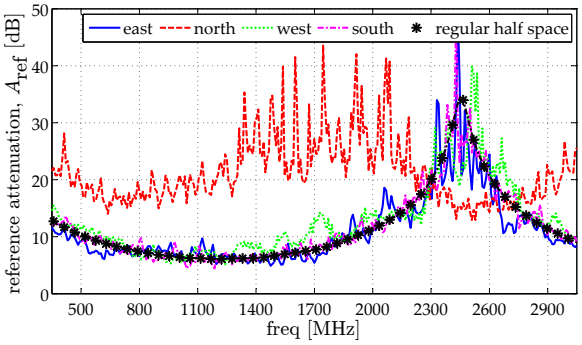

(b) $h_r = 5\,\text{m}$

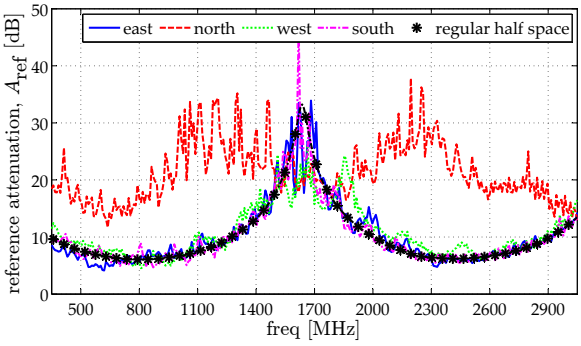

(c) $h_r = 7.5\,\text{m}$

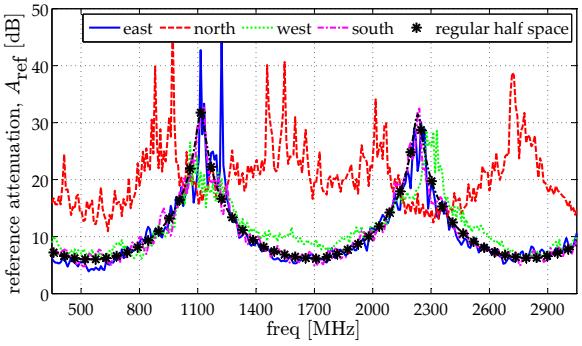

(d) $h_r = 11\,\text{m}$

Figure 5.3: Reference attenuation, A_{ref}, as a function of receiver height with MeerKAT receptors in orientation 1 (facing southwest). The noise source was modelled on LPDA far-field data.

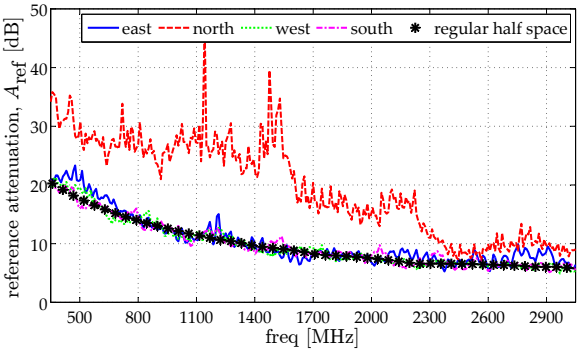

(a) $h_r = 2\,\text{m}$

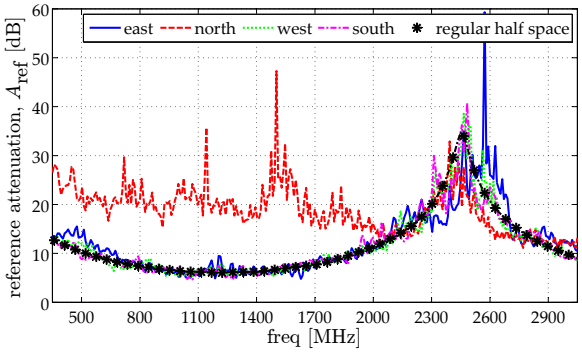

(b) $h_r = 5\,\text{m}$

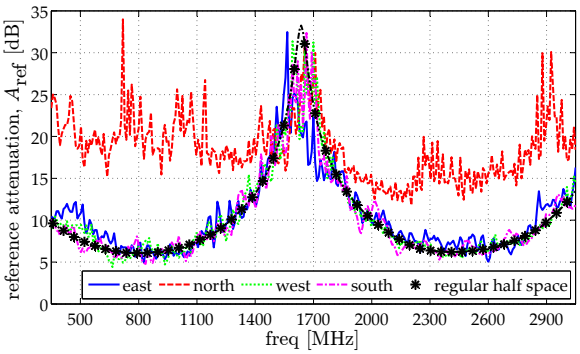

(c) $h_r = 7.5\,\text{m}$

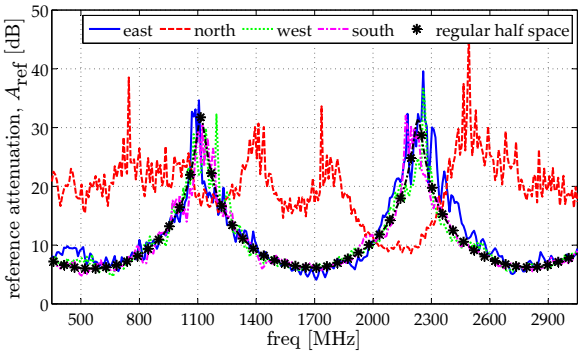

(d) $h_r = 11\,\text{m}$

Figure 5.4: Reference attenuation, A_{ref}, as a function of receiver height with MeerKAT receptors in orientation 2 (facing northeast). The noise source was modelled on LPDA far-field data.

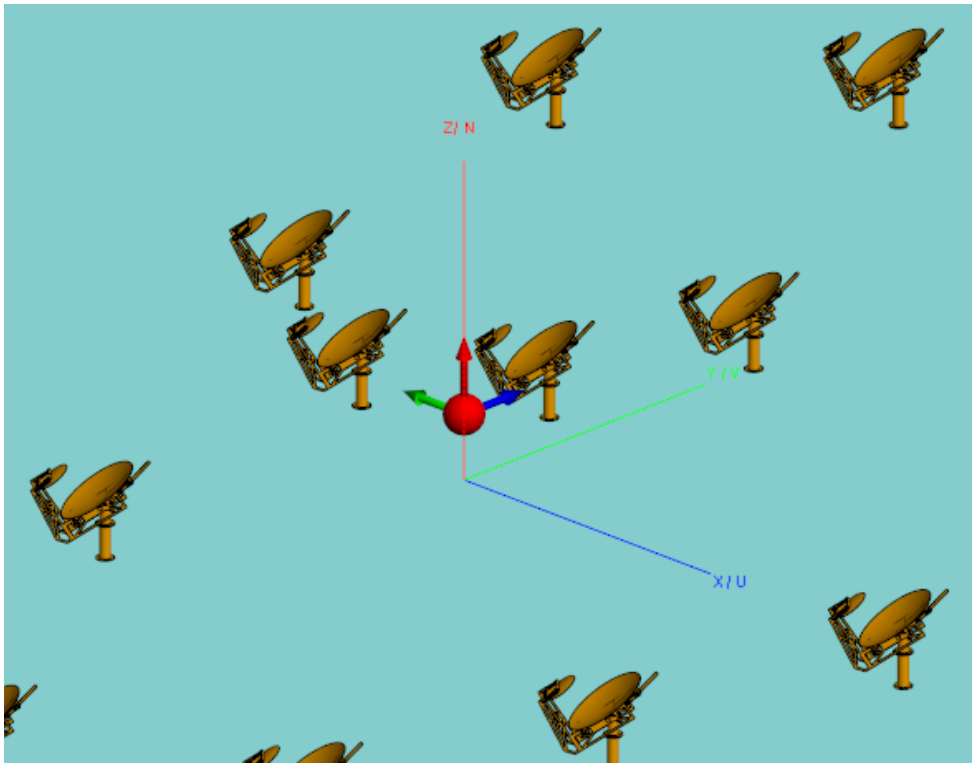

Figure 5.5: Configuration of noise source (LPDA) and receptors for transmission in the northern direction as indicated by the blue arrow. Here the receptors are shown in orientation 1.

exhibits a different trend and has a higher loss. At the frequencies where this is not true, the attenuation is still ∼10 dB above free space loss (FSL) and as such is not problematic. Deviation of the results in the northern direction can be understood by taking a look at the setup in Figure 5.5. As can be seen, there are two receptors that obscure the line-of-sight (LOS) path. Hence, the generally lower attenuation is due to a shadowing effect by reflection of a significant portion of the field away from the receiver.

We can infer from Figure 5.5 and the attenuation curves (Figures 5.3 and 5.4) that if there is a minimally obstructed path, the FWPM (MoM-only solution for a half-space) will give a fair prediction of the loss. Based on the results, height does not have a significant effect on the reference attenuation except to affect the path length difference. Of course this influences which frequencies will correspond to cancellation and/or reinforcement. Yet, in terms of amplitude, the worst case scenario does not go lower than 5 dB. Put differently, whatever the receiver height, A_{ref} is always at least 5 dB above FSL given a directional source and a path length of 900 m within the MeerKAT core.

5.2.2 Reference Attenuation as a Function of Distance – Case 1: Directional Source

The severity of a multipath environment is much more discernible by single frequency analysis wherein the attenuation is viewed as a function of distance. The same setup as in Section 5.2.1 was used, except that the electric field – rather than power – was computed at the same height as the source (11 m) from the array centre up to a radial distance of 900 m in steps of 2 m. As with the height analysis, this was done successively in each cardinal direction for both

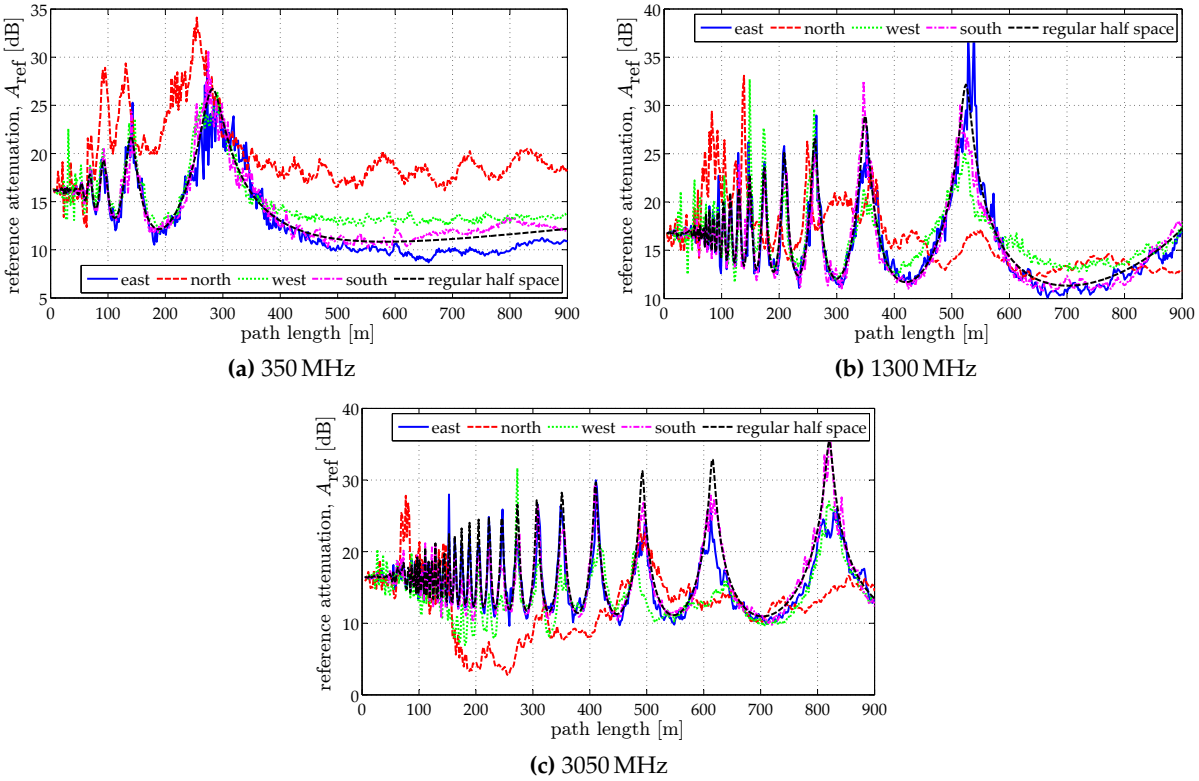

(a) 350 MHz

(b) 1300 MHz

(c) 3050 MHz

Figure 5.6: Reference attenuation as a function of distance with MeerKAT receptors in orientation 1. The transmitting antenna was modelled on LPDA far-field data to represent a directional noise source.

orientations 1 and 2 of the MeerKAT receptors. The results are shown in Figures 5.6 and 5.7.

For both orientations, we observe that at 350 and 1300 MHz, A_{ref} does not go significantly below 10 dB. Again, the fact that at these frequencies the predictions for the MeerKAT core do not deviate much from the regular half-space is indicative of a minimally obstructed path which is dominated by the ground wave (i.e. direct and ground-reflected waves). Even though predictions for the northern direction exhibit a different trend, generally, the attenuation is greater or in the same range of magnitude as the regular half-space.
At 3050 MHz, A_{ref} in the northern direction does get quite close to the FSL value. For orientation 1, its value is 2.76 dB at 257 m, while the minimum value for orientation 2 is 3.12 dB at 181 m. This clearly indicates constructive interference of the fields at these locations as the attenuation is 16.41 dB at a distance of 5 m from the source. These are the sort of unexpected effects that arise in a complex multipath environment.

We also investigated A_{ref} for a source at a height of 5 m, keeping all other variables fixed. Due to path length differences, the curves exhibited slightly different characteristics as expected. As with the previous case, predictions for the core generally followed the corresponding regular half-space solution. The most dramatic results occurred at 3050 MHz and can be seen in Figure 5.8 (curves for 350 and 1300 MHz can be found in Appendix D). Looking at Figure 5.8a, reinforcement in the western direction was strong at 147 and 229 m, yielding A_{ref} of −1.30 and −1.96 dB, respectively. Also, the loss was essentially equal to FSL (0.35 dB) at 658 m. In Figure 5.8b, minima (below FSL) were recorded at 125, 161, 255 and 654 m with respective values

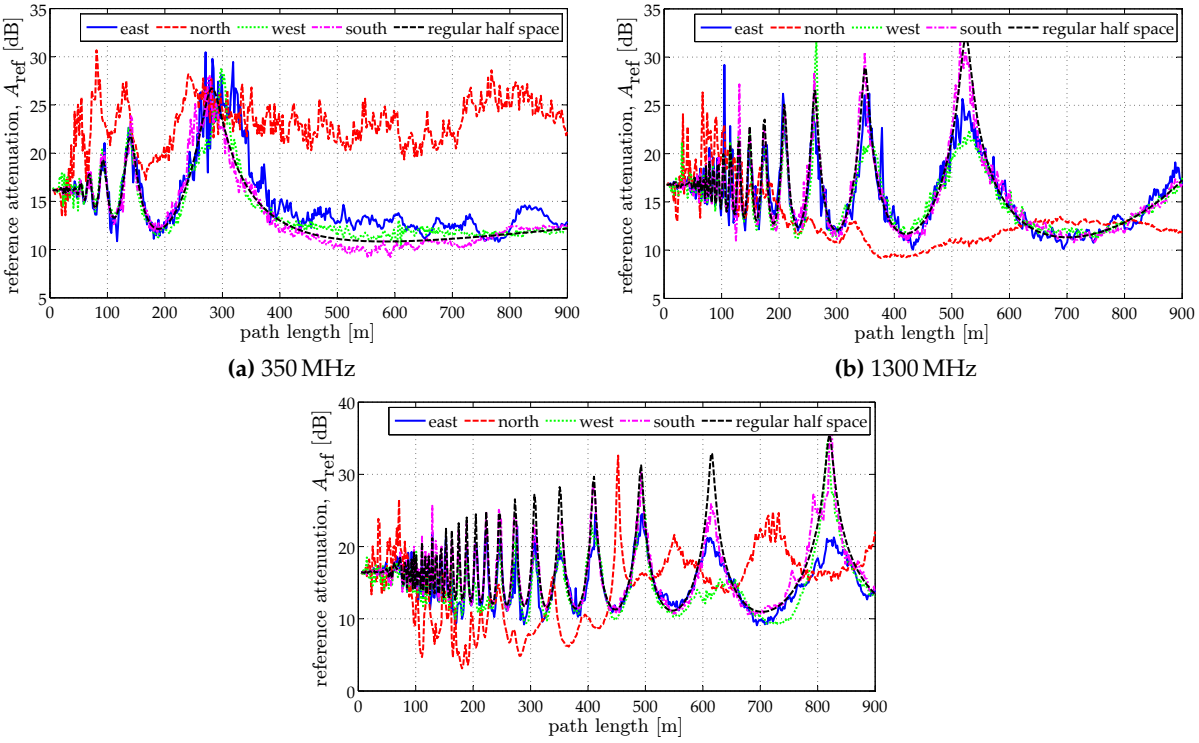

(a) 350 MHz **(b)** 1300 MHz

(c) 3050 MHz

Figure 5.7: Reference attenuation as a function of distance with MeerKAT receptors in orientation 2. The transmitting antenna was modelled on LPDA far-field data to represent a directional noise source.

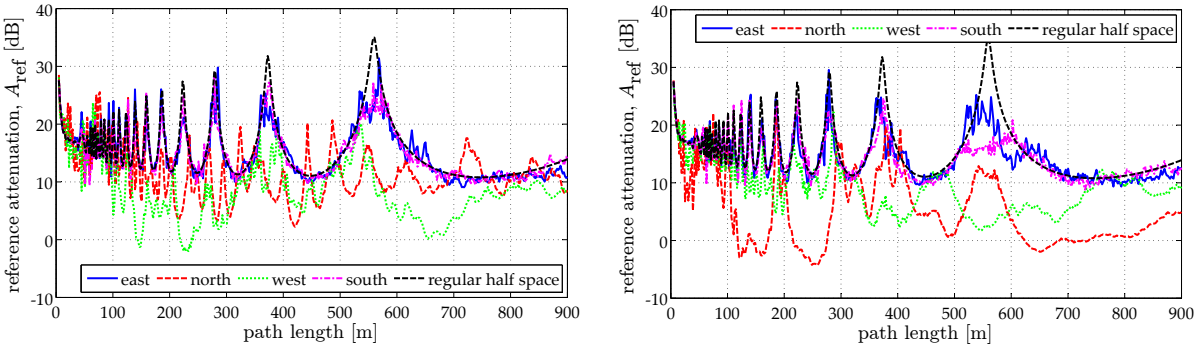

(a) orientation 1 **(b)** orientation 2

Figure 5.8: Reference attenuation at 3050 MHz for a noise source at a height of 5 m.

of −2.70, −2.62, −4.05 and −1.87 dB in the northern direction. We see from this that at high frequency, a source at a lower height than the receiver indexer could yield the most harmful effects.

Based on the evidence, estimates of the impact of a directional noise source transmitting at 350 and 1300 MHz could be obtained using a regular half-space with a ± 5 dB error margin. However, this is not universally true since only four directions and two orientations have been investigated. At the higher frequencies (represented by 3050 MHz), the reference attenuation can deviate quite substantially and precise, deterministic modelling would be required.

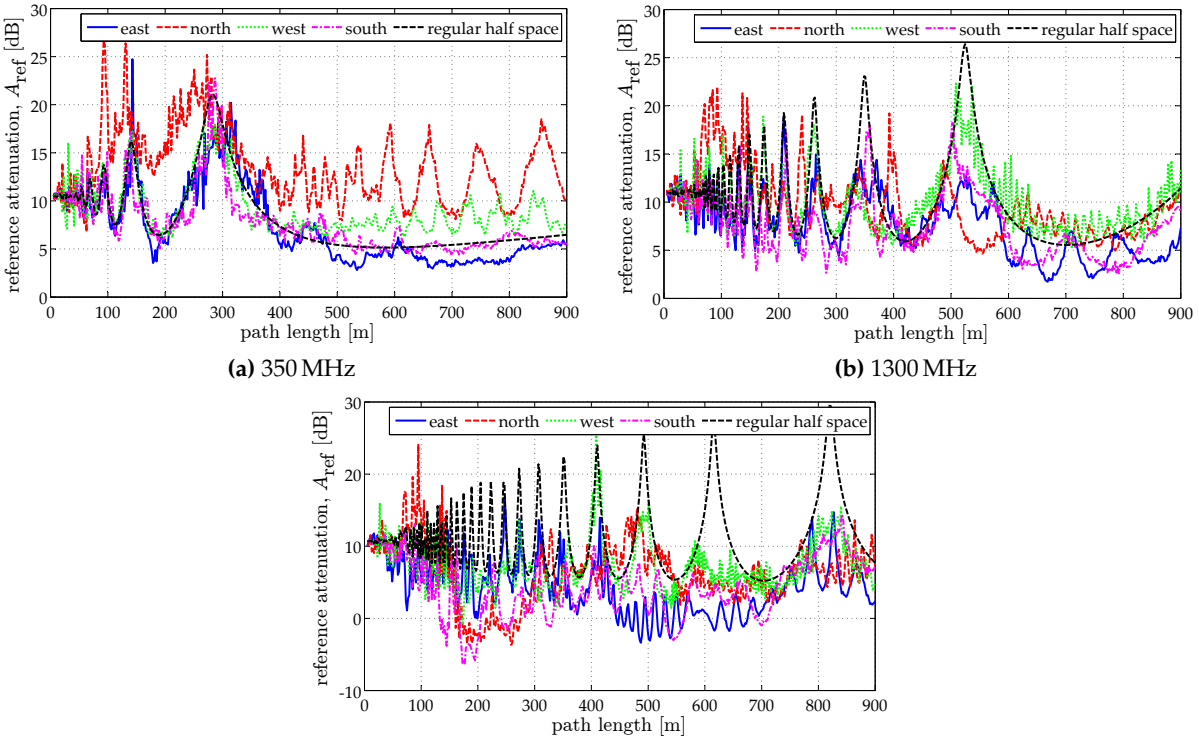

(a) 350 MHz

(b) 1300 MHz

(c) 3050 MHz

Figure 5.9: Reference attenuation as a function of distance given an omni-directional source and MeerKAT receptors in orientation 1.

5.2.3 Reference Attenuation as a Function of Distance – Case 2: Omni-directional Source

The setup in Section 5.2.2 is now repeated for an omni-directional source positioned at a height of 11 m. In addition to providing a more general perspective, analysis of this sort provides the worst case scenario for transmission loss in the MeerKAT environment. (From a simulation point of view, this is advantageous since the fields can be determined simultaneously for each direction in the same solution.) Figures 5.9 and 5.10 reveal that the received field due to an omni-directional source increases by about 5 dB compared to the case of a directional source. This is a consequence of more severe multipath. Attenuation in the eastern, western and southern directions still follow the trend of a regular half-space at 350 MHz, with the minimum value around 5 dB. Results for the northern direction have significant amplitude variations but exhibit a higher loss than the regular half-space, all the same. Interesting effects start to manifest at 1300 MHz with the attenuation deviating strongly from the regular half-space and going significantly lower than 5 dB at multiple locations. At 3050 MHz, A_{ref} is less than FSL at multiple points and spans a wide range of locations in some cases. The impact is most severe for orientation 1 than 2 where the attenuation is zero at least once in each direction. On further inspection of Figure 5.10, it can be seen that the attenuation behaves in the most dramatic fashion in the eastern direction, being equal to or less than FSL 41% of the time.

Investigating only four directions, it is clear that scenarios could arise in which reinforcement could be so pronounced as to decrease the loss below the free space value. Through the mod-

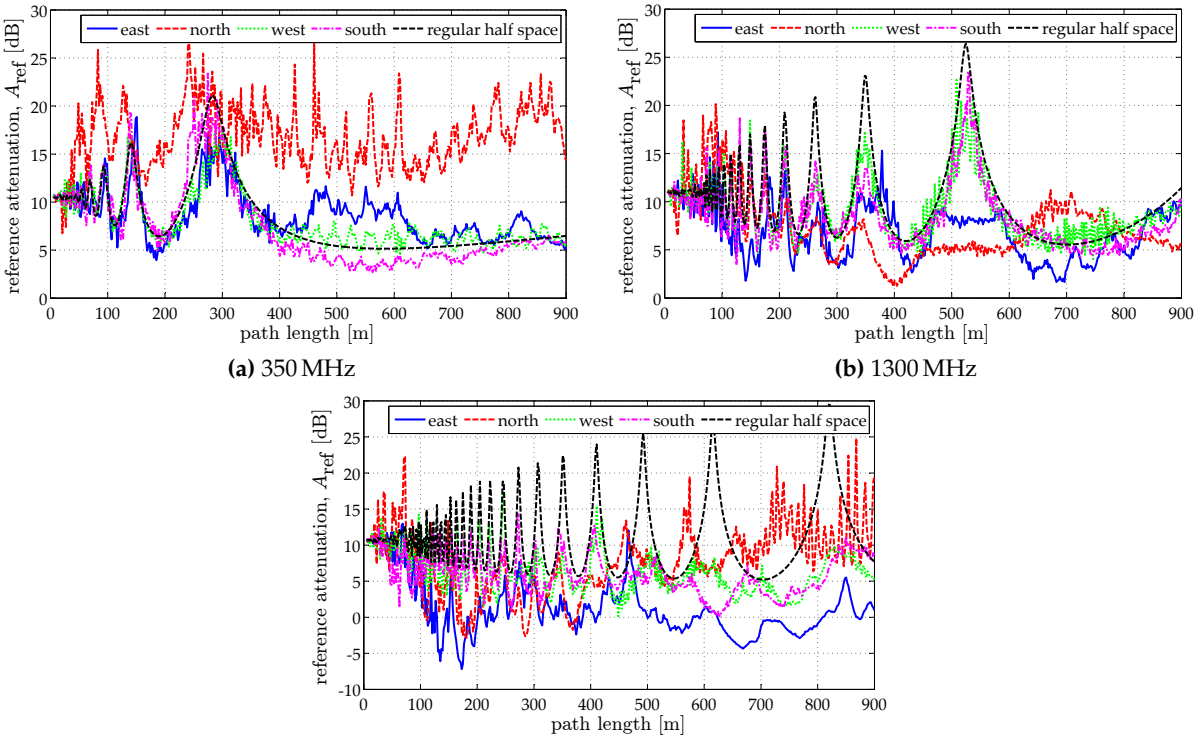

(a) 350 MHz

(b) 1300 MHz

(c) 3050 MHz

Figure 5.10: Reference attenuation as a function of distance given an omni-directional source and MeerKAT receptors in orientation 2.

elling here, the complexity of the MeerKAT core is clear. More important, the ability to model this complex environment has been clearly demonstrated. It now remains to aggregate these results into a form that reveals the full extent of multipath effects at the core.

5.3 Attenuation Maps of the MeerKAT Core

The results presented in the preceding sections are limited in application since they investigated specific directions. These curves are actually 'slices' of a bigger picture which is now drawn together by an *attenuation map*. Attenuation maps provide an overview of the evolution of basic transmission loss or reference attenuation within a given radius of the horizontal (phi) plane. Hence, we gain aggregated insights regarding the electromagnetic characteristics of an environment as they relate to signal propagation. To this end, we applied our ray model (MoM-PO hybrid) to map the MeerKAT core at three frequencies, namely, 350, 1300 and 3050 MHz. These frequencies were selected to respectively represent the low, medium and high frequencies of the SKA mid-frequency band (350 to 3050 MHz). Transmitting and receiving at a height of 11 m, the fields were computed in concentric circles at an angular resolution of 2° in steps of 10 m from the array centre to a radius of 1000 m.

With the source at the centre of the array, basic transmission loss (L_b) and reference attenuation (A_{ref}) for a regular half-space are presented as attenuation maps in Figure 5.11. For reference, the relative locations of the 44 MeerKAT receptors are depicted by magenta dots. Acquaintance with these maps is necessary in order to better conceive the results for the MeerKAT core.

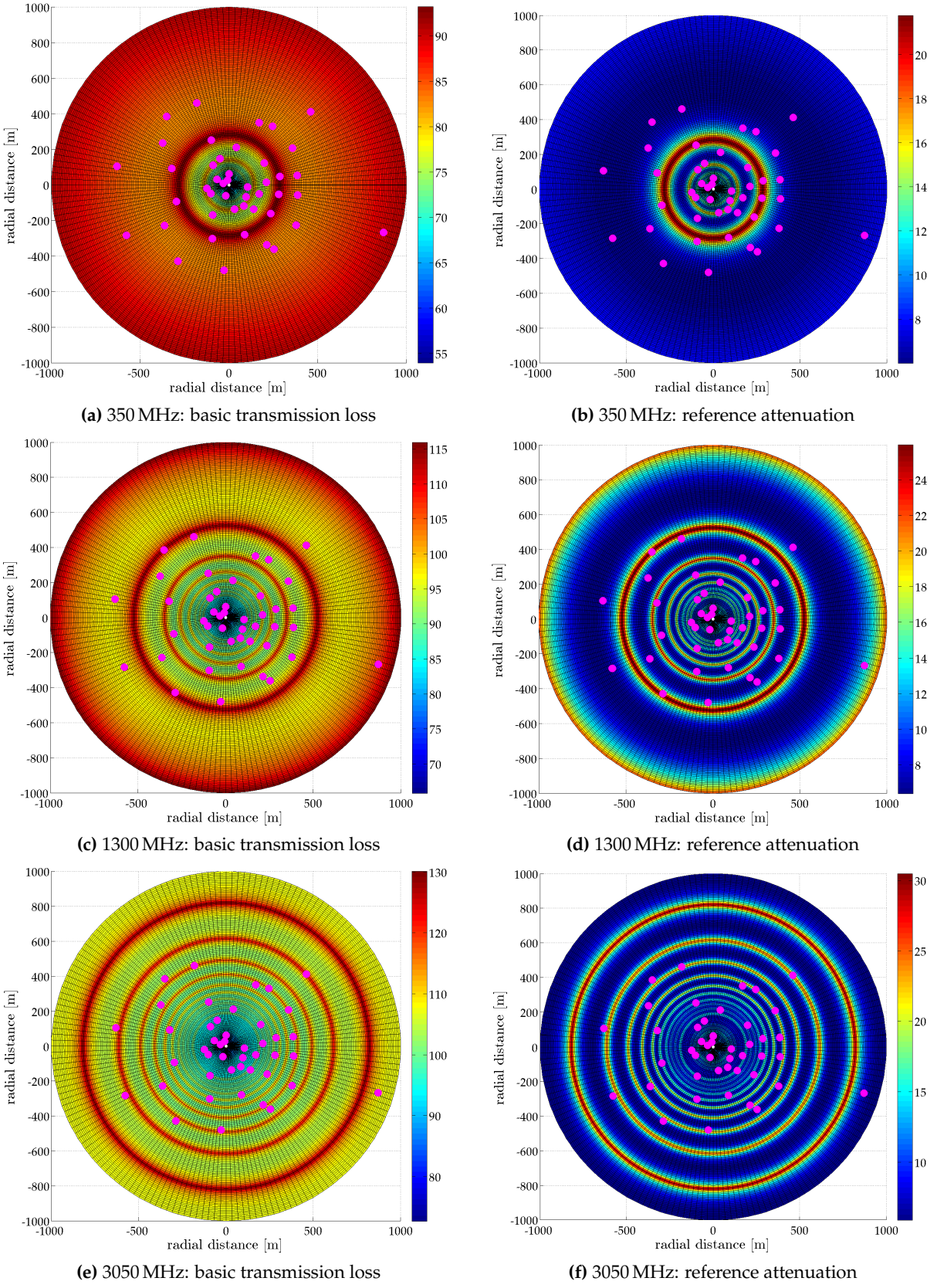

(a) 350 MHz: basic transmission loss

(b) 350 MHz: reference attenuation

(c) 1300 MHz: basic transmission loss

(d) 1300 MHz: reference attenuation

(e) 3050 MHz: basic transmission loss

(f) 3050 MHz: reference attenuation

Figure 5.11: Attenuation maps for a regular half-space. The magenta dots represent the locations of MeerKAT receptors relative to the centre of the array.

The thinner, higher loss bands correspond to cancellation of the fields as a result of ground

bounce. Due to smaller radio path length differences, fading is more severe at 1300 and 3050 MHz as can be seen by the number of concentric rings. For all three frequencies, A_{ref} is at the least 6 dB higher than the free space loss.

Commencing with the receptors in orientation 1 (facing southwest), Figure 5.12 shows the maps corresponding to 350 MHz. Although there is still an appearance of cancellation, the evolution of loss is vastly different from the regular half-space. At a radial distance of 290 m to the west, L_b for MeerKAT is 88 dB while the same location for a regular half-space shows 93 dB. That is, there is an increase of 5 dB. Of course there are also regions where the attenuation is higher than that of the reference case. In terms of A_{ref}, the worst case scenario is 2 dB higher than FSL.

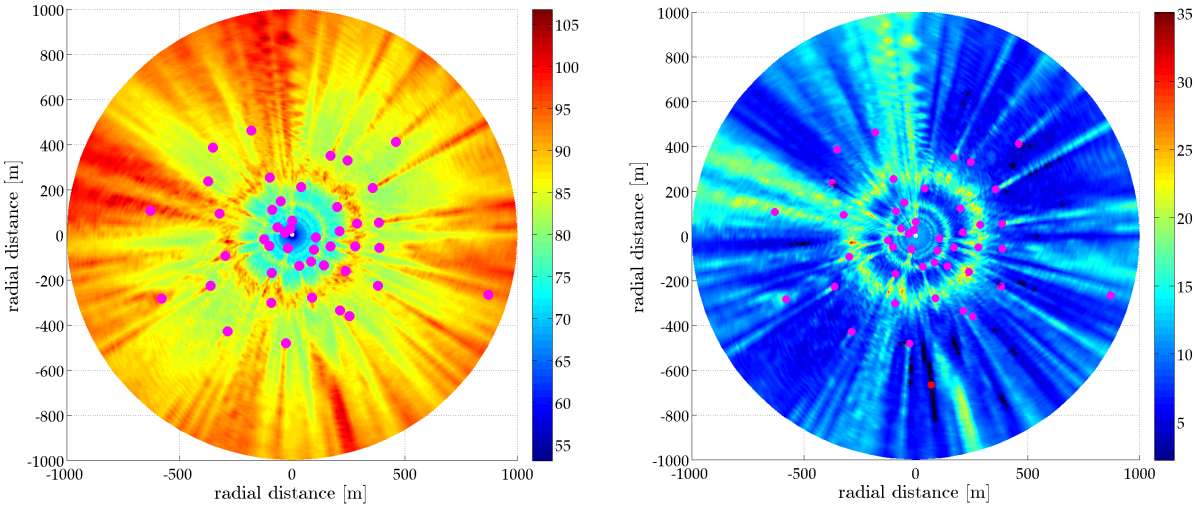

(a) basic transmission loss **(b)** reference attenuation

Figure 5.12: Attenuation map for orientation 1 at 350 MHz. Asterisks denote the relative high risk regions of ≤ 4 dB in (b).

It is more clear at 1300 MHz that shadowed regions are set up behind the dishes. This is seen as the high loss streaks most pronounced beyond a radius of 500 m in Figure 5.13a. Closer to the core, L_b is again 5-6 dB lower in the regions that correspond to high loss in the regular half-space, showing the general increase in the received field. A new, interesting phenomenon of pockets or patches of low loss manifests in A_{ref} for the core (Figure 5.13b). In fact, A_{ref} approaches and is less than zero at some locations. In particular, the radial arms in the north-northwest (NNW), west-northwest (WNW) and southeast (SE) directions are all low loss regions where A_{ref} frequently approaches 0 dB.

Basic transmission loss at 3050 MHz evolves in an even more dramatic fashion than observed at 1300 MHz. Again the locations where high loss occurs (due to cancellation) in the regular half-space (Figure 5.11e) exhibit lower loss in the corresponding map for MeerKAT (Figure 5.14a). Within the central area there are locations where L_b reduces by as much as 14 dB. It is not surprising then that the corresponding A_{ref} in Figure 5.14b is considerably lower with a startling -10 dB for the minimum value. This occurs in the NNW direction at a radius of 240 m, close to

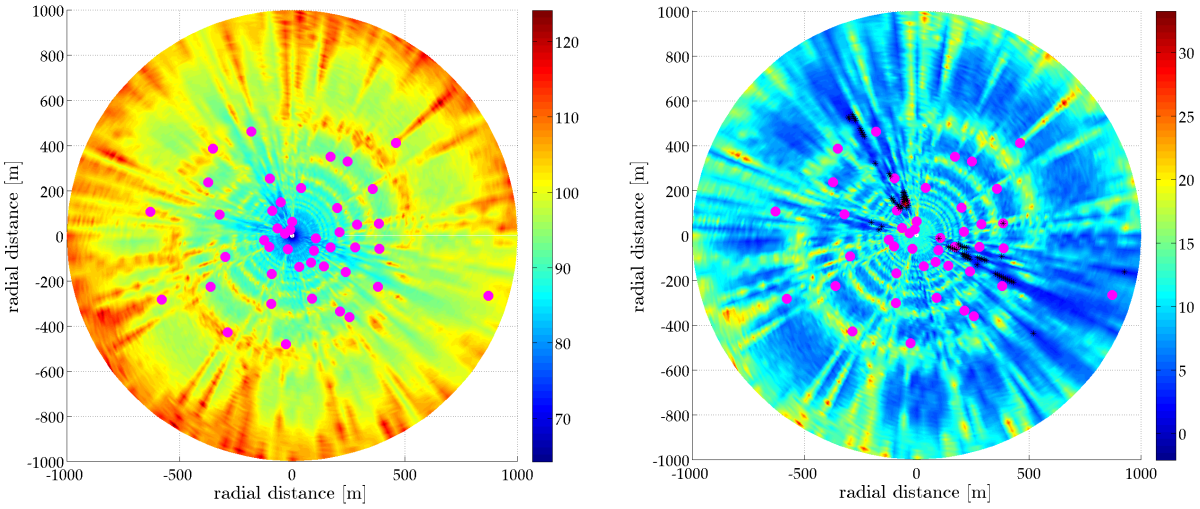

(a) basic transmission loss **(b)** reference attenuation

Figure 5.13: Attenuation map for orientation 1 at 1300 MHz. Relative high risk regions of ≤ 2 dB are represented by the asterisks in (b).

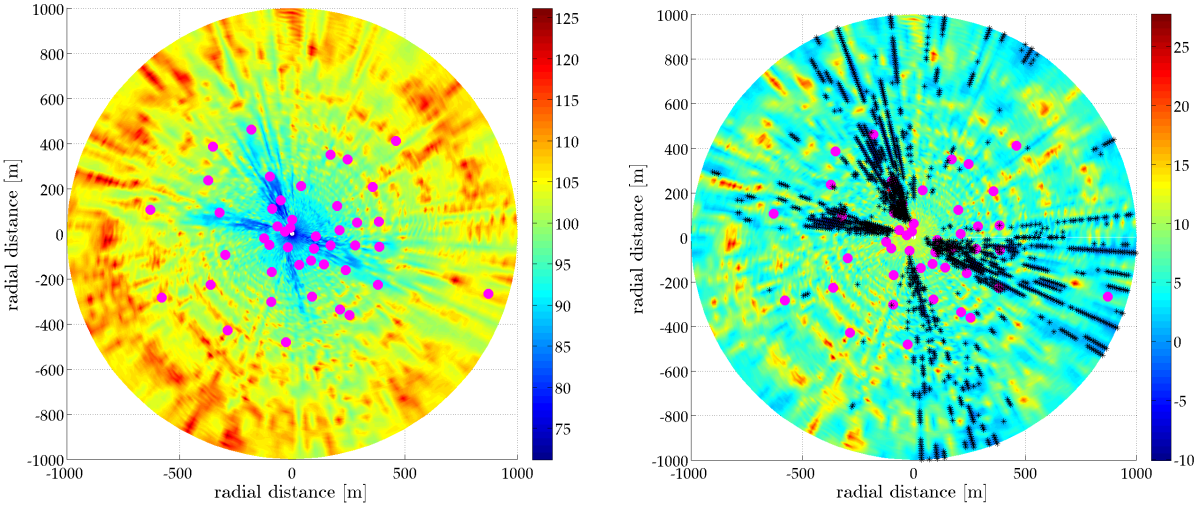

(a) basic transmission loss **(b)** reference attenuation

Figure 5.14: Attenuation map for orientation 1 at 3050 MHz with relative high risk regions of ≤ 1 dB shown by the asterisks in (b).

a receptor. Radial arms in the WNW, SE and south-southeast (SSE) directions are also characterised by low values of A_{ref}, frequently less than FSL (< 0 dB) at multiple locations.

Attenuation maps were also generated for the MeerKAT receptors in orientation 2 (facing northeast) and can be found in Appendix D (Figures D.3 to D.5). General observations do not differ much from what has been mentioned here, with the regular half-space trends being interrupted by streaks and sectors of high and low loss. Nevertheless, it is clear that receptor orientation will influence severity and location of high risk (low loss) regions. For instance, at 350 MHz the low loss regions are typically characterised by values of A_{ref} in the 2-4 dB range but record a minimum of 0.2 dB at a radial distance of 440 m northwest. In contrast, the minimum value at 350 MHz for orientation 1 is 2.2 dB, occurring at a radial distance of 670 m to the

south. Additionally, there are relatively more high risk regions for orientation 2 than orientation 1 at 350 MHz.

Relative high risk regions are highlighted by the asterisks in Figures 5.12b, 5.13b and 5.14a for orientation 1, and Figures D.3b, D.4b and D.5b for orientation 2. The risk thresholds were determined based on examination of the data by sight as well as a desire to easily distinguish the lower loss regions from the relatively higher loss locations.

Undoubtedly, the greatest potential danger lies at high frequencies as seen from the maps at 3050 MHz) where many regions with $A_{\text{ref}} < 1$ dB occurred for both orientations 1 and 2. This is not surprising since multipath effects are most severe when path length differences are small. In spite of there being dramatic effects at 350 and 1300 MHz, the multipath does not yield terribly severe consequences with regard to A_{ref}. This is most likely due to a localisation of effects as a function of frequency and dish orientation. At 350 MHz, there are relatively more risk regions for orientation 2 than orientation 1 given the same threshold of ≤ 4 dB. Conversely, for a threshold of ≤ 2 dB, fewer risk locations were identified for orientation 2 than 1. Furthermore, two regions were found with A_{ref} less than FSL for orientation 1 and none for orientation 2 (where the minimum attenuation was 0.1 dB).

5.4 Derivation of Path Loss Exponent

The numeric data is now used to compute the path loss exponent, n, for propagation through the MeerKAT core. This will enable empirical modelling using the log distance formula [38, 51]

$$L_b = L_{b0} + 10n \log\left(\frac{d}{d_0}\right) \tag{5.1}$$

where L_{b0} is the basic transmission loss at the reference distance d_0. Equation (5.1) typically includes a normally distributed random variable to account for fading. This is not essential here since characterisation of the fading does not add real value to RFI protection. Furthermore, due to the fact that the computation is based on data from the actual multipath environment itself, the empirical curve will represent the underlying mean trend. This makes obsolete the inclusion of a random variable (which would only skew the transmission loss curve by a certain factor).

The path loss exponent is related to basic transmission through [51]

$$d^n = k\, l_b \tag{5.2}$$

where l_b is the basic transmission loss in linear terms and $k = (\lambda/4\pi)^2 = (c/4\pi f)^2$ is the free space factor. Solving for n gives

$$n = \frac{\log(k l_b)}{\log(d)} = \frac{\log(k) + (L_b/10)}{\log(d)}\,. \tag{5.3}$$

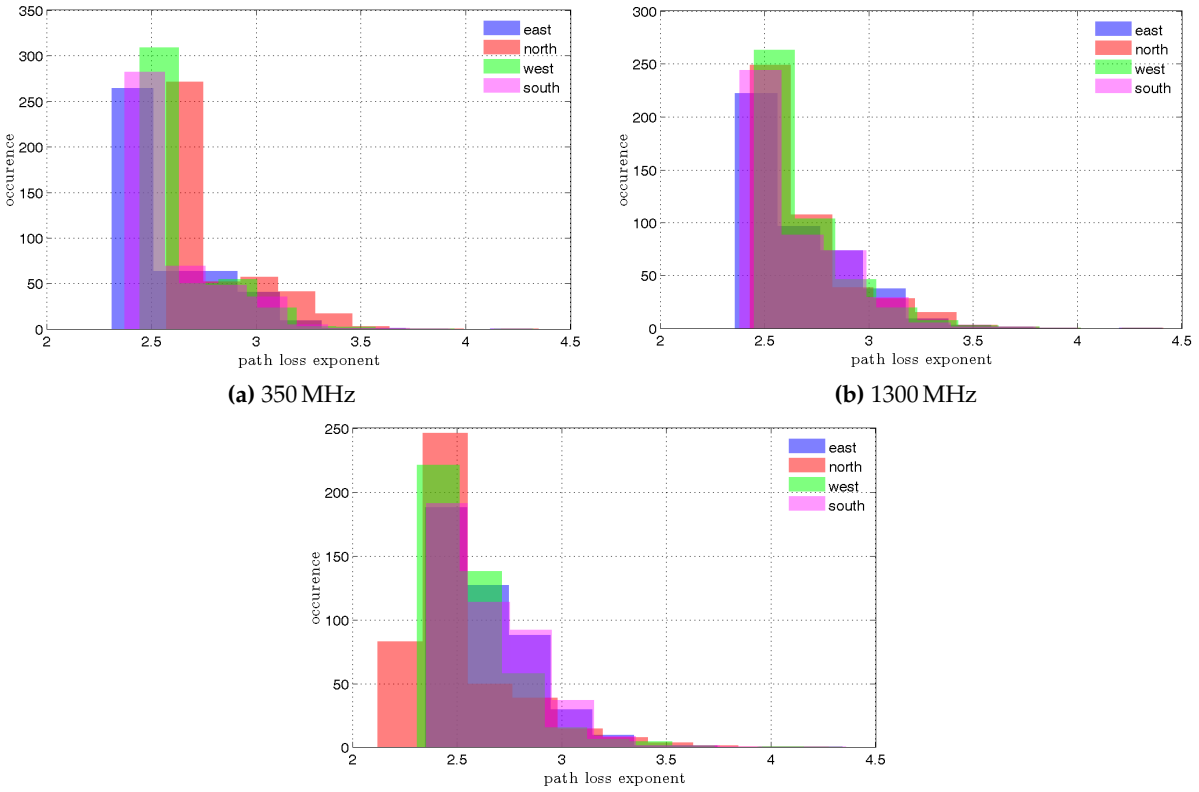

(a) 350 MHz

(b) 1300 MHz

(c) 3050 MHz

Figure 5.15: Distribution of path loss exponent (n) in the case of a directional source and MeerKAT receptors in orientation 1.

With the data in Sections 5.2.2 and 5.2.3 as input, path loss exponents were computed using (5.3).

Histogram plots of the path loss exponents computed for each dataset are shown in Figures 5.15 and 5.16 corresponding to directional and omni-directional sources, respectively. (Corresponding results for the receptors in orientation 2 are in Appendix D.3.) These charts reiterate the fact that the MeerKAT environment is complex. The path loss exponent exhibits a range of values that correspond to different types of radio environments. To obtain the most representative value, for each frequency the median value of the path loss exponent in each direction was computed. These median values were then used to compute the mean. The results are summarised in Table 5.1.

The results in Table 5.1 again point out the potential impact of dish orientation on signal loss. This can be seen clearly in the case of a directional source where a slightly higher exponent was obtained consistently for orientation 1. However, the values at 3050 MHz are comparable, suggesting that orientation may not be very crucial at high frequencies.

The lower path loss exponents obtained for an omni-directional source are the preferred values since they will yield conservative results under the presumption of the worst case multipath effects. Hence, the overall path loss exponents should thus be taken as 2.34, 2.30 and 2.19 corresponding the low, mid and high frequencies of the SKA midband.

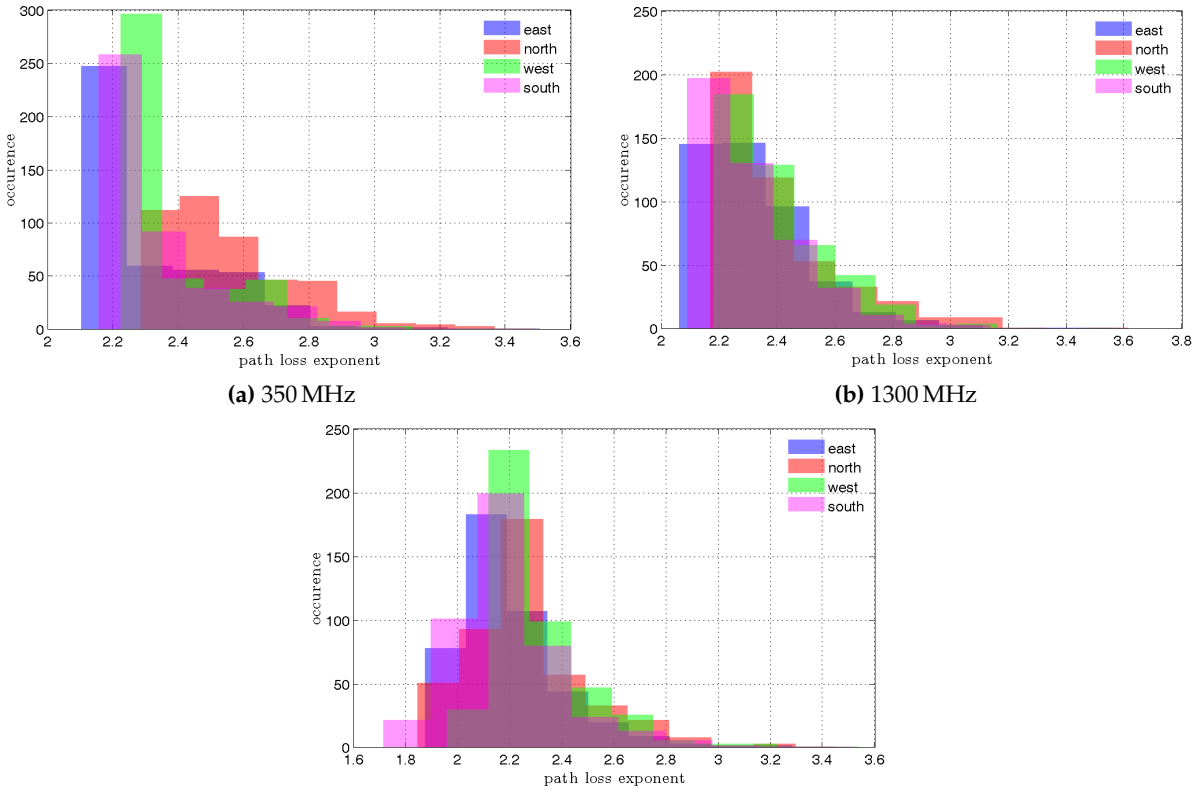

(a) 350 MHz

(b) 1300 MHz

(c) 3050 MHz

Figure 5.16: Distribution of path loss exponent (n) in the case of a omni-directional source and MeerKAT receptors in orientation 1.

Table 5.1: Path loss exponents for MeerKAT

freq	directional source		omni-directional source	
[MHz]	orientation 1	orientation 2	orientation 1	orientation 2
350	2.53	2.43	2.32	2.35
1300	2.55	2.34	2.32	2.28
3050	2.50	2.48	2.20	2.18

5.5 Summary

The goal of this chapter and indeed the primary objective of this research has been to model signal propagation through the MeerKAT core and thereby characterise it. This has successfully been achieved and is summarised by attenuation maps in which high risk (low loss) regions are easily identified. These maps can reveal potential problem areas and can serve as a guide for prioritising which regions to consider during RFI audit surveys.

It is clear from this investigation that the most severe effects due to multipath will occur at the higher frequencies. However, it is not to be assumed that there is no risk at the lower frequencies: adverse effects (zero reference attenuation) were observed even at 350 MHz. Additionally, the evolution of transmission loss through the core might worsen at a certain frequency depending on the dish orientation and the height at which the source signal originates.

As a radio environment, the MeerKAT core is characterised by path loss exponents of 2.34, 2.30 and 2.19 corresponding the low, mid and high frequencies of the SKA midband. These values show that the nature of multipath in the core results in a relatively low loss environment in which basic transmission loss will be comparable to free space loss for which the exponent is 2.

The numerical modelling undertaken here is no small feat. Our simulations involved a total of 3 781 200 triangles for the 44 receptors, requiring 5 710 609 basis functions. For a memory of 21.87 GB spread over 12 cores, it took 28.42 h to generate results at 3050 MHz. Nonetheless, the return in insights and information gained through the numeric data far more than compensate for the computational cost. It would be extremely problematic to map the MeerKAT core any other way at the spatial resolution achieved here. And herein lies our novelty: we have devised a deterministic model such that the full scale, three-dimensional propagation environment of MeerKAT has been reproduced with promising accuracy.

Chapter 6

Conclusions and Recommendations

The scope of the research was introduced in Chapter 1 with a brief discussion on the MeerKAT environment and the need for prediction tools for RFI monitoring. Naturally, this led to a review of the core principles of propagation studies in Chapter 2. A few propagation models were discussed, with emphasis on those that have frequently been used for studies in the Karoo. This was concluded with an overview on deterministic methods. In Chapter 3, selected empirical models were evaluated against measured data to determine their accuracy for modelling the MeerKAT site. It was evident from the evaluation that a more accurate tool would be required for analysis of the MeerKAT core. Hence, Chapter 4 focused attention on developing a deterministic model. A ray model was realised and validated by comparison to measurements at KAT-7. Using the verified ray model, the MeerKAT core was characterised in Chapter 5.

6.1 Summary of the Research

The focus of this research was on propagation modelling as a means of characterising the electromagnetic environment of MeerKAT. Propagation modelling aims to predict signal degradation (transmission loss) with regard to interference effects – which depend on the environment – and thereby provide grounds for selecting potential mitigation methods. Consideration of the site layout, purpose (RFI protection), range and the impact of various mechanisms on signal propagation led to an emphasis on reflection. Agreement between measurements and simulation confirmed that even over irregular terrain, reflection is the dominant effect.

ITU Recommendation P.1546, the Longley-Rice Irregular Terrain Model (ITM) and the Egli model were for the first time evaluated to assess their accuracy and suitability for predictions in the Karoo. The measured data comprised two datasets (DS1 and DS2) corresponding to transmitter heights of 5 and 7.5 m, respectively, while the receiver was fixed at 2 m. For each dataset, three short range (< 1 km) and two long range (> 1 km) recordings were made. On account of large errors tending towards over-prediction of loss, the Egli model was found to be unsuitable for modelling the MeerKAT environment within the parameter space of the measurements. Very good predictions were obtained at some path lengths but the performance was not consistent (see Tables 3.2 and 3.3). On the other hand, P.1546 and ITM models gave reliable estimates. Their respective root mean square errors (RMSE's) averaged over the two datasets were 7.43 and 6.58 dB. This is well within the 15 dB error margin prescribed for rural areas. Thus, although P.1546 and the ITM are conservative, their application (to similar parameter spaces) will not compromise RFI shielding budget calculations, for instance. However, it could lead to RFI protection measures being more stringent than required.

Contrary to the popular presumption, it was clearly seen that propagation loss does not triv-

ially reduce to free space loss (FSL) at short range. On average, a 14 dB difference between FSL and open area measurements (dataset-3, DS3) was recorded at five path lengths between 20 and 200 m. Evidently, careful consideration must be given to the physical configuration (path length, antenna heights) before the FSL approximation is applied. In relation to RFI protection, this is not necessarily problematic (for the radio observatory) but will typically lead to even more conservative measures than if empirical models are used. In fact, the proper way to regard FSL predictions is as the benchmark defining the worst case scenario whereby propagation loss is at a minimum.

Recognizing the limitations of empirical path loss modelling in the failure to accurately model real ground, inability to incorporate scattering phenomena and inadequacy in representing underlying physical processes, attention was turned towards deterministic modelling. Utilising the commercial computational electromagnetics (CEM) software, FEKO, a full wave propagation model (FWPM) was developed using the method of moments (MoM). A comparison of the FWPM basic transmission loss predictions to Karoo measurements (DS1 and DS2) yielded an unprecedented RMSE of < 4 dB. Ultimately, a ray model exploiting the MoM and physical optics (PO) was synthesised. Its features include: accounting for the electrical properties of the ground as a function of frequency; antenna radiation characteristics are incorporated; scattering from multiple objects can simultaneously and efficiently be modelled; modelling occurs in a three-dimensional environment such that multipath effects are inherently taken into account. Validation of the ray model was done via comparison to measurements at KAT-7 (dataset-4, DS4). From this analysis, a RMSE of 3.68 dB was obtained.
Although it has a high computer memory requirement, the novelty and significance of this deterministic, ray model is the ability to reproduce an actual deployment scenario with precision and high accuracy. In fact, development of the model was motivated by the need to characterise the MeerKAT core. Full scale simulations of 44 MeerKAT receptors within a 1 km radius of the array centre were run successfully and yielded attenuation maps for the area. Mapping of the core exposed the full extent of electromagnetic complexity and the necessity for deterministic modelling. Most notably, the attenuation maps revealed the regions of high sensitivity (low loss), presenting new information that could prove invaluable in identifying potential problem areas. Considering the restrictions against measurements close to MeerKAT dishes, the ray model becomes extremely attractive and essential. At any rate, high spatial resolution data of the sort presented here would be extremely cumbersome to obtain physically.

In sum, the PhD ascertained the inadequacy of standard empirical modelling to predict attenuation in the Karoo environment. This gap was bridged by developing a site-specific, deterministic propagation model with an unprecedented level of accuracy as proven by comparisons to measurements. It was revealed that there exists a complex multipath environment in which electromagnetic (EM) noise could escalate. Indeed, some high risk (low loss) regions were identified. Based on the simulations, path loss exponents of 2.34, 2.30 and 2.19 were obtained, corresponding respectively to 350, 1300 and 3050 MHz (representing the low, medium and high frequencies of the SKA midband). This provides a means of empirically modelling propagation through the MeerKAT core for quick assessments. The techniques established here can readily

be applied to evaluate the EM response of any complex environment defined by scattering.

6.2 Limitations

6.2.1 Simulation Constraints

A major limitation of the ray model as applied to the MeerKAT core is the need for high computational power. Even meshing might terribly slow down an average machine of specifications similar to 12 GB memory (RAM) and 4 cores equipped with multi-threading. As such, the local Stellenbosch University computer cluster, HPC1 (also know as Rhasatsha), was used to run all simulations involving dishes. In the case where the HPC1 job scheduler determines the computer resources, 24.65 GB of memory and 27.31 h were required to simulate the MeerKAT core at 3050 MHz. For the 44 receptors, this translated to $\sim 3.7 \times 10^6$ metallic triangles.

A check for convergence of the numeric data was not performed. This is because of incompatibility of certain solvers and the high memory requirements of others. For instance, the uniform theory of diffraction (UTD) solver and PO – which is ideal for structures such as dishes – cannot be used in the same model. At present, it would thus not be possible to model the MeerKAT core with a real finite ground plane. A MoM-UTD or UTD-only solution will give errors since the UTD is not designed for modelling structures such as dishes that have fine detail. Memory requirements of methods such as geometrical optics and the multilevel fast multipole method (MLFMM), scale up rapidly and cause the program to terminate. On the other hand, the PO solver which is optimal for the problem of dish scattering, uses a pre-defined mesh that cannot be adjusted. Hence, verification of the ray model depended entirely on comparison to measurements at KAT-7.

6.2.2 Limitations of the Measurements

For all the measured datasets used in this research, antenna heights were low (< 10 m). Ideally, some measurements ought to have been conducted around the height of the MeerKAT receivers (11 m). Thus, even though there was excellent agreement between measurement and simulation, there exists some uncertainty regarding the applicability of the numerical modelling for higher antenna heights.

Any given measurement is a sample around the true value and this sample will contain errors due to the measurement process itself. As much as possible, care was taken to use dedicated, high quality cables and connectors that were periodically tested for damage. Thus, uncertainty in the measured datasets can be attributed to systematic errors in the equipment (antennas, signal generators and spectrum analysers) and random error in marking out distances as well as aligning the antennas. The uncertainty could have been quantified and minimised by repeating each measurement setup several times so that the best estimate is given by the average value.
Time constraints and measurement costs did not permit multiple data recordings for each physical configuration. Consequently, the uncertainty in the measurements reported here is largely

unknown. Nonetheless, the agreement between the four datasets and the numerical modelling provides some positive feedback on the validity of both measurement and simulation.

6.3 Future Work

In the bid to effectively manage electromagnetic interference (EMI) and mitigate radio frequency interference (RFI) in the Karoo, studies on and relating to electromagnetic compatibility (EMC) are a key component. In light of this and what has been achieved in this research, the following is recommended for future work:

- A rigorous measurement campaign at the actual MeerKAT core site. This would serve to further verify and refine the deterministic modelling.
- Investigate coupling mechanisms into the MeerKAT receptors. This would introduce questions such as the role, if any, of the non-main lobe of the telescopes in coupling and where the near-field/far-field transition point lies and what impact this could have.
- Integrate direction finding tools with deterministic modelling. This would involve aggregating the various RFI-related studies that have been conducted to achieve a monitoring tool such that an RFI source can be determined using the predicted environment and measured data.
- Refine irregular terrain and/or topography modelling to address diffraction. Exploiting the UTD real finite ground plane is a promising way to investigate diffraction in relation to EMI sources such as windmills. Also, there have been some divergent views within the SKA-SA on how diffraction is to be treated. Therefore, a deliberate study on this topic would be worthwhile. Topography modelling brings to the fore the prospect of large scale computational representation of a site. In addition to diffraction effects, the benefit of this would be investigation of multipath due to terrain.
- Capitalise on the ability to reproduce deployment scenarios to model other environments such as solar photovoltaic (PV) plants. Noise from PV plants is a potential EMI problem in the northern part of the MeerKAT site.

Appendices

Appendix A

Transmission Loss

Given a power input P_t' (dBW or dBm) at the antenna terminals of a radio frequency transmitting system, if P_r' (dBW or dBm) is the resulting power measured at the receiving antennas terminals, then system loss is defined as [29]

$$L_s = P_t' - P_r' \,. \tag{A.1}$$

In addition to effects introduced by the intervening medium, L_s, accounts for circuit losses in the transmitting and receiving antennas. These are respectively denoted as L_tc and L_rc. If the circuit losses are neglected system loss then becomes transmission loss (L), that is [29, 30]

$$L = L_s - L_tc - L_rc = P_t - P_r \,, \tag{A.2}$$

where P_t is power radiated by the transmitting antenna and P_r is the resultant power available at an equivalent loss-free antenna. It should be kept in mind that P_r incorporates the transmit and receive gains as well a loss L_m due to the intervening medium in addition to free space basic transmission loss, L_{bf} [28, 30]. To be precise,

$$P_r = P_t + G_t + G_r - L_{bf} - L_m \,, \tag{A.3}$$

so that

$$L = L_{bf} + L_m - G_t - G_r \,. \tag{A.4}$$

Computing the loss which would occur if isotropic antennas were used instead yields the *basic transmission loss*

$$L_b = L + G_t + G_r = L_{bf} + L_m \,. \tag{A.5}$$

As can be seen, if environmental effects are negligible, L_b reduces to L_{bf}.
More frequently, the term *path loss* is used in reference to (A.5) but this can be somewhat misleading. Path loss is defined as the ratio of power radiated to power received (p_t / p_r*) [38, 47, 48] which is actually the transmission loss given by (A.2). In implementation, however, it is (A.5) that is quoted. Rappaport [38] attempts to remedy this by replacing the transmitted power with effective isotropically radiated power (EIRP) in the definition of path loss but still uses the ratio p_t / p_r in the mathematical expression. Confusion is avoided and consistency achieved by simply stating that path loss is another term for basic transmission loss. This is in keeping with the loss term in the link budget expression (A.3).

*Small letters denote numeric values

Appendix B

FEKO Modelling

B.1 Equivalent Sources

Use of equivalent sources (including ideal receiving antennas) greatly speeds up the solution time of a problem. When generating far-field data for use as an equivalent source, 'continuous sampling' should be selected so that the resulting pattern can be used at any angle. Care should be taken to ensure that the frequency range of the far-field pattern coincides with the solution frequency of the model to solved. If not, FEKO should be pointed to the correct line from which to start reading using the 'start from point number' field far-field data dialogue (see page 3-20, [91]).
If the line of sight path coincides with the x-axis, the U and V vectors of the ideal receiver must be set to -1 obtain the correct orientation. Similar adjustments can be made for other positions.

B.2 Common Errors Related to PO and GO

It may seem desirable to model dielectrics using geometrical and physical optics techniques. Here are some challenges one may encounter:

- *ERROR 38024: Large element PO not supported for dielectric PO triangles*
- *ERROR 33214: Not enough memory available for dynamic allocation*
  This occurs using ray-launching geometrical optics (RL-GO).
  This is likely to occur at high frequency, resulting in small ray-launching angles and therefore more Huygens sources to solve and more memory.
  Suggestions:
  1) Memory increases with the number of parallel processes. First try maybe 4 and work from there.
  2) Try the "Low" setting for convergence accuracy for the RL-GO
- *ERROR 33714: An infinite ground plane and RL-GO are not allowed simultaneously*
- LE-PO and RL-GO cannot be used in the same model
- *ERROR 240: A triangle is too small or EPSENT is too large*
  This error was encountered for simulations involving dishes solved with LE-PO . It is associated with the geometry limits (EG Card)
  *The triangle with the number 9074 is too small (surface = 1.6260E-11 m*m) compared with the limit value EPSENT= 1.0000E-06 m. Define the parameter EPSENT at the EG card.*
  To solve the issue, change the geometry limits of EG Card using EditFEKO

B.3 Running on HPC

Exit Code 9 may occur when there are too many memory-unlimited FEKO processes on one machine resulting in processes running out of memory. (c.f. Charl Moller) This can be overcome by specifying:

```
#PBS -l select=1:ncpus=10:mpiprocs=10:scratch=true:mem=400GB
# request 400GB RAM, 40GB per process export FEKO_MAXALLOCM=$((400*1024))
runfeko dipole_finite_gp_1300MHz_v2.cfx --use-job-scheduler
```

B.4 Topography Surface

Taking advantage of the UTD technique for treating finite ground planes, we devised a method for incorporating terrain data into FEKO. The appeal in pursuing such functionality relates to the need to investigate multipath effects due to terrain.
A 30 m resolution digital elevation model (DEM) based on the Shuttle Radar Topography Mission (SRTM) data was cropped to the desired area around the Losberg hill using the open source software QGIS.

1) Method 1
   Read the cropped Geotiff file into MATLAB and subsequently export it as a stereolithography (*.stl) file. The *.stl file can then imported into FEKO as 'Mesh'. This approach cannot utilize the UTD solver which was found to be the best for finite ground planes involving thin dielectric layers.
2) Method 2
   Export the DEM data as a geometry layer in `*.dxf` format and subsequently import it into FEKO as a CAD part. This splits the topography surface into discrete faces which can be unioned. Face properties can then be set to correspond to real ground by applying a dielectric layer as described for the UTD-treated ground plane.

Appendix C

Matlab Scripts

C.1 Launching FEKO Simulations with Matlab

```
% Script to run FEKO propagation models within the MATLAB environment.
% Relies on two scripts by Ngoy Mutonkole:
%               feko_engine (2014)
%               main_sim_engine (2014)
%
% Temwani-Joshua, Sept 2015, Stellenbosch University

close all
clear all
clc

% matlabpool

% dipole sims
cd('F:\FEKO Models\Path_Loss\dipole_ground_plane')
% lpda sims
% cd('F:\FEKO Models\Path_Loss\lpda\lpda_ground_plane')
% cd('F:\FEKO Models\Path_Loss\lpda\hockey')

% File handling settings
cur_num = 1;

% Path to source(where the CADFEKO file is) and destination directories
% drive = 'F:\FEKO Models\Path_Loss\path_loss_models\plm_dipole';
Data.source_dir = [pwd '\'];
% for .ffe files || dipole_gp_reflect_ffe, lpda_hockey_ffe
Data.ff_dir = [Data.source_dir 'dipole_gp_pec_ffe\'];
% Data.sph_dir = [Data.source_dir 'dipole_vsph\']; % for .sph files
% for .s2p files || dipole_gp_reflect_sp, lpda_hockey_sp
Data.sp_dir = [Data.source_dir 'dipole_gp_pec_sp\'];
% matched refers to dipole design
mkdir(Data.ff_dir);
% mkdir(Data.sph_dir);
mkdir(Data.sp_dir);

% CADFEKO file name: dipole3, dipole_gp_exact_sommer, lpda_hockey
Data.filename = 'dipole_gp_pec';
name = [Data.filename,'_run_'];
% Source files of interest to be copied and saved: far-field file and
% f_source = [Data.source_dir,Data.filename,ff_xt];

Data.feko_file = [Data.filename,'.cfx']; % CADFEKO file to execute, might need full path
```

```
time_elapsed = []; % Record simulation time
% load validation_points.mat;
% d = [50 200 700 1800 3600]; % path length in metres
d = [20 50 100 150 200]; % path length in metres for HockeyField Campaign
% freq = [100:50:2500]*1e6;
% s = s_val;
for k = cur_num:length(d)
    s = d(k); %[s(k) 10 10];
    tic;
%     x = [s, 7.5];
    [cur_num] = feko_engine(s,cur_num,Data);
    time_elapsed = [time_elapsed toc];
end

% extract S-parameters and save to matlab directory
sp_files = dir(Data.sp_dir);
S_params = {};
S_temp = [];
numfiles = size(sp_files,1);
for j = 3:numfiles
    i = j-2;
    filename = sp_files(j).name;
    disp(filename)
    u = fopen([Data.sp_dir filename],'r');
    while ~feof(u)
        line = fgetl(u); %read line
        if ~ischar(line), break
        end %stop when no more lines available
        S_temp = [S_temp; str2num(line)]; %convert to number and add to matrix
    end
    S_temp2 = [double(S_temp(:,1)*1e-6) double(S_temp(:,2)) double(S_temp(:,4))...
        double(S_temp(:,6)) double(S_temp(:,8))];
    S_params{i} = S_temp2;
    S_temp = []; % clear S_temp for next run
    S_temp2 = [];
end

sp_locale = 'C:\Users\TJ\Documents\MATLAB\Matlab_Propagation\FEKO_Sims\S2P\';
% mkdir(save_locale);
% delete([sp_locale Data.filename '_s2p.mat']);
save([sp_locale Data.filename '_s2p'],'S_params');

% process and save gain/directivity data
ff_files = dir(Data.ff_dir);
num_ff_files = size(ff_files,1);
for j = 3:num_ff_files
    i = j-2;
    ff_filename = ff_files(j).name;
    disp(ff_filename)

    [theta,phi,Et,Ep,g,freq,psamples,tsamples] = farfield_read([Data.ff_dir ff_filename]);
```

```
    data.theta = theta;
    data.phi = phi;
    data.psamples = psamples;
    data.tsamples = tsamples;
    data.freq = freq;

%     Eph = max(Ep);
%     Eth = max(Et);
%     for k = 1:length(freq)
%         [dd(:,k), Pt(:,k)] = computeDirectivity(Et(:,k),Ep(:,k),data);
%     end
%     D(:,i) = max(dd)';
    G(:,i) = max(g)';% gain directly from FEKO which is in dB!
end
f = freq'*1e-6;

gain_locale = ['C:\Users\TJ\Documents\MATLAB\Matlab_Propagation\',...
    'FEKO_Sims\FEKO_Sims.Gain\'];
mkdir(gain_locale);
% delete([gain_locale Data.filename '_gain.mat']);
save([gain_locale Data.filename '_gain'],'f','G');

cd('C:\Users\TJ\Documents\MATLAB\')


%% FEKO Engine
%  Runs FEKO from Matlab
%  Input(s):
%     x       : Vector containing values of variables to be passed to Feko
%     cur_num : Current Number of function Evaluations. Needed for file
%       handling purposes.
%     Data    : Structure containing system information.
%  Output(s):
%     cur_num : See Input(s) section
%
%
%   nym 2013 -- modified 01/06/2014 - 20/05/2015 for Feko v7
%   TJ Phiri -- modified Aug 2015

function [cur_num] = feko_engine(x,cur_num,Data)
    % File extensions
    ff_xt = '.ffe';
    sp_xt = '.s2p';

    if cur_num < 10
        name = [Data.filename,'_run_0'];
    else
        name = [Data.filename,'_run_'];
    end

    % nym uses this if structure to control output names for multiple
```

```
    % simulations -- uncomment if needed.
%         if cur_num < 100
%             name = [Data.filename,'_run_s'];
%         else
%             name = [Data.filename,'_run_sp'];
%         end
%     end
%     name = [Data.filename,'_run_'];

    FEKOstring = ['cadfeko_batch ',Data.feko_file,' -#path_length=',...
        num2str(x)];
%     FEKOstring = ['cadfeko_batch ',Data.feko_file,' -#ant_height1=',...
%       num2str(x(1)),' -#ant_height2=',num2str(x(2)),...
%       ' -#path_length=',num2str(x(3))];

    % Only variable of interest at present is path length. More variables
    % can be added
    system(FEKOstring);
    disp(['--------- Feko solving run #',num2str(cur_num),'... --------']);
    prefekoString = ['prefeko ',Data.filename,' > output.txt'];
    runfekoString = ['runfeko ',Data.filename,' -np 4 > output.txt',...
        ' --parallel-authenticate localonly'];
    % -np 4, ' --parallel-authenticate localonly'
    system(prefekoString); % A status of zero indicates that the command
    % completed successfully
    system(runfekoString);

    % Move .ffe files
    ff_dest = [Data.ff_dir,name,num2str(cur_num),'_Farfield1',ff_xt];
    ff_source = [Data.source_dir,Data.filename,'_Farfield1',ff_xt];
    copyfile(ff_source,ff_dest,'f');
    ff_files = dir(ff_source);
    numfiles = size(ff_files,1);
    if numfiles ~= 0
        copyfile(ff_source,ff_dest,'f');
    elseif numfiles == 0
        disp(['------  no ff files, run #',num2str(cur_num),'... -----']);
    end


    %% Move .s2p files
    sp_dest = [Data.sp_dir,name,num2str(cur_num),sp_xt];
    sp_source = [Data.source_dir,Data.filename,'_SParameter1',sp_xt];
    % Edited to accomodate Feko v7 format
    sp_files = dir(sp_source);
    numfiles = size(sp_files,1);
    if numfiles ~= 0
        copyfile(sp_source,sp_dest,'f');
    elseif numfiles == 0
        disp(['------  no sp files, run #',num2str(cur_num),'... ------']);
    end
```

```
    cur_num = cur_num + 1;
end
```

C.2 Propagation Modelling Based on FEKO S-Parameters

```
% Code for plotting (basic) transmission loss from S Parameters derived
% from FEKO The S-parameter *.mat files are generated using the script
% 'feko_propagation.m' and the data are the absolute values.
% The path loss so obtained is then compared to free space and other models
% ------------------------------------------------------------------------
% Path loss computation:
%            S21_prime = sqrt( (S21.^2)./(1-S11.^2)*(1-S11.^2) );
%            path_loss = -20*log10(S21_prime) + 2*G;
%            where S21_prime = P_rad/P_rec is the corrected S21^2 parameter

close all; clear all; clc;

%% FWPM Data

% load s2p *.mat file
load('dipole_gp_reflections_s2p');
% load(s_parameters);
[m n] = size(S_params);

% load gain *.mat file extracted from *.ffe file
% If gain is not available as *.mat file, load the *.ffe using
% 'farfield_read':
%     ffe_file = '[filename including path]';
%     [theta,phi,Et,Ep,g,freq,psamples,tsamples] = farfield_read(ffe_file);
%     G  = max(g)';

load('dipole_gp_reflect_gain');
S21_prime = [];
f_s = S_params{1}(:,1)*1e-6; % f in MHz
% freq = freq'*1e-6;
for i = 1:n
    S11(:,i) = S_params{i}(:,2); S22(:,i) = S_params{i}(:,5);
    S21(:,i) = S_params{i}(:,3);
    S21_prime(:,i) = sqrt( ((1 - S11(:,i).^2).*(1 - S22(:,i).^2))...
        ./(S21(:,i).^2) ); % corrected S21 parameter
    if length(G) ~= length(S21_prime)
        G = interp1(f,G,f_s); % use 'freq' in place of 'f' if gain is
        % obtained from *.ffe file
    end

    Lbs(:,i) = 10*log10(S21_prime(:,i)) + 2*G; % basic transmission loss
end

d = d.*1e-03; % path legnth in km (d would ideally be a included in the
% s2p file)
for i = 1:length(d)
```

```
    friis(:,i) = fspl(d(i),f_s);
end

%% free space loss comparisons
% font = 0.8;   % set relative font size %% for use with ExportKDP
% rect = [200, 200, 850, 500];
for i = 1:length(d)
    figure
    plot(f_s(1:1:end),Lbs(1:1:end,i),'--r',...
        f_s(1:1:end),friis(1:1:end,i),'g','LineWidth',2)
    ylabel('path loss [dB]','FontSize',16,'FontName','Palatino')
    xlabel('Freq [MHz]','FontSize',16,'FontName','Palatino')
    set(gca,'FontSize',12)
    legend('FEKO','Friis')
%     ExportFigKDP(font,1) % custom script for scaling figures
%     H = gcf; %get figure handle
%     set(H,'position',rect); %set figure properties
end
```

C.3 Gain from Far-field Data

```
% Script for extracting gain from farfield (.ffe) FEKO files
% NOTE: FEKO writes gain in dB
% TJ 2016 based on nym 2012

function [freq,g] = gain_read(Filename)

fid = fopen(Filename,'r');  % Open farfield result file
InputText=textscan(fid,'%s',8,'delimiter','\n');  % Read strings delimited
% by a carriage return
block = 1;
Intro = fgetl(fid);
freq(block) = sscanf(Intro,'%*s %f');
InputText=textscan(fid,'%s',1,'delimiter','\n');
skip = fgetl(fid); % need this line when farfield origin is shifted
Intro = fgetl(fid);
tsamples = sscanf(Intro,'%*s %*s %*s %*s %f');
Intro = fgetl(fid);
psamples = sscanf(Intro,'%*s %*s %*s %*s %f');

measrows = tsamples * psamples;

InputText=textscan(fid,'%s',3,'delimiter','\n');

while ~feof(fid)
    InputData = textscan(fid, '%f %f %f %f %f %f %f %f %f',measrows);
    g(:,block) = InputData{9};      % total gain in dB

    InputText = textscan(fid,'%s',3,'delimiter','\n');  % Read strings
    %delimited by a carriage return.
```

```
    block =  block + 1;
    Intro = fgetl(fid);
    status = feof(fid);

    if (Intro(1) == '#')
        freq(block) = sscanf(Intro,'%*s %f');
        InputText=textscan(fid,'%s',7,'delimiter','\n'); % 7 when origin
        % is shifted, 6 otherwise
        if status == 1
            break;
        end
    end

end
fclose(fid);
```

C.4 Plotting Attenuation Maps

```
%% path loss mapping
% TJ Phiri, Jul 2016
% -------------------------------------------------------------------------
close all; clear all; clc

folder = ['F:\FEKO Models\CouplingInvestigations\MeerKAT_env\',...
    'meerkat_mapping2\3050_meerkat_orient2_mapping2\'];
filename = '3050_meerkat_orient2_mapping2_NearField1.efe';
[r,phi,E] = nearfield_mapping([folder,filename]);

control_folder = ['F:\FEKO Models\CouplingInvestigations\MeerKAT_env\',...
    'meerkat_mapping2\meerkat_mapping2_control\'];
G = gain_read2([control_folder,'3050_meerkat_mapping2_control',...
    '_FarField1.ffe']);

filename2 = '3050_meerkat_mapping2_fs_NearField1.efe';
[r,phi,E_fs] = nearfield_mapping([control_folder,filename2]);
G_fs = gain_read2([control_folder,... % free space gain
    '3050_meerkat_mapping2_fs_FarField1.ffe']);

E = 20*log10( E*1e6 ); % convert to dBuV/m
Lb = 2*G - E + 20*log10(3050) + 107.2;

E_fs = 20*log10( E_fs*1e6 );
Lbf = 2*G_fs - E_fs + 20*log10(3050) + 107.2;

Lb = Lb - Lbf; % reference attenuation

[X,Y] = pol2cart(phi*pi/180,r);
ant_locations = [-8 27 134; 1 63 134; -32 10 134; -66 32 134;...
    -124 -19 134; -102 -49 134; -18 -61 134; -90 -169 134;...
    -93 -302 134; 32 -137 134; 88 -279 134; 84 -118 134;...
    140 -135 134; 237 -160 134; 281 -52 134; 211 16 134; 288 49 134;...
```

```
    200 123 134; 106 -11 134; 171 -51 134; 97 -66 134; -296 -93 134;...
    -322 93 134; -373 236 134; -351 386 134; -182 462 134; -99 253 134;...
    41 212 134; -51 148 134; -89 111 134; 171 350 134; 247 330 134;...
    461 412 134; 358 207 134; 386 54 134; 388 -57 134; 380 -226 134;...
    213 -336 134; 254 -360 134; -27 -480 134; -287 -429 134;...
    -362 -227 134; -630 106 134; -578 -284 134; 872 -267 134];

font = 0.8;
rect = [200, 200, 850, 500];
figure,hold
atten_map = surf(X,Y,Lb); view(2); grid
set(atten_map,'EdgeColor','interp')%,shading flat
set(atten_map,'FaceColor','interp') % will result in removal of radius lines
% shading flat, shading interp, shading faceted
axis equal tight;
xlim([-1000 1000])
ylim([-1000 1000])
c = colorbar;
set(c,'Location','EastOutside')

%% add antenna locations
scatter3(ant_locations(:,1),ant_locations(:,2), ant_locations(:,3),...
    'mo','LineWidth',5,'MarkerFaceColor','m')
set(gca,'FontSize',20,'FontName','Palatino Linotype')
xlabel('radial distance [m]','FontSize',20),...
    ylabel('radial distance [m]','FontSize',20)

%% other plotting options:
% h = polar([0 2*pi], [min(min(r)) max(max(r))]); % set limits of polar plot
% delete(h)
% hold
% contour(X,Y,Lb,100)

% contour(X,Y,Lb,100),hold
% scatter(ant_locations(:,1),ant_locations(:,2), 'mo','LineWidth',10,...
%       'MarkerFaceColor','m')

% ExportFigKDP(font,1) % figure scaling script
% H = gcf; %get figure handle
% set(H,'position',rect); %set figure properties

%% determining the risk regions (benchmark taken as <= 1 dB)
% lowest value
[a b] = find(Lb==min(min(Lb)));
minimum = min(min(Lb));
scatter3(X(a,b),Y(a,b),135,'r*');
r = sqrt(X(a,b)^2+Y(a,b)^2);
% risk regions
[c d] = find(Lb<=1);
for k = 1:length(c)
    scatter3(X(c(k),d(k)),Y(c(k),d(k)),134,'k*');
end
```

The user-defined function 'nearfield_mapping' must be added to the working directory.

```
%% nearfield_mapping
% script for reading FEKO nearfield data (*.efe file) to give suitable
% output for attenuation mapping
%
% TJ Phiri, Aug 2016
% Adapted from a script by nym 2012
% ------------------------------------------------------------------------

function [r,phi,E] = nearfield_mapping(Filename)

fid = fopen(Filename,'r');  % Open farfield result file
InputText=textscan(fid,'%s',8,'delimiter','\n');  % Read strings delimited
% by a carriage return
block = 1;
Intro = fgetl(fid);
freq(block) = sscanf(Intro,'%*s %f');
InputText=textscan(fid,'%s',1,'delimiter','\n');
skip = fgetl(fid); % need this line when origin is shifted
Intro = fgetl(fid);
rsamples = sscanf(Intro,'%*s %*s %*s %*s %f');
Intro = fgetl(fid);
tsamples = sscanf(Intro,'%*s %*s %*s %*s %f');
Intro = fgetl(fid);
psamples = sscanf(Intro,'%*s %*s %*s %*s %f');

measrows = rsamples * psamples;

InputText=textscan(fid,'%s',3,'delimiter','\n');

for k = 1:psamples
    InputData = textscan(fid, '%f %f %f %f %f %f %f %f %f',rsamples);
    r(:,k) = InputData{1};  % x samples (distance coordinate)
    theta(:,k) = InputData{2};    %
    phi(:,k) = InputData{3}; % height coordinate
    Er(:,k) = InputData{4} + 1j*InputData{5}; % x-component of E-field
    Eth(:,k) = InputData{6} + 1j*InputData{7}; % y-component of E-field
    Eph(:,k) = InputData{8} + 1j*InputData{9}; % z-component of E-field
    E(:,k) = sqrt( abs(Er(:,k)).^2 + abs(Eth(:,k)).^2 + abs(Eph(:,k)).^2 );
end
fclose(fid);
```

C.5 Generating Topography Surfaces

Running 'raster_to_3D' requires DXFLib Version 0.9.1 to export the topography surface as `*.dxf` format.

```
% raster_to_3D
% script for reading Geotiff files into Matlab and exporting them as
% topography surfaces
```

```
%
% TJ Phiri, June 2016
% -------------------------------------------------------------------------
close all; clear all; clc

karoo = ['F:\Academics\Propagation.Terrain.Profiles\',...
    'KAT7_SRTM_2016-07-04.tif']; % directory where geotiff file is located.
    % file must have been cropped to desired region (very large files will
    % cause problems when importing into FEKO)

[Z,R] = geotiffread(karoo);
Z = double(Z);

% extract and define x- and y-dimensions as longitude and latitude
% respectively
Lon = [R.Lonlim(1):R.DeltaLon:R.Lonlim(2)]';
Lat = [R.Latlim(2):R.DeltaLat:R.Latlim(1)]';

% covert lon and lat to ranges in metres

height = pos2dist(Lat(1),Lon(1),Lat(end),Lon(1),1)*1000;
H = flipud( double( [0:length(Lat)-1] * ( height/(length(Lat)-1) ) )' );

width = pos2dist(Lat(end),Lon(1),Lat(end),Lon(end),1)*1000;
W = double([0:length(Lon)-1]*(width/(length(Lon)-1) ))';

Z = Z - min(min(Z)); % normalise altitude
centre = [width/2 height/2]; % compute centre for use in FEKO

figure,mesh(W,H,Z)

% surf2stl(['F:\Academics\Propagation.Terrain.Profiles\MeerKAT_3D\',...
    %'KAT7_SRTM_2016-07-04.stl',W,H,Z]) % uncomment if desring topography
    % surface in *.stl format

FID = dxf_open('F:\FEKO Models\MeerKAT_topo_surface\kat7_area.dxf');
FID = dxf_set(FID,'Layer',10);
fvc = surf2patch(W,H,Z,'triangles');
dxf_polymesh(FID, fvc.vertices, fvc.faces);
dxf_close(FID);
```

Appendix D

Supplementary Transmission Loss Data

D.1 Reference Attenuation as a Function of Distance Analysis: Directional Source

The data here correspond to Section 5.2.2 where reference attenuation is examined as a function of distance. The height of the source was 5 m while the received electric field was computed at a height of 11 m. As can be seen in Figures D.1 and D.2, the reference attenuation (A_{ref}) generally

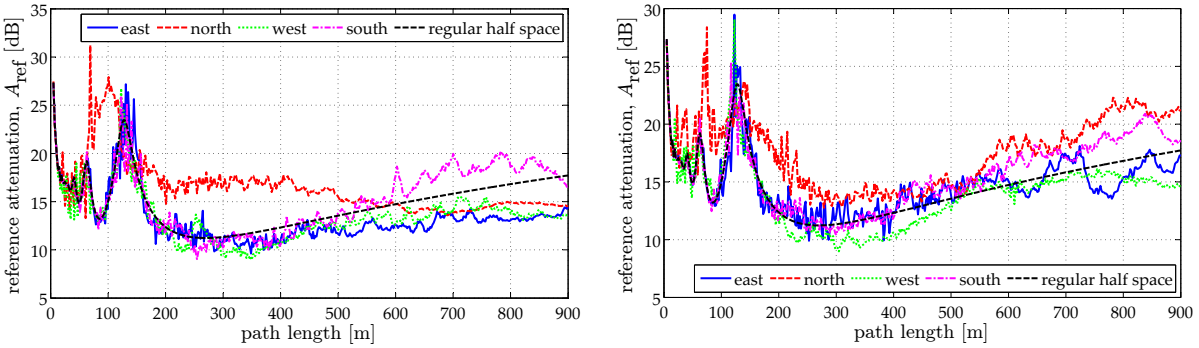

(a) orientation 1 **(b)** orientation 2

Figure D.1: Reference attenuation at 350 MHz for a noise source at a height of 5 m and receiver at 11 m.

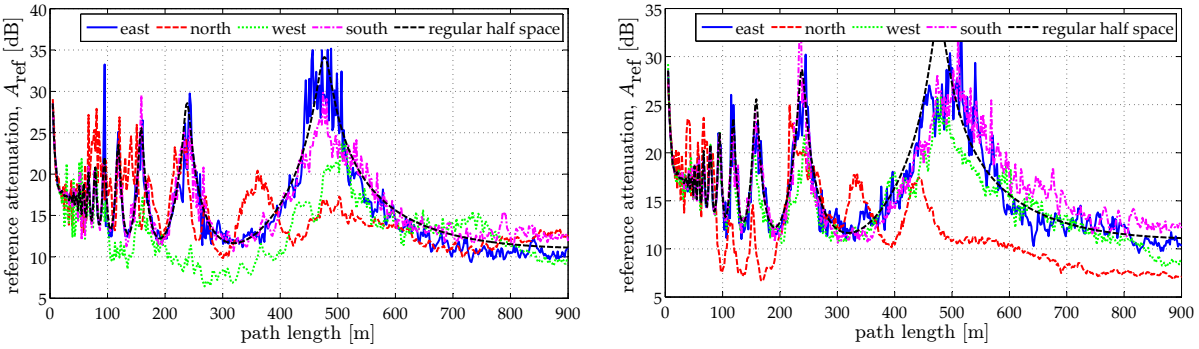

(a) orientation 1 **(b)** orientation 2

Figure D.2: Reference attenuation at 1300 MHz for a noise source at a height of 5 m and receiver at 11 m.

follows the regular half space solution at 350 and 1300 MHz, respectively. Even though A_{ref} does not go lower than 5 dB in either scenario, the potential impact of dish orientation is visible: the most dramatic effects are in the western direction yields in Figure D.2a, while in Figure D.2b A_{ref} is most dramatic in the northern direction.

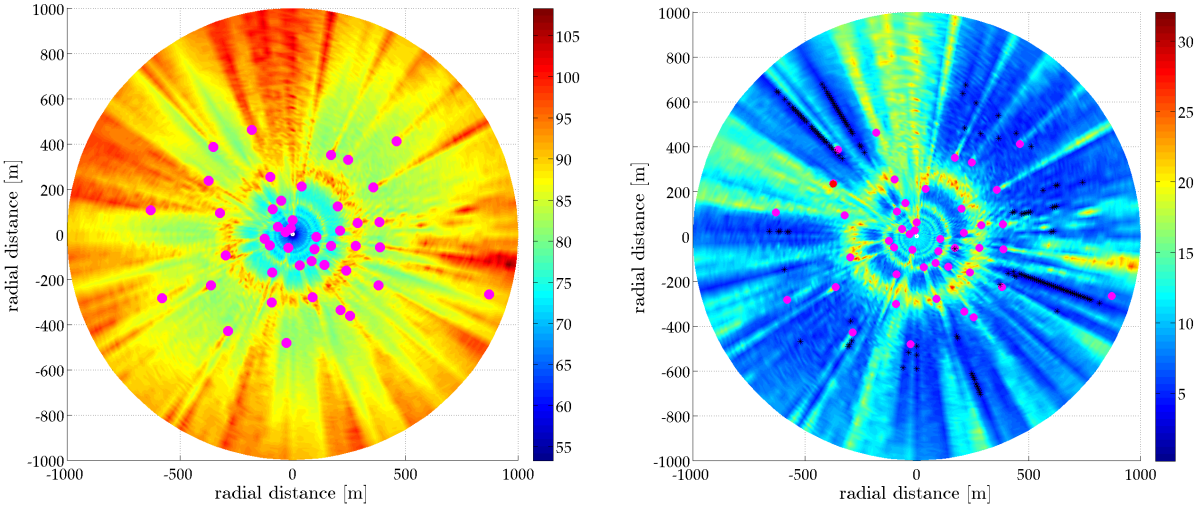

(a) 350 MHz: basic transmission loss

(b) 350 MHz: reference attenuation

Figure D.3: Attenuation map for orientation 2 at 350 MHz

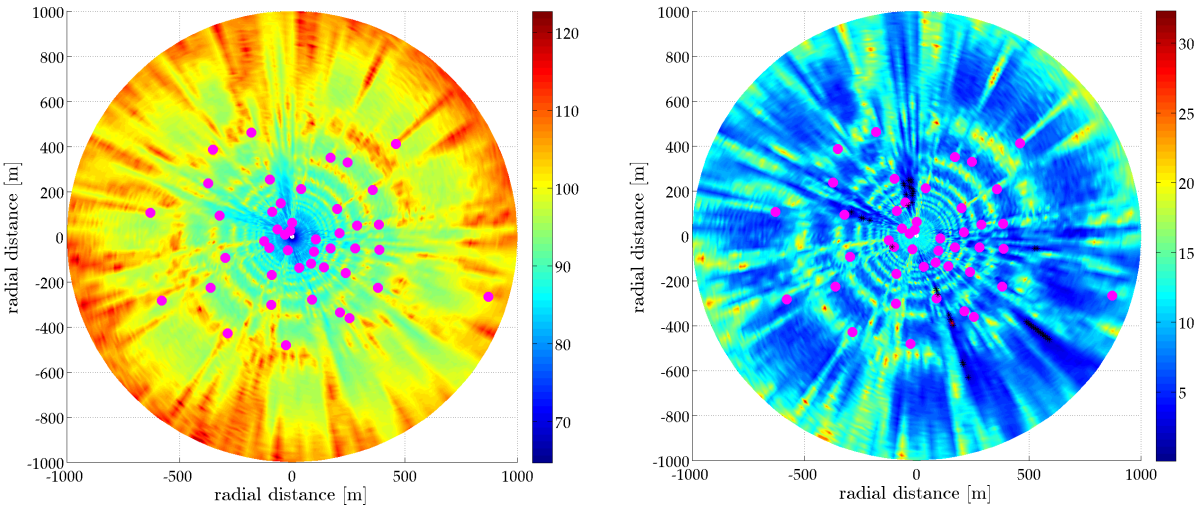

(a) 1300 MHz: basic transmission loss

(b) 1300 MHz: reference attenuation

Figure D.4: Attenuation map for orientation 2 at 1300 MHz

D.2 Attenuation Mapping

Attenuation maps provide an overview of the evolution of basic transmission loss or reference attenuation within a given radius of the horizontal plane. This offers aggregated insights regarding the electromagnetic characteristics of an environment as they relate to signal propagation.

Appendix D.2.1 shows the attenuation maps for orientation 2, supplementing the results in Section 5.3. Additional maps for an omni-directional source at the periphery of the MeerKAT core are presented in Appendix D.2.2.

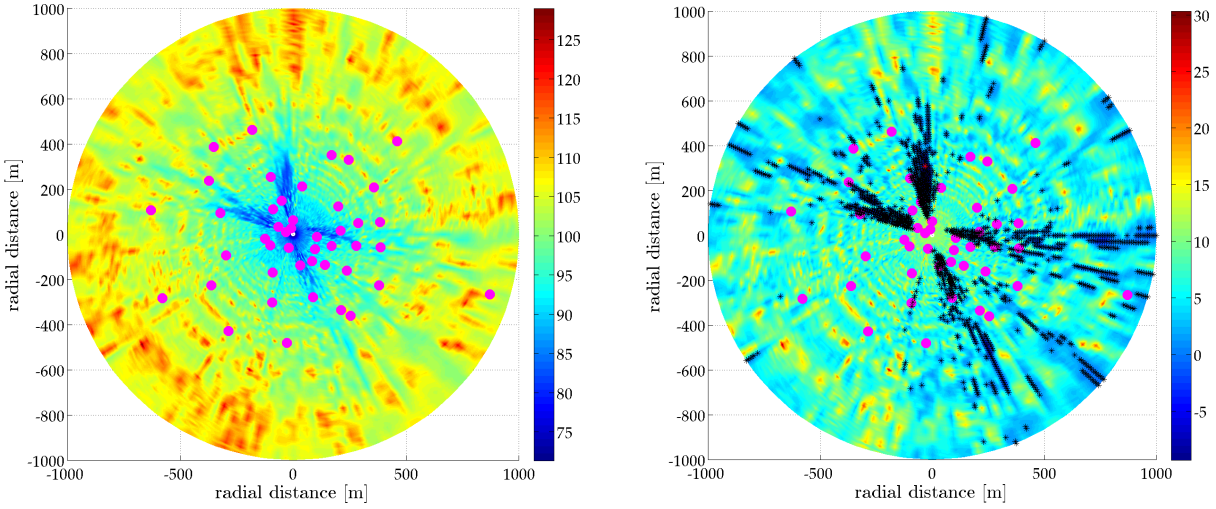

(a) 3050 MHz: basic transmission loss

(b) 3050 MHz: reference attenuation

Figure D.5: Attenuation map for orientation 2 at 3050 MHz

D.2.1 Attenuation Maps for Orientation 2

Orientation 2 relates to the MeerKAT receptors in a northeast direction. In Figures D.3, D.4 and D.5, receptor locations are represented by the magenta dots while the asterisks show the relative high risk locations. These high risk locations correspond to ≤ 4 dB in Figure D.3b, ≤ 2 dB in Figure D.4b and ≤ 1 dB in Figure D.5b. There are clearly more high risk regions at high frequency (3050 MHz).

D.2.2 Attenuation Mapping: Source at the Periphery

Placing the source at the periphery is more representative of what is likely to occur in practice. This relates specifically to RFI sources such as GSM transmissions and windmills. The absolute power values are not required since results are viewed in terms of transmission losses.

As was done in Section 5.3, basic transmission loss (L_b) and reference attenuation (A_{ref}) for a regular half-space are first presented as a control in Figure D.6. For all three frequencies, A_{ref} is at least 6 dB above free space loss (FSL).
It can be seen in Figures D.7 and D.8, corresponding respectively to orientations 1 and 2, that the results are not as severe as when the source is at the centre of the core, as expected. Reinforcement occurs at a few locations leading to values of A_{ref} in the range 0 dB - 2 dB. However, the most pronounced effect for the two configurations investigated is shadowing as seen by the streaks behind the dishes. While there is clear reduction in the amount of loss (as compared to the regular half-space), the characteristic pattern is preserved, albeit interrupted by higher loss streaks.

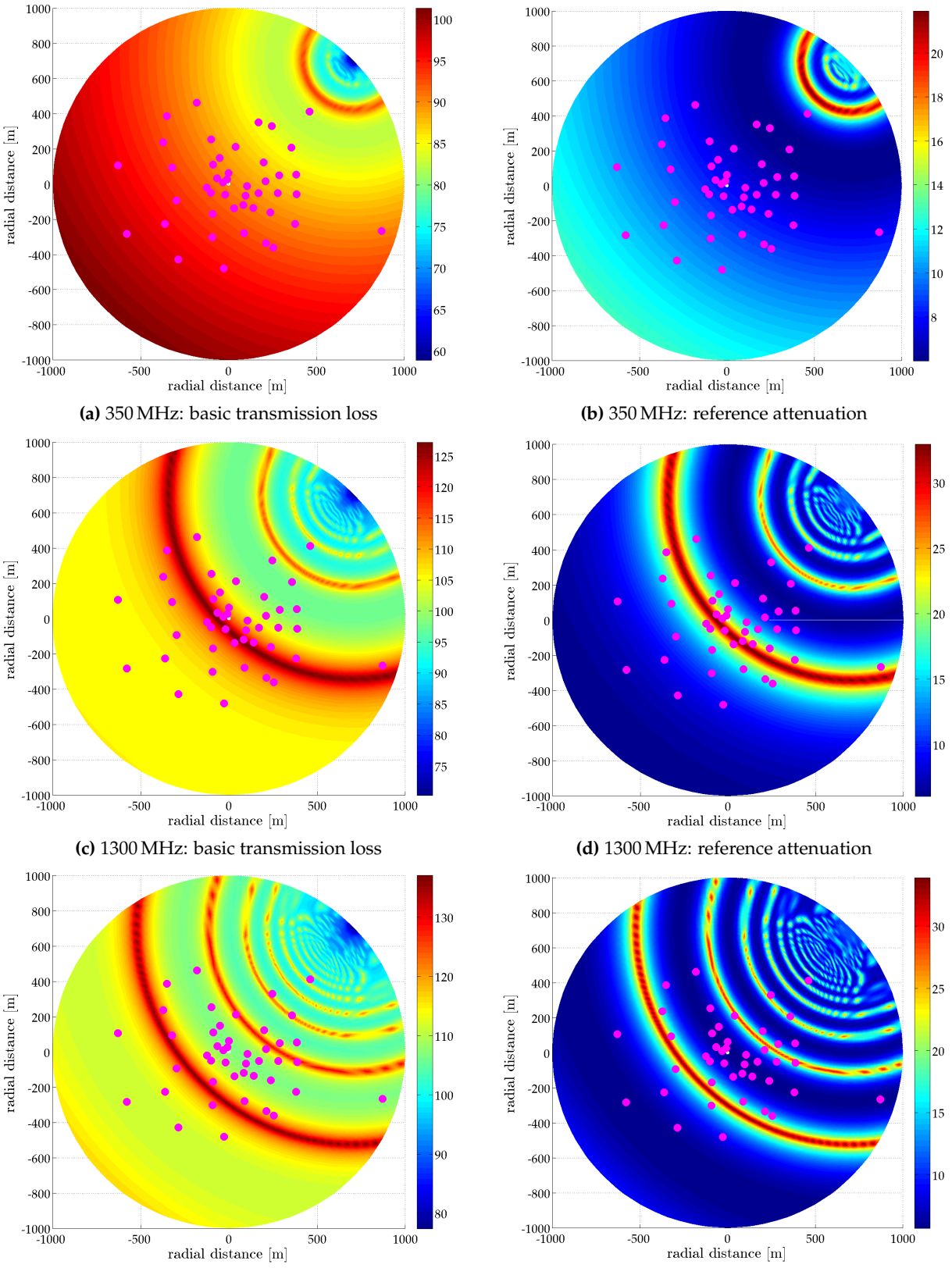

(a) 350 MHz: basic transmission loss

(b) 350 MHz: reference attenuation

(c) 1300 MHz: basic transmission loss

(d) 1300 MHz: reference attenuation

(e) 3050 MHz: basic transmission loss

(f) 3050 MHz: reference attenuation

Figure D.6: Attenuation maps for a regular half-space given a peripheral source. The magenta dots represent the locations of MeerKAT receptors relative to the centre of the array.

Periphery Source: Orientation 1

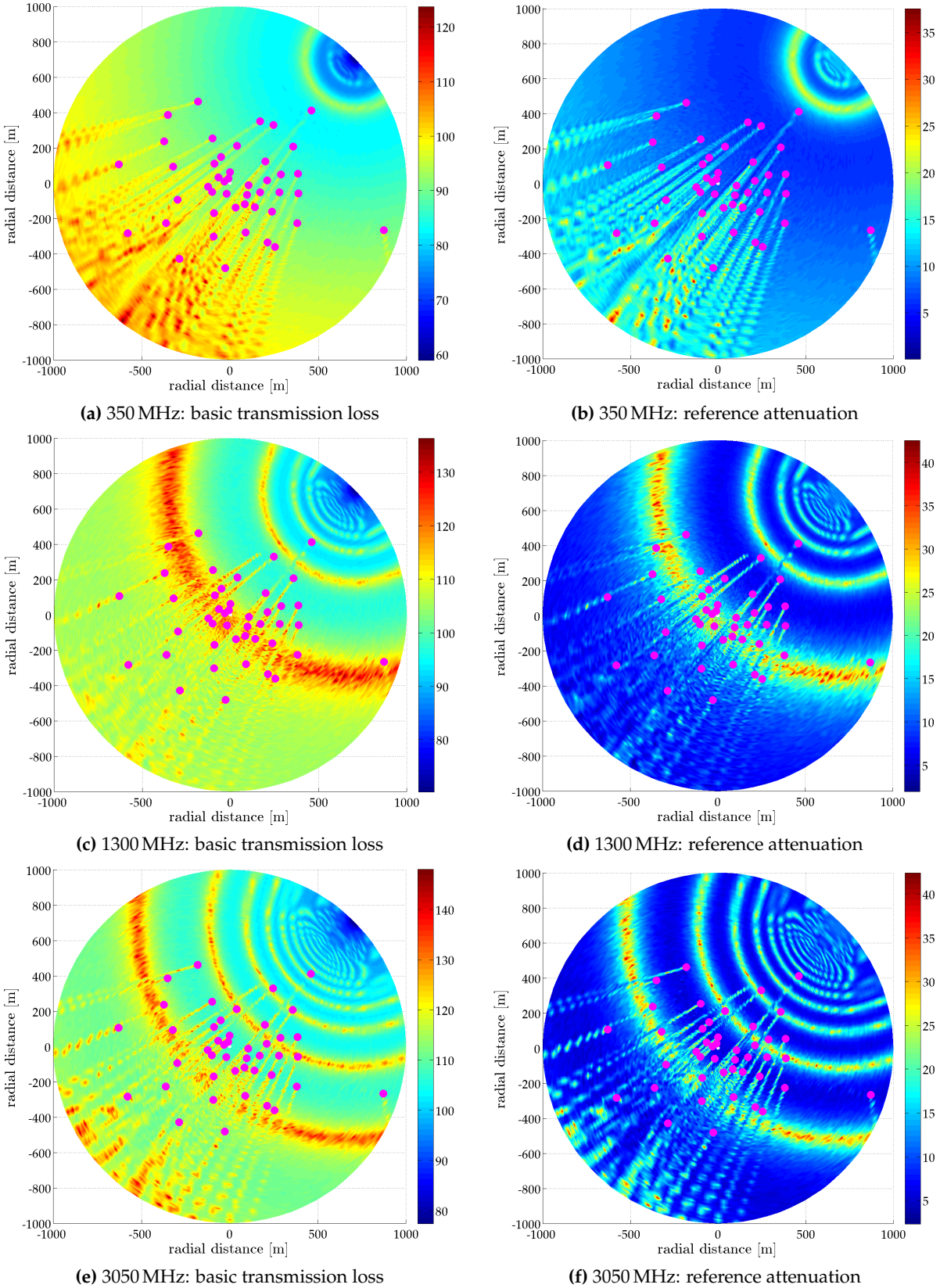

(a) 350 MHz: basic transmission loss

(b) 350 MHz: reference attenuation

(c) 1300 MHz: basic transmission loss

(d) 1300 MHz: reference attenuation

(e) 3050 MHz: basic transmission loss

(f) 3050 MHz: reference attenuation

Figure D.7: Attenuation maps for orientation 1 and a peripheral source.

Periphery Source: Orientation 2

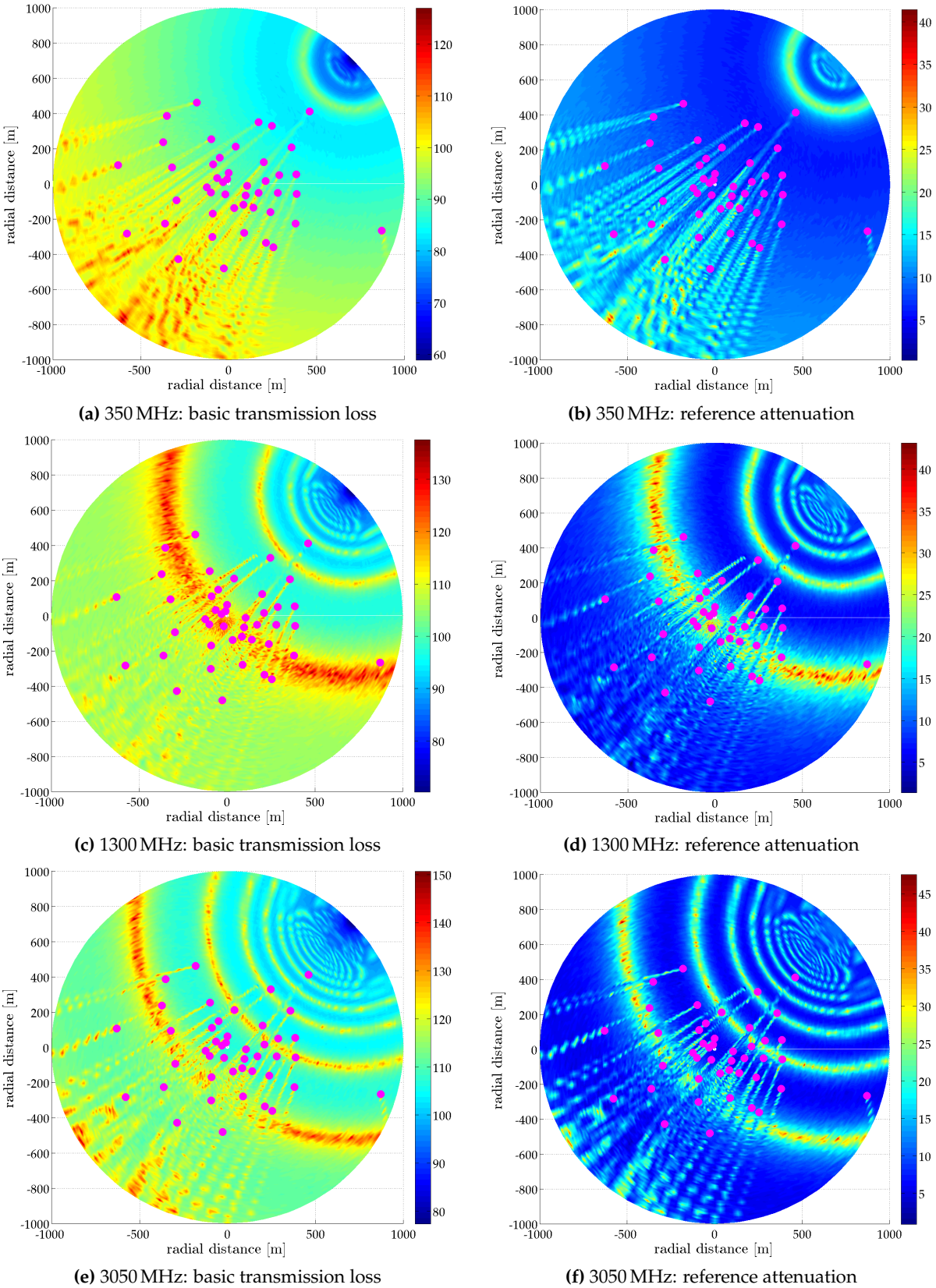

(a) 350 MHz: basic transmission loss

(b) 350 MHz: reference attenuation

(c) 1300 MHz: basic transmission loss

(d) 1300 MHz: reference attenuation

(e) 3050 MHz: basic transmission loss

(f) 3050 MHz: reference attenuation

Figure D.8: Attenuation maps for orientation 2 and a peripheral source.

D.3 Histograms: Path loss Exponent

The numeric data from Sections 5.2.2 and 5.2.3 was used to compute path loss exponents in Section 5.4 so that propagation through the MeerKAT core could be modelled using the log-distance formula. Figures D.9 and D.10 show the respective histogram plots for directional and omni-directional sources for orientation 2.

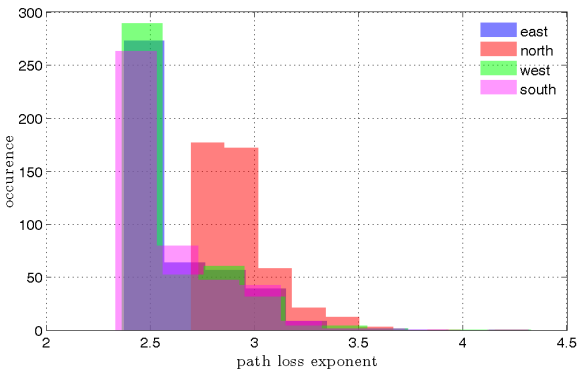

(a) 350 MHz

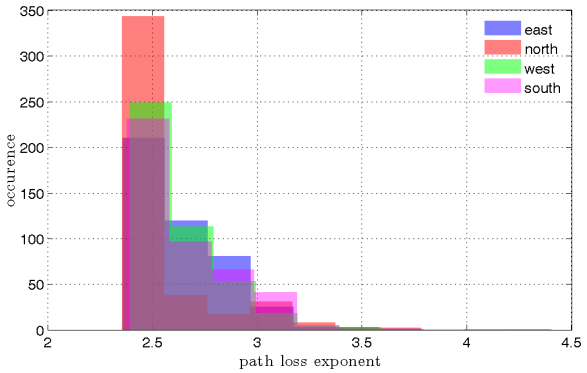

(b) 1300 MHz

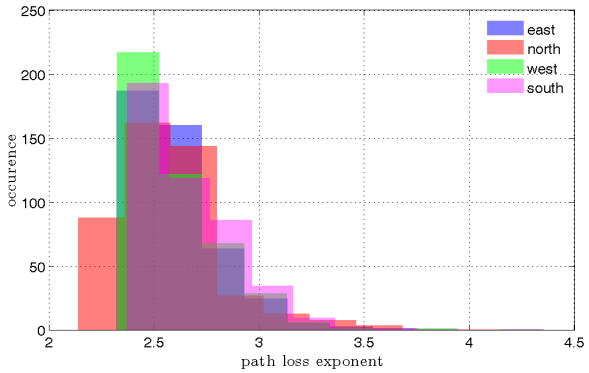

(c) 3050 MHz

Figure D.9: Distribution of path loss exponent in the case of a directional source and MeerKAT receptors in orientation 2.

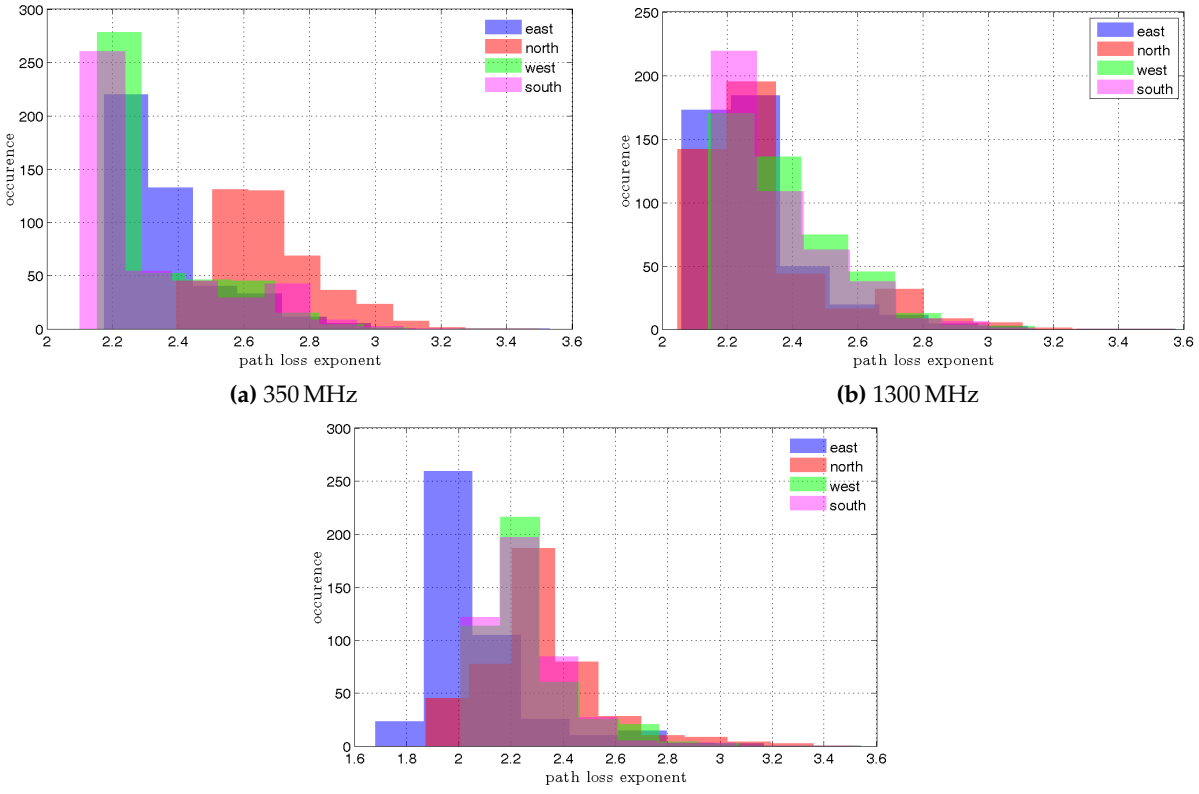

(a) 350 MHz

(b) 1300 MHz

(c) 3050 MHz

Figure D.10: Distribution of path loss exponent in the case of a omni-directional source and MeerKAT receptors in orientation 2.

Bibliography

[1] P.E. Dewdney, "SKA1 System Baseline V2 Description," SKA Organization, Report, 2015. [Online]. Available: https://www.skatelescope.org/wp-content/uploads/2014/03/SKA-TEL-SKO-0000308_SKA1_System_Baseline_v2_DescriptionRev01-part-1-signed.pdf

[2] D.B. Davidson, "The SKA and the MeerKAT Precursor – Extreme Antenna Engineering," in *the 8th European Conference on Antennas and Propagation (EuCAP 2014)*. IEEE, 2014, pp. 1216–1219.

[3] SKA South Africa, "MeerKAT Report: MeerKAT joins the Ranks of the World's Great Scientific Instruments through its First Light Image," Jul 2016. [Online]. Available: http://newsletter.skatelescope.org/category/news-from-the-precursor-and-pathfinder-facilities-skaenews-september2016/meerkat-report-skaenews-september2016/

[4] J.L. Jonas, "MeerKAT – The South African Array With Composite Dishes and Wide-Band Single Pixel Feeds," *Proceedings of the IEEE*, vol. 97, no. 8, pp. 1522–1530, Aug 2009.

[5] Republic of South Africa, "Act No. 21 of 2007: Astronomy Geographic Advantage Act," *Government Gazette*, vol. 516, no. 31157, Jun 2008. [Online]. Available: http://www.dst.gov.za/images/pdfs/Astronomy%20Geographic%20Advantage%20Act.pdf

[6] ——, "Astronomy Geographic Advantage Act No. 21 of 2007: Declaration of the Karoo Central Astronomy Advantage Areas," *National Gazettes*, vol. 584, no. 37397, Feb 2014. [Online]. Available: http://cer.org.za/wp-content/uploads/2014/03/Declaration-of-the-Karoo-Central-Astronomy-Advantage-Area.pdf

[7] H.C. Reader *et al.*, "South African SKA demonstrator systems: Evolving RFI mitigation investigations," in *General Assembly and Scientific Symposium, 2011 XXXth URSI*, Aug 2011, pp. 1–4.

[8] ——, "EMC techniques for a Complex Project: Karoo Array Telescope," in *Aerospace EMC, 2012 Proceedings ESA Workshop on*, May 2012, pp. 1–4.

[9] P.G. Wiid, H.C. Reader, and R.H. Geschke, "Radio Frequency Interference and Lightning Studies of a Square Kilometre Array Demonstrator Structure," *IEEE Transactions on Electromagnetic Compatibility*, vol. 53, no. 2, pp. 543–547, May 2011.

[10] P.S. van der Merwe, A.J. Otto, and H.C. Reader, "Practical Definition of Interface Barrier Effective Shielding," in *International Conference on Electromagnetics in Advanced Applications (ICEAA)*, Sept 2011, pp. 58–61.

[11] H. Pienaar, "Karoo Array Telescope Site Shielding: Laboratory, Computational and Multi-copter Studies," Ph.D. dissertation, Department of E&E Engineering, Stellenbosch University, 2015.

[12] H. Pienaar *et al.*, "Building Electromagnetic Shielding Characterisation using Multicopter," in *Asia-Pacific International Symposium on Electromagnetic Compatibility (APEMC)*, vol. 01, May 2016, pp. 309–312.

[13] A.J. Otto, P.S. van der Merwe, and H.C. Reader, "Real Time Analyser: 'Nuweberg' Berm and Propagation Loss Measurements," MESA Solutions (Pty) Ltd, Internal SKA-SA Report, 2014.

[14] N. Matthysen, "Time Domain Metrology for MeerKAT Systems," Master's thesis, Department of E&E Engineering, Stellenbosch University, 2014.

[15] C. Phillips, D. Sicker, and D. Grunwald, "Bounding the Practical Error of Path Loss Models," *International Journal of Antennas and Propagation*, vol. 2012, 2012.

[16] ITU-R, "Recommendation ITU-R P.1546-5: Method for Point-to-Area Predictions for Terrestrial Services in the Frequency Range 30 MHz to 3000 MHz," International Telecommunication Union, Tech. Rep., 2013.

[17] L. Barclay, "Short-range propagation," in *Propagation of Radiowaves*, 2nd ed., L. Barclay, Ed. London: Institution of Engineering and Technology, 2003, ch. 9. [Online]. Available: http://digital-library.theiet.org/content/books/ew/pbew502e

[18] ITU-R, "Recommendation ITU-R P.1411-8: Propagation Data and Prediction Methods for the Planning of Short-range Outdoor Radiocommunication Systems and Radio Local Area Networks in the Frequency Range 300 MHz to 100 GHz," International Telecommunication Union, Tech. Rep., 2015.

[19] T. Kürner, "Propagation Models for Macro-Cells," in *COST Action 231: Digital Mobile Radio Towards Future Generation Systems (Final Report)*, E. Damosso, Ed. European Commission, 1999, ch. 4.4. [Online]. Available: http://grow.tecnico.ulisboa.pt/~grow.daemon/cost231/

[20] C.A. Balanis, *Advanced Engineering Electromagnetics*, 2nd ed. New York: John Wiley & Sons, Inc., 2012.

[21] S. Ramo, J.R. Whinnery, and T. Van Duzer, *Fields and Waves in Communication Electronics*, 3rd ed. New York: John Wiley & Sons, Inc, 1994.

[22] R.E. Collin, *Foundations for Microwave Engineering*, 2nd ed. New York: IEEE Press, 2001.

[23] J.S. Seybold, *Introduction to RF Propagation*. New Jersey: John Wiley & Sons, Inc., 2005.

[24] M. Mehler, "Electromagnetic Wave Propagation," in *Propagation of Radiowaves*, 2nd ed., L. Barclay, Ed. London: Institution of Engineering and Technology, 2003, ch. 5. [Online]. Available: http://digital-library.theiet.org/content/books/ew/pbew502e

[25] L. Barclay, "Basic Principles 1," in *Propagation of Radiowaves*, 2nd ed., L. Barclay, Ed. London: Institution of Engineering and Technology, 2003, ch. 2. [Online]. Available: http://digital-library.theiet.org/content/books/ew/pbew502e

[26] C. Haslett, *Essentials of Radio Wave Propagation*. New York: Cambridge University Press, 2008.

[27] C.A. Balanis, *Antenna Theory: Analysis and Design, 3rd Edition*, 3rd ed. Wiley-Interscience, 2005.

[28] A.V. Räisänen and A. Lehto, *Radio Engineering for Wireless Communication and Sensor Applications*. Massachusetts: Artech House Inc., 2003.

[29] P.L. Rice *et al.*, "Transmission Loss Predictions for Tropospheric Communication Circuits," National Bureau of Standards, Washington D.C, Tech. Rep., 1965.

[30] International Telecommunication Union, "Recommendation ITU-R P.341-5: The Concept of Transmission Loss for Radio Links," International Telecommunication Union, Tech. Rep., Oct 1999.

[31] W. Gosling, *Radio Antennas and Propagation*. Massachusetts: Newnes, 1998.

[32] D. Bacon, "Introduction to Diffraction," in *Propagation of Radiowaves*, 2nd ed., L. Barclay, Ed. London: Institution of Engineering and Technology, 2003, ch. 8. [Online]. Available: http://digital-library.theiet.org/content/books/ew/pbew502e

[33] International Telecommunication Union, "Recommendation ITU-R P.526-12: Propagation by Diffraction," International Telecommunication Union, Tech. Rep., Feb 2012.

[34] D. Bacon, "Reflection and Scattering from Rough Surfaces," in *Propagation of Radiowaves*, 2nd ed., L. Barclay, Ed. London: Institution of Engineering and Technology, 2003, ch. 6. [Online]. Available: http://digital-library.theiet.org/content/books/ew/pbew502e

[35] E.C. Jordan and K.G. Balmain, *Electromagnetic Waves and Radiating Systems*, 2nd ed. New Jersey: Prentice-Hall Inc., 1968.

[36] J.D. Parsons, *The Mobile Radio Propagation Channel*, 2nd ed. Chichester: John Wiley & Sons Ltd, 2000.

[37] D. Bacon, "Basic Principles 2," in *Propagation of Radiowaves*, 2nd ed., L. Barclay, Ed. London: Institution of Engineering and Technology, 2003, ch. 3. [Online]. Available: http://digital-library.theiet.org/content/books/ew/pbew502e

[38] T.S. Rappaport, *Wireless Communications: Principles and Practice*, 2nd ed. New Jersey: Prentice Hall, 2001.

[39] ITU-R, "Rec. ITU-R P.527-3: Electrical Characteristics of the Surface of the Earth," International Telecommunication Union, Tech. Rep., 1992.

[40] K.A. Norton, "The Propagation of Radio Waves Over the Surface of the Earth and in the Upper Atmosphere - Part II," in *Proceedings of the Institute of Radio Engineers*, vol. 25, no. 9, 1937.

[41] D.J. Angelakos and T.E. Everhart, *Microwave Communications*, ser. Electrical Engineering Series. New York: McGraw-Hill Inc., 1968.

[42] P.L. Overfelt, "Review of Electromagnetic Surface Waves: 1960 Through 1987," DTIC Document, Naval Weapons Center, China Lake CA, Tech. Rep., 1988.

[43] R.E. Collin, *Antennas and Radiowave Propagation*. New York: John Wiley & Sons, Inc, 1985.

[44] F.E. Terman, *Radio Engineers' Handbook*. New York: McGraw Hill Book Company, Inc, 1943.

[45] J. Milsom, "Surface Waves, and Sky Waves below 2 MHz," in *Propagation of Radiowaves*, 2nd ed., L. Barclay, Ed. London: Institution of Engineering and Technology, 2003, ch. 18. [Online]. Available: http://digital-library.theiet.org/content/books/ew/pbew502e

[46] C. Phillips, D. Sicker, and D. Grunwald, "A Survey of Wireless Path Loss Prediction and Coverage Mapping Methods," *IEEE Communications Surveys & Tutorials*, vol. 15, no. 1, 2013.

[47] T.K. Sarkar *et al.*, "A Survey of Various Propagation Models for Mobile Communication," *IEEE Antennas and Propagation Magazine*, vol. 45, no. 3, 2003.

[48] V.S. Abhayawardhana *et al.*, "Comparison of Empirical Propagation Path Loss Models for Fixed Wireless Access Systems," in *Proceedings of the* 61^{st} *IEEE Vehicular Technology Conference*, 2005.

[49] H. Harada and R. Prasad, *Simulation and Software Radio for Mobile Communications*. Massachusetts: Artech House, Inc., 2002.

[50] J.J. Egli, "Radio Propagation above 40 MC over Irregular Terrain," *Proceedings of the IRE*, vol. 45, no. 10, pp. 1383–1391, Oct 1957.

[51] S.R. Saunders, "Outdoor Mobile propagation," in *Propagation of Radiowaves*, 2nd ed., L. Barclay, Ed. London: Institution of Engineering and Technology, 2003, ch. 11. [Online]. Available: http://digital-library.theiet.org/content/books/ew/pbew502e

[52] G.A. Hufford, A.G. Longley, and W.A. Kissick, "A Guide to the Use of the ITS Irregular Terrain Model in the Area Prediction Mode," National Technical Information Service, Tech. Rep., Apr 1982.

[53] A.G. Longley and P.L. Rice, "Prediction of Tropospheric Radio Transmission Loss Over Irregular Terrain: A Computer Method - 1968," Institute for Telecommunication Sciences (ITS), National Technical Information Service, Tech. Rep., Jun 1968.

[54] G.A. Hufford, "The ITS Irregular Terrain Model, Version 1.2.2: The Algorithm," National Technical Information Service, Tech. Rep., Sep 1984.

[55] C. Phillips, D. Sicker, and D. Grunwald, "The Stability of The Longley-Rice Irregular Terrain Model for Typical Problems," Department of Computer Science, University of Colorado, Tech. Rep., 2011.

[56] B. Henderson, "Radio Mobile Program Operating Guide," 2013. [Online]. Available: http://www3.telus.net/hendersb/documents/Radio%20Mobile.pdf

[57] Softwright LLC. (2000) Notes on Longley-Rice Propagation. [Online]. Available: http://www.softwright.com/faq/engineering/prop_longley_rice.html

[58] E. Östlin, "On Radio Wave Propagation Measurements and Modelling for Cellular Mobile Radio Networks," Doctoral Thesis, Blekinge Institute of Technology, 2009.

[59] Y.S. Meng, Y.H. Lee, and B. Ng, "Study of Propagation Loss Prediction in Forest Environment," *Progress In Electromagnetics Research B*, vol. 17, pp. 117–133, 2009.

[60] International Telecommunication Union, "Recommendation ITU-R P.833-8: Attenuation in Vegetation," International Telecommunication Union, Tech. Rep., 09 2013.

[61] H.K. Sharma, S. Sahu, and S. Sharma, "Enhanced Cost231 W.I. Propagation Model in Wireless Network," *International Journal of Computer Applications*, vol. 19, no. 6, 2011.

[62] J. Walfisch and H.L. Bertoni, "A theoretical model of UHF Propagation in Urban Environments," *IEEE Transactions on Antennas and Propagation*, vol. 36, no. 12, pp. 1788–1796, Dec 1988.

[63] F. Ikegami, T. Takeuchi, and S. Yoshida, "Theoretical prediction of mean field strength for urban mobile radio," *IEEE Transactions on Antennas and Propagation*, vol. 39, no. 3, pp. 299–302, Mar 1991.

[64] M.F. Iskander and Z. Yun, "Propagation Prediction Models for Wireless Communication Systems," *IEEE Transactions on Microwave Theory and Techniques*, vol. 50, no. 3, 2002.

[65] E. Damosso and L. Correia, Eds., *COST Action 231: Digital Mobile Radio Towards Future Generation Systems (Final Report)*, ser. EUR (Series). European Commission, 1999. [Online]. Available: http://grow.tecnico.ulisboa.pt/~grow.daemon/cost231/

[66] R. Vaughan and J.B. Andersen, *Channels, Propagation and Antennas for Mobile Communications*, ser. Electromagnetics and Radar Series. Institution of Engineering and Technology, 2006. [Online]. Available: http://digital-library.theiet.org.ez.sun.ac.za/content/books/ew/pbew050e

[67] Z. Chen, A. Delis, and H.L. Bertoni, "Radio-wave Propagation Prediction using Ray-Tracing Techniques on a Network of workstations (NOW)," *Journal of Parallel and Distributed Computing*, vol. 64, no. 10, pp. 1127–1156, 2004. [Online]. Available: http://dblp.uni-trier.de/db/journals/jpdc/jpdc64.html#ChenDB04

[68] C.C. Constantinou, "Numerically Intensive Propagation Prediction Methods," in *Propagation of Radiowaves*, 2nd ed., L. Barclay, Ed. London: Institution of Engineering and Technology, 2003, ch. 10. [Online]. Available: http://digital-library.theiet.org/content/books/ew/pbew502e

[69] J-M. Jin, *Theory and Computation of Electromagnetic Fields*. New Jersey: John Wiley & Sons, Inc, 2010.

[70] D.B. Davidson, *Computational Electromagnetics for RF and Microwave Engineering*, 2nd ed. Cambridge: Cambridge University Press, 2011.

[71] E. Kreyszig, *Advanced Engineering Mathematics*, 9th ed. New Jersey: John Wiley & Sons, Inc, 2006.

[72] K.H. Craig and M.F. Levy, "Parabolic Equation Modelling of the Effects of Multipath and Ducting on Radar Systems," *IEE Proceedings F - Radar and Signal Processing*, vol. 138, no. 2, pp. 153–162, April 1991.

[73] C. Brennan and D. Trinh, "Fullwave computation of path loss in urban areas," in *the 8th European Conference on Antennas and Propagation (EuCAP)*, April 2014, pp. 1124–1127.

[74] C. Beaudet, J. Ford *et al.*, "Radio Frequency Interference Management Efforts at the National Radio Astronomy Observatory Green Bank Site," in *Radio Science Meeting (USNC-URSI NRSM)*, 2013.

[75] A.J. Boonstra, M. Van Veelen, and R. Millenaar, "EMC and RFI Environment Aspects for Wide Area Sensor Networks," in *the XXVIIth URSI GA*, 2002.

[76] A. Jessner *et al.*, "EMI Protection and Threshold Levels for the SKA," 2014, Status: Submitted (2014-04-07).

[77] T.J. Phiri, D.B. Davidson, and P.G. Wiid, "Propagation Modelling for the South African SKA Site," in *IEEE-APS Topical Conference on Antennas and Propagation in Wireless Communications (APWC)*. IEEE, 2015, pp. 1329–1332.

[78] International Telecommunication Union, "Recommendation ITU-R P.530-15: Propagation Data and Prediction Methods Required for the Design of Terrestrial Line-of-Sight Systems," International Telecommunication Union, Tech. Rep., 09 2013.

[79] W.C.Y. Lee, *Wireless and Cellular Communications*, 3rd ed. New York: McGraw-Hill, 2012.

[80] K. Craig, "Computer modelling," in *Propagation of Radiowaves*, 3rd ed., L. Barclay, Ed. London: Institution of Engineering and Technology, 2012, ch. 20. [Online]. Available: http://digital-library.theiet.org/content/books/ew/pbew056e

[81] E. Östlin, H. Suzuki, and H.-J. Zepernick, "Evaluation of the Propagation Model Recommendation ITU-R P.1546 for Mobile Services in Rural Australia," *IEEE Transactions on Vehicular Technology*, vol. 57, no. 1, pp. 38–51, January 2008.

[82] K. Low, "Comparison of Urban Propagation Models with CW-measurements," in *42nd IEEE Vehicular Technology Conference*. IEEE, 1992, pp. 936–942.

[83] N. Faruk, A. Ayeni, and Y.A. Adediran, "On the Study of Empirical Path Loss Models for Accurate Prediction of TV Signal for Secondary Users," *Progress In Electromagnetics Research B*, vol. 49, pp. 155–176, 2013.

[84] A.J. Otto, P.S. van der Merwe, and A.R. Botha, "GSM Propagation Analysis," MESA Solutions (Pty) Ltd, Internal SKA-SA Report, 2015.

[85] A.R. Botha, "Development of a Real-Time Transient Analyser for the SKA," Master's thesis, Department of E&E Engineering, Stellenbosch University, 2014.

[86] S.N. Lophaven, H.B. Nielsen, and J. Søndergaard, "A MATLAB Kriging Toolbox," Technical University of Denmark (DTU), Technical Report, 2002.

[87] K.A. Kent and R.J. Luebbers, "An Evaluation of Longley-Rice and GTD Propagation Models," *IEEE Transactions on Antennas and Propagation*, vol. AP-30, no. 6, pp. 1093–1098, November 1982.

[88] S. Kasampalis *et al.*, "Comparison of Longley-Rice, ITM and ITWOM propagation models for DTV and FM Broadcasting," in *16th International Symposium on Wireless Personal Multimedia Communications (WPMC)*, June 2013, pp. 1–6.

[89] ——, "Comparison of Longley-Rice, ITU-R P.1546 and Hata-Davidson Propagation models for DVB-T Coverage Prediction," in *IEEE International Symposium on Broadband Multimedia Systems and Broadcasting*, June 2014, pp. 1–4.

[90] A.R. Botha *et al.*, "Dynamic RFI Measurement Systems on a ROACH-2 Platform," in *International Conference on Electromagnetics in Advanced Applications (ICEAA)*, Sept 2013, pp. 502–505.

[91] Altair Hyperworks, "FEKO 14 User Manual," Altair Engineering Inc., 2015.

[92] U. Jakobus *et al.*, "Latest Extensions of the Electromagnetic Field Solver Package FEKO," in *the 10th European Conference on Antennas and Propagation (EuCAP)*. European Association of Antennas and Propagation, 2016.

[93] Altair Hyperworks, "Numerical Methods: Method of Moments," Altair Engineering Inc., 2016. [Online]. Available: https://www.feko.info/product-detail/numerical_methods/mom

[94] G.L. James, *Geometrical Theory of Diffraction for Electromagnetic Waves*, 3rd ed., ser. Electromagnetic Waves. London: Institution of Engineering and Technology, 2007.

[95] Altair Hyperworks, "Numerical Methods: Physical Optics," Altair Engineering Inc., 2016. [Online]. Available: https://www.feko.info/product-detail/numerical_methods/po

[96] V.A. Borovikov and B.Ye. Kinber, *Geometrical Theory of Diffraction*, 3rd ed., ser. Electromagnetic Waves. London: Institution of Electrical Engineers, 1994. [Online]. Available: http://digital-library.theiet.org/content/books/ew/pbew037e

[97] Altair Hyperworks, "Numerical Methods: Geometrical Optics based on Ray Launching," Altair Engineering Inc., 2016. [Online]. Available: https://www.feko.info/product-detail/numerical_methods/rl-go

[98] P.H. Pathak, G. Carluccio, and M. Albani, "The Uniform Geometrical Theory of Diffraction and Some of Its Applications," *IEEE Antennas and Propagation Magazine*, vol. 55, no. 4, pp. 41–69, Aug 2013.

[99] P. Pagani *et al.*, "Geometric Optics and Uniform Theory of Diffraction," in *Ultra-Wideband Radio Propagation Channels*. London: ISTE, 2010, pp. 189–208. [Online]. Available: http://dx.doi.org/10.1002/9780470611715.app3

[100] Altair Hyperworks, "Numerical Methods: Uniform Theory of Diffraction," Altair Engineering Inc., 2016. [Online]. Available: https://www.feko.info/product-detail/numerical_methods/utd

[101] U. Jakobus, "Review of Advanced Electromagnetic Modeling Techniques in the Computer Code FEKO based on the Method of Moments with Hybrid Extensions," *Applied Computational Electromagnetics Society Newsletter*, vol. 18, no. 2, pp. 30–42, 2003.

[102] N. Mutonkole, "Study of a Wideband Sinuous Feed for Reflector Antenna Applications," Master's thesis, Department of E&E Engineering, Stellenbosch University, 2013.

[103] V. van Tonder, "Beamforming for Radio Astronomy," Master's thesis, Department of E&E Engineering, Stellenbosch University, 2014.

[104] J.A. Andriambeloson and P.G. Wiid, "A 3D-Printed PLA Plastic Conical Antenna with Conductive-Paint Coating for RFI Measurements on MeerKAT Site," in *IEEE-APS Topical Conference on Antennas and Propagation in Wireless Communications (APWC)*. IEEE, 2015, pp. 945–948.

[105] P.G. Wiid, "The Answer is in Fact 41, or How to Get 35:1 Bandwidth from a Cone Antenna," in *IEEE-APS Topical Conference on Antennas and Propagation in Wireless Communications (APWC)*. IEEE, 2015, pp. 1060–1063.

[106] S.O. Kuja, "Characterization of RF Signal Coupling into MeerKAT Telescopes," Master's thesis, Department of E&E Engineering, Stellenbosch University, 2015.

[107] K.A. Norton, "The Propagation of Radio Waves Over the Surface of the Earth and in the Upper Atmosphere - Part I," in *Proceedings of the Institute of Radio Engineers*, vol. 24, no. 10, 1936.

[108] SKA South Africa. (2016, Oct) MeerKAT Radio Telescope. [Online]. Available: http://www.ska.ac.za/science-engineering/meerkat/

[109] P.G. Wiid, H.C. Reader, and R.H. Geschke, "Karoo Array Telescope: Lightning Protection Issues and RFI," in *XXXIth URSI General Assembly and Scientific Symposium (URSI GASS)*, Aug 2011, pp. 1–4.

[110] SKA South Africa. (2016, Jul) Public Science/Engineering Site: KAT-7. [Online]. Available: http://public.ska.ac.za/kat-7

[111] H. Friis, "A Note on a Simple Transmission Formula," in *Proceedings of the I.R.E. and Waves and Electrons*. IRE, 1946, pp. 254–256.

[112] ISO/IEC 61000-4-21, " Electromagnetic Compatibility (EMC) Part 4-21: Testing and Measurement Techniques - Reverberation Chamber Test Methods," International Electrotechnical Commission (IEC), Technical Report, 2009.

[113] K.H. Craig, "Clear-air Characteristics of the Troposphere," in *Propagation of Radiowaves*, 2nd ed., L. Barclay, Ed. London: Institution of Engineering and Technology, 2003, ch. 7. [Online]. Available: http://digital-library.theiet.org/content/books/ew/pbew502e

[114] A.J. Otto, H.C. Reader, and R.G. Marchand, "Complex Permittivity Measurements of Karoo Soil for the Square Kilometre Array," in *International Conference on Electromagnetics in Advanced Applications (ICEAA)*, 2011.

[115] J. Taylor, *Introduction to Error Analysis, the Study of Uncertainties in Physical Measurements*, 2nd ed. New York: University Science Books, 1997.

[116] P.G. Wiid and H.C. Reader, "Towards Electromagnetic Characterization of MeerKAT Telescope," in *General Assembly and Scientific Symposium (URSI GASS), 2014 XXXIth URSI*, Aug 2014, pp. 1–4.

[117] S.O. Kuja and P.G. Wiid, "Characterization of RF Signal Coupling between MeerKAT Telescope Structures," in *IEEE-APS Topical Conference on Antennas and Propagation in Wireless Communications (APWC)*, Sept 2015, pp. 1004–1007.

[118] SKA South Africa. (2016, Jun) MeerKAT Array Releases and Specifications. [Online]. Available: http://public.ska.ac.za/meerkat/meerkat-schedule